An Investigation into Radiative Property Variations across Pre-Annealed Advanced High Strength Steel Coils

by

Nishant Sriram Narayanan

A thesis

presented to the University of Waterloo

in fulfilment of the

thesis requirement for the degree of

Master of Applied Science

in

Mechanical and Mechatronics Engineering

Waterloo, Ontario, Canada, 2023

Author's Declaration

Abstract

In recent years, increasingly stringent crashworthiness and emissions regulations have driven automakers to consider novel materials for automotive lightweighting. Advanced high-strength steels (AHSS) used in automotive chassis construction has increased considerably. The most widely used grades of AHSS are dual-phase (DP) ferrite-martensite ($\alpha + \alpha'$) grades.

Advanced high strength steel coils must be annealed with a precise heating schedule to achieve the required mechanical properties. However, temperature excursions during intercritical annealing cause erratic changes in the steel's microstructure, resulting in variations in post-annealed mechanical properties across coils. These variations lead to high scrap rates and cost manufacturers millions of dollars annually. Past research has attributed these temperature excursions to non-uniform thermal irradiation. The present work shows variations in radiative properties across a single AHSS coil may cause temperature excursions through pyrometer errors and nonuniform heating. Radiative property variations across a coil may also arise before annealing due to non-homogeneities in surface topography, influencing how the radiative properties subsequently evolve during annealing.

This thesis documents experimental and theoretical work characterising radiative property variations across a single AHSS coil processed on an industrial cold-rolling line. The *ex-situ* radiative properties of samples extracted from various coil locations are analysed using a Fourier Transform Infra-Red (FTIR) spectrometer equipped with an integrating sphere, revealing large swings in radiative properties along its length and width. The effect of these variations on pyrometric temperature measurements, strip temperature evolution, and in turn, the as-formed mechanical properties are discussed.

Radiative property variations are strongly correlated to differences in surface topography (particularly surface cavities) through optical profilometry, optical microscopy, and scanning electron microscopy (SEM). The work uses 3D depth mapping of optical imagery to generate surface height maps and theoretically models the radiative properties using a geometric optics approximation (GOA) ray-tracing algorithm. The GOA approach provides accurate spectral emissivity predictions within its validity regime.

The study then explores reasons for surface cavity formation, hypothesising that cavities form due to the dissolution of selective grain boundary oxides (formed during hot rolling) during acid pickling, which leads to micro-topographical changes to the strip surface. Furthermore, non-homogeneous cold-rolling parameters subsequently lead to non-uniform cavity flattening. The thesis then explores the combined effect of acid pickling time and cold-rolling reduction percentage by studying different AHSS alloys, cold-rolled and acid-pickled to different extents, through a factorial design-of-experiments procedure.

An artificial neural network (ANN) regression model for near-instantaneous spectral emissivity predictions of AHSS was developed using surface roughness parameters and optical imagery as inputs. Manufacturers can implement this model with emerging *in-situ* strip imaging technologies to provide real-time spectral emissivity predictions before a coil section enters an annealing furnace. Galvanisers can also use these on-line spectral emissivity predictions to update pyrometry and furnace temperature control algorithms in real time.

This thesis expands our knowledge base on the possible causes for temperature excursions across an AHSS coil during annealing. Findings of this research will benefit steel manufacturers in identifying and reducing non-homogeneities in mechanical properties across AHSS coils, reducing high scrap rates in the industry.

Acknowledgements

First and foremost, I would like to thank my supervisor and professor, Dr. Kyle Daun, for assigning me this exciting project (ZCO-72), which has such a strong industrial impact. This thesis would have been impossible without your continued help and support; you really are an excellent teacher and mentor.

Secondly, a special thanks to Kaihsiang Lin and Fatima Suleiman for all our interesting discussions regarding the project and all the help they afforded me during my first few weeks and months in the lab.

A special thanks to Dr. Wanda Melfo Prada and Dr. Marga Zuijderwijk of Tata Steel, Mr. William Marr, Mr. Chad Cathcart, and Mr. Francis Barrado of Stelco for providing an industrial perspective.

I would also like to thank all my wonderful colleagues at WatLIT, past and present, Arpan Singh (it was great talking about *Subaru WRXs* and *Honda Civics* with you), Alireza Kaveh, Cameron Klassen, Boxuan (Tom) Zhao, Stanislav Musikhin, Stephen Robinson-Enebeli, Paule Laperye, Rodrigo Brenner Miguel, Daniel Christopher Blackmore, Ned Zhou, Sina-Talebi Moghaddam, Michael Christopher Nagorski, and Ardhendu Shekhar Bhattacharya. The brilliant minds with whom I have had the privilege to work and share a lab.

I would also like to thank Dr. Yuquan Ding for his assistance with the optical profilometer, Professor Duane Cronin and Mr. Devon Hartlen for their assistance with the Keyence digital microscope, and Dr. Nina Heinig and Dr. Lei Zhang for their help with the Scanning Electron Microscope (SEM).

Thank you to all the individuals and organisations who/that are part of the Galvanized Autobody Partnership (GAP); this project would not have been possible without them.

Lastly, I would also like to thank my parents (Sriram Narayanan & Rinku Sriram Narayanan), grandparents, family, and friends (everyone I have known from my days in India, Singapore, the US, and Canada) for all their love and support. This work would have been impossible without all of you!

Table of Contents

Author's Declaration ii

Abstract iii

Acknowledgements v

List of Figures ix

List of Tables xvi

List of Abbreviations xvii

Nomenclature xix

Quote xxiii

Chapter 1 : Overview and Industrial Motivation 1

1.1: Introduction to Advanced High-Strength Steels 1

1.2: AHSS Manufacturing Process 3

1.2.1 Manufacturing Chain 3

1.2.2 Annealing Process and Microstructure 4

1.2.3 Continuous Galvanising Lines 6

1.3 Research Motivation & Objectives 7

1.4 Overview of Thesis 9

1.5 Research Contributors 10

Chapter 2 : Theoretical Background 12

2.1 Introduction to Pyrometry 12

2.1.1 Single-Wavelength Pyrometry 14

2.1.2 Dual–Wavelength Pyrometry 15

2.1.3 Multi-Wavelength Pyrometry 16

2.1.4 Pyrometric Wavelength Selection 17

2.2 Annealing Furnace Basics 18

2.2.1 Annealing Furnace Design 18

2.2.2 Furnace Heat Transfer Model 19

Chapter 3 : Radiative Property Characterisation 22

3.1: Sample Extraction and Analysis Performed 22

3.2 Ex-Situ Spectral Reflectivity Analysis 23

3.3 Radiative Property Results for Samples from Different Coil Locations 26

3.3.1 Spectral Emissivity Variations 26

3.3.2 Emissivity Ratio Variations and Pyrometric Temperature Errors 29

3.3.3 Total Hemispherical Absorptivity Variations & Strip Temperature Evolution 31

Chapter 4 : Surface State Characterisation 37

4.1: Mathematical Modelling of Surface Topography 37

4.1 Surface Imaging Techniques 39

4.1.1. Optical Profilometry 39

4.1.2. Optical Microscopy 40

4.1.3 Scanning Electron Microscopy 44

4.2 Cavity Quantification 45

4.2.1 Image Thresholding Approach 45

4.3 GOA Ray-Tracing Model 48

4.3.1 Surface Replication Technique 52

Chapter 5 : Cavity Formation 56

5.1 Literature on Surface Cavity Formation 56

5.2 Factorial Design-of-Experiments Approach 60

5.2.1 2^k - Factorial Design for Cavity Formation/Flattening 60

5.2.2. Effect of Cold-Rolling on Cavity Flattening 69

Chapter 6 : ANN Spectral Emissivity Model 74

6.1 Introduction to Neural Networks 75

6.1.1. ANN Training Procedure 77

6.2 ANN Regression Model for Spectral Emissivity Predictions 79

6.2.1 ANN Training Data 81

6.2.2 Optimising the Network Topology 83

6.2.3 ANN Model Results 84

6.3 Global Sensitivity Analysis for ANN Inputs 86

6.3.1 Fourier Amplitude Sensitivity Testing 86

6.3.2 Numerical Implementation 88

6.3.3. Accounting for Correlated Inputs 90

6.3.4. Overall Sensitivity Indices 95

6.3.5. Wavelength Dependent Sensitivity Indices 97

6.3.6 Validation of Cavity Blackbody Assumption with GOA 99

6.4 Prospective Application and Future Improvements 100

6.4.1 On-Line Implementation for In-Situ Spectral Emissivity Prediction 100

6.4.2. Improving Accuracy and Uncertainty Quantification for ANN Model 102

Chapter 7 : Conclusions and Future Work **103**
7.1: Key Findings 103
7.2: Future Work 104
7.2.1 Predicting Radiative Property Evolution 104
7.2.2 Updated Heat Transfer Model 106
7.2.3 Improving ANN Spectral Emissivity Model 106
7.2.4 Combining All Improvements 107
References **108**
Appendix A: Replicate Measurements **116**
Appendix B: Normality of Surface Heights **117**
Appendix C: Scanning Area Selection & Summary Statistics **118**
Appendix D: Levenberg-Marquardt Algorithm **120**
Appendix E: Variance Computation **123**
Appendix F: Probability Distributions of ANN Input Data **125**
Appendix G: Iman and Conover Procedure **127**

List of Figures

Figure 1-1 Comparison of fuel efficiency and vehicle weight; reducing vehicle weight can have a positive impact on fuel consumption and hence greenhouse gas emissions [2]. 1

Figure 1-2: Comparison of tensile strengths and ductility of different steel grades (conventional HSS, 1st and 2nd generation AHSS, etc.) [3]. 2

Figure 1-3: AHSS manufacturing chain schematic adapted from Ref. [8]. This thesis analyses the effects of hot-rolling, acid-pickling and cold-rolling on the surface topography and the radiative properties of an AHSS coil before it enters an annealing furnace. 3

Figure 1-4: Iron-Carbon phase diagram showing the intercritical range (α – Ferrite, γ - Austenite). Figure adapted from Ref. [3] 4

Figure 1-5: Effect of quenching rate on microstructure formation during annealing. Figure adapted from Ref. [3]. 5

Figure 1-6: Schematic of a typical continuous galvanising line. 6

Figure 2-1: Schematic of a pyrometer measuring the surface temperature of a steel strip, showing the infinitesimal area, dA, the spectral intensity from the steel strip at the detection wavelength, $L'_\lambda(T, \lambda_d)$, the solid angle of measurement, $\Delta\Omega_d$, the detector area, A_d, and the signal generated by the pyrometer, S_λ. 14

Figure 2-2: Two configurations for a wedge-type pyrometer arrangement. (a) Here the wedge is created between the steel strip and the coil as the coil is unwound (image adapted from Ref. [21]). (b) Here, the wedge is created between the roller and the steel strip. The wedges, in both cases, make a virtual blackbody where the emissivity is approximately unity. 15

Figure 2-3: A schematic of the annealing furnace installed at Voestalpine Stahl GmbH in Linz, Austria. Image adapted from Ref. [33] 18

Figure 2-4: Heat-transfer model for predicting local strip temperature evolution through the furnace, where furnace surroundings are assumed to be large and isothermal. 20

Figure 3-1: Locations of extracted samples on the DP-780 coil, samples from the edge (E) and middle (M) of the coil are labelled with blue and red dots, respectively. The head, centre, and tail sections are marked as H, C, and T. [not to scale] 22

Figure 3-2: Spectral reflectivity of Infragold® and Spectralon® (coatings used in the two integrating spheres). In their respective operating ranges, the spectral reflectivities of both materials are larger than 0.9. The shaded areas show the operating ranges of the integrating spheres [36]. 23

Figure 3-3: Schematic of a Bruker A-562 Integrating Sphere [35] 24

Figure 3-4: Difference in spectral emissivity values between the Edge and Middle of the coil; the Edge samples show lower spectral emissivity values than the Mid samples. The amber-shaded area represents the NIR region important for pyrometry. Samples are from the (a) 20m Edge, (b) 75m Edge, (c) 1509m Mid, and (d) 450m Mid coil locations. 26

Figure 3-5: (a) Optical properties of pure Iron, and (b) the corresponding theoretical normal spectral emissivity. The optical properties are from Ordal et al. [38] and Johnson et al. [39] 27

Figure 3-6: Spectral directional emissivities at all 18 coil locations at the three common pyrometric wavelengths of (a) 1.6 μm, (b) 2.1 μm and (c) 2.4 μm. The coil's head, centre and tail sections have been shaded in green, yellow, and orange, respectively. 28

Figure 3-7: Variations in emissivity ratios and the associated temperature errors at common pyrometry wavelengths. Samples extracted from the edge (E) of the coil show larger emissivity ratio values than samples from the middle (M). The head, centre and tail sections are marked with H, C and T, respectively. (a) 1.6/2.1 μm, (b) 1.6/2.4 μm, (c) 2.1/2.4 μm 29

Figure 3-8: Effect of intercritical annealing temperature on the stress-strain behaviours of DP980 steels [40]. Different intercritical annealing temperatures cause significant variations in the steels' ultimate tensile strengths (UTS) and yield strengths (YS). 30

Figure 3-9: Conversion factors for converting normal emissivities to hemispherical emissivities. Adapted from Ref. [44]. 32

Figure 3-10: Spectral hemispherical emissivity curve for one of the samples, which have been curve-fit using a power law function, overlaid with the blackbody spectral intensity (given by Planck's distribution). 32

Figure 3-11: Total hemispherical absorptivity variations (at $T_{furnace}$ = 850°C) along the length and width of the coil. Samples from the head, centre and tail sections are shaded in green, yellow, and orange, respectively. 33

Figure 3-12: Representative furnace temperature profiles for DP780 (blue) and DP980 (red) alloys, taken from Somveille et al. [27]. These furnace temperature profiles have been used to model strip temperature evolutions in this study. 34

Figure 3-13: Specific heat for DP-980 as a function of temperature, where the relationship follows a quadratic behaviour [45]. These values have been applied for both the DP780 and DP980 heating schedules, as it is challenging to obtain these relationships for all DP grades. ... 34

Figure 3-14: Expected temperature evolutions of two samples showning large differences in total hemispherical absorptivities. Temperature profiles for typical (a) DP780 and (b) DP980 alloys. 35

Figure 3-15: The temperatures of different coil locations at various distances into the furnace. The middle of the coil changes in temperature faster than the edge. This diagram follows the DP-980 heating schedule. 36

Figure 4-1: Optical profilograms of a subset of samples. The total hemispherical absorptivity (α) values presented are computed at $T_{furnace}$ = 850 °C. 39

Figure 4-2: Optical micrographs of the ten selected samples taken with a lateral resolution of 0.104 μm. At this magnification, a larger number of dark patches are visible on the surfaces of the Mid samples compared to the Edge samples. 41

Figure 4-3: 3D digitised surface height maps obtained using the Keyence optical microscope for two select samples (20m Edge and 1509m Mid samples). 42

Figure 4-4: Relationship between surface slope and total hemispherical absorptivity for the ten analysed samples in Figure 4-2. 43

Figure 4-5: Comparison of an optical image and an SEM image (20kV) taken at the same location on the 1509m Mid sample. The SEM image reveals a highly corrugated surface inside the dark patches 44

Figure 4-6: Effect of gamma correction on the contrast of a subset of samples. This procedure allows for normalising images in the case of varying microscope imaging characteristics like exposure and lighting settings 45

Figure 4-7: Binary image of the cavity shown in Figure 4-5. The correct regions have been identified using the image thresholding approach. 46

Figure 4-8: Relationship between cavity percentage and total hemispherical absorptivity over the ten analysed samples in Figure 4-2 and Table 4-1. 47

Figure 4-9: (a) Parameters used to define the BRDF. (b) The path of an incident ray as it interacts with a random Gaussian surface. 49

Figure 4-10: GOA spectral emissivity predictions for a subset of samples, comparing GOA results between the (a) and (c) Edge and the (b) and (d) Middle of coil. 51

Figure 4-11: Surface replication apparatus, Top: Application gun, Bottom: 1509m Mid sample and its replicate 52

Figure 4-12: Surface height profile of the cavity shown in Figure 4-5 obtained by imaging the (a) original steel surface and (b) the replicate surface. 53

Figure 4-13: Linear height profiles along the red dotted lines. The replicate profile reveals a much rougher surface inside the cavity. A larger number of higher order scattering events are also visible which contribute to the higher spectral emissivities and total hemispherical absorptivities. 53

Figure 4-14: Comparison of cavity surface taken using an SEM at 54°, and the replicant surface height profile at 54°. The red circles represent the surface peaks visible in both the SEM image and the replicant surface height profile. 54

Figure 4-15: GOA spectral emissivity predictions using the surface height profile from the replicant technique. An improved GOA prediction is obtained within its validity domain. 55

Figure 5-1: Selective oxidation in the oxygen depletion zone created between external oxide scale and the steel substrate after the (a) hot-rolling process. Some of these oxide nodules are dissolved during (b) pickling and subsequently get flattened during (c) cold-rolling. Image adapted from Ref. [51]. Dashed lines represent grain boundaries. 56

Figure 5-2: Surface cavities seen in samples analysed by Köpper et al [51], the cross-section SEM image of the surface with cavities shows cracks along the grain boundaries due to oxide dissolution during pickling. 57

Figure 5-3: SEM cross-section images of one of the analysed samples (pickled to ~50s) provided by our industrial partner. External and grain boundary oxides are removed by pickling leading to a roughened substrate surface and surface cavities, post-pickling. (SEM Images from partner). Higher magnification SEM images are required to ascertain if oxide nodules are present on the surface, as performed in Ref. [46].. 58

Figure 5-4: Similarity of the reflectivities of under-pickled samples and those of certain annealed samples showing oxide nodules, analysed by Lin et al. [46].. 59

Figure 5-5: External oxide scale remnant visible on certain under-pickled samples represented by amber region in Figure 5-1. 59

Figure 5-6: Optical micrographs of samples representing the 8 treatment combinations analysed through the 2^3 - factorial design. Fewer dark patches are observed as the cold-rolling reduction is increased from 1% to 53%. 62

Figure 5-7: Percentage contributions of the processing parameters on the response variables. At all wavelengths, the cold-rolling reduction percentage strongly dominates the radiative properties.. 66

Figure 5-8: Normal probability plots of the effects of each factor on each response variable. All effects lie close to the normal line except for the cold-rolling reduction percentage. (a) Cavity Percentage, (b) average emissivity, spectral emissivities at (c) 1.6, (d) 2.1, (e) 2.4, (f) 5, (g) 10, and (h) 20 μm. The red arrow identifies the effect of the cold-rolling reduction percentage....... 68

Figure 5-9: Scatter plots of cold-rolling reduction percentage against (a) cavity %, (b) average spectral emissivity, (c) spectral emissivity at $\lambda = 2.4$ μm and (d) spectral emissivity at $\lambda = 20$ μm. There are six replicates at each cold-rolling reduction value. Similar variations are observed in the number of surface cavities and radiative properties across the DP780 coil in Chapters 3 and 4, as shown by the red ovals. 69

Figure 5-10: Normal probability and histograms for the residuals of (a) cavity percentage, (b) average spectral emissivity between 0.5 and 20μm, and spectral emissivities at (c) 2.4 and (d) 20μm. 72

Figure 6-1: A multi-layer perceptron network (MLP) schematic with an input layer, a set of hidden layers, and an output layer. x, y and y□ represent the inputs, outputs, and predicted values. e is the residual between y and y□□□The neuron marked by the red-dashed box represents a hypothetical j^{th} neuron in the n^{th} layer. 75

Figure 6-2: Computing the output of the j^{th} neuron in the n^{th} layer. This neuron is highlighted by the dotted red box in Figure 6-1.. 76

Figure 6-3: ANN training flow to optimise the weights and biases. The value for n is set to MATLAB®'s default value of 6. An example training process is also shown where the lowest error on the validation dataset is achieved at the seventh epoch. 78

Figure 6-4: Proposed ANN model for inferring the spectral emissivities of AHSS in their cold-rolled condition before entering the annealing furnace. 79

Figure 6-5: Limitation of a neural network in modelling the interaction effect between two variables. 80

Figure 6-6: Spectral directional emissivities of all 164 samples. (a) Dataset 1, (b) dataset 2, (c) dataset 3. Samples from dataset 3 show the greatest variance in spectral emissivities, as those samples are acid-pickled and cold-rolled to various extents. 81

Figure 6-7: Optical micrographs showing varying amounts of surface cavitation amongst the samples analysed from datasets 1, 2 and 3. The reported lengths (75m, 450m and 880m) for samples from dataset 1 represent the axial location along the length of the DP780 coil. 82

Figure 6-8: Choosing optimum number of hidden neurons and layers through a grid-search approach. A single hidden layer with five neurons yields the lowest error on the testing dataset. As such, a single hidden layer with five neurons is chosen. 83

Figure 6-9: Comparison of neural network predictions and the measured spectral emissivities. Predictions from GOA simulations are also presented. Unfortunately, the GOA predictions for surfaces with many cavities are poor as the topography inside the cavities is not captured by optical microscope. 84

Figure 6-10: Residual analysis of all samples in the testing dataset (dataset 1), the mostly normal residuals signify the validity of the ANN model. 85

Figure 6-11: Exploration of the probability space of each input for a hypothetical model with three input parameters when sampling through Eq. (41), using (a) linearly dependent and (b) independent frequency sets. 89

Figure 6-12: Pearson rank correlation structures of (a) experimental data from datasets 1, 2, and 3, (b) samples generated using Eq. (6.4) ($x10^{-5}$), and (c) FAST-C samples after Iman and Conover restructuring. 91

Figure 6-13: Two hypothetical surfaces with the same RMS roughness but with drastically different surface slopes due to differences in their correlation lengths. 92

Figure 6-14: (a) Original and (b) altered oscillation frequencies for the refractive index after restructuring using the Iman and Conover [36] procedure. 93

Figure 6-15: Example showing the restoration of the characteristic oscillation behaviour for a given input i. Here, XW_i examples are given for the hypothetical inputs 2 and 4. 94

Figure 6-16: Overall sensitivity indices for non-dimensional input parameter groups; (a) assumes that that the non-dimensional groups are independent, while (b) accounts for the correlation structure amongst the inputs shown in Figure 6-12 (c). 95

Figure 6-17: Sensitivity indices and distributions of the wavelength-normalised RMS roughness and surface slopes of the exposed area of samples analysed in datasets 1, 2, and 3, overlayed on the regime map by Tang et al. [49]. The wavelength-normalised RMS roughness differentiates between the EM, specular and GOA domains, as such has a higher sensitivity index compared to surface slope.......... 96

Figure 6-18: Impact of surface topography parameters on spectral emissivity at different wavelengths of incident light between 0.5 and 20 μm. The surface slope values are (a) sampled from the kernel distribution fit to data in datasets 1,2 and 3 (see Appendix C), (b) sampled from a uniform distribution with Min and Max values of 0.2 and 0.55, (c) sampled from a uniform distribution with Min and Max values of 0.2 and 0.75.......... 98

Figure 6-19: GOA spectral emissivity predictions by setting the areas covered by the cavities as blackbodies for two select samples with many cavities, (a) 450m Mid and (b) 880m Mid.......... 99

Figure 6-20: On-line microscope for imaging the strip surface at different coil locations along its width, where the microscope can move along rails. [63] 100

Figure 6-21: (a) Surface height-map acquisition by Amepa microscope, through the line projection method. (b) Generated 3D height map for an examples surface [65].......... 101

List of Tables

Table 4-1: Summary of roughness statistics and total hemispherical absorptivities for samples analysed using the digital microscope shown in Figure 4-2. 43

Table 5-1: Factors and their respective levels used in the 2^3 model. 61

Table 5-2: Analysed samples using the three factors, their respective cavity percentages and average emissivities (computed between $\lambda = 0.5 - 20\mu m$). All reported wavelengths in μm. The runs represent the eight samples analysed in Figure 5-6. 61

Table 5-3: Algebraic signs for combining the values of the response variables at the different treatment combinations (samples in Table 5-2) to compute the individual and combined factor effects. 63

Table 5-4: Factor effects, their contrasts, and their sum of squares for each response variable. The percentage contributions of each factor have also been shown. 65

Table 5-5: Testing of cavity percentage, average spectral emissivity and select (2.4μm and 20μm) spectral emissivity residuals for normality using various normality tests. Most tests identify the residuals for all response variables to be normal. 71

List of Abbreviations

Below are abbreviations used in this thesis classified according to the context in which they appear and listed alphabetically.

Steels & Annealing	
AHSS	Advanced High-Strength Steels
CGL	Continuous Galvanising Line
DP	Dual-Phase
GHG	Greenhouse Gas Emissions
HSLA	High-Strength Low Alloy
TRIP	Transformation Induced Plasticity
UTS	Ultimate Tensile Strength
YS	Yield Strength
Radiative Properties & Surface Characterisation	
ACF	Auto-Covariance Function
BRDF	Bi-directional Reflectance Distribution Function
CCD	Charged Coupled Device
EM	Electromagnetic
FOV	Field of View
FTIR	Fourier Transform Infra-Red
HDF	Height Distribution Function
MIR	Mid-Infra-Red
NIR	Near-Infra-Red
RGB	Red, Green, Blue (Pixel Intensity Channels)
RMS	Root-Mean-Squared
SEM	Scanning Electron Microscopy
XRD	X-Ray Diffraction
Radiative Property & Heat-Transfer Modelling	
ANN	Artificial Neural Networks
BNN	Bayesian Neural Networks
CA	Cellular Automata
CDF	Cumulative Distribution Function
CNN	Convolutional Neural Networks
FAST	Fourier Amplitude Sensitivity Testing
FDTD	Finite Difference Time Domain
GOA	Geometric-Optics Approximation
GSA	Global Sensitivity Analysis
IC	Iman and Conover

LMA	Levenberg-Marquardt Algorithm
MCMC	Monte-Carlo Markov’s Chain
MCRT	Monte-Carlo Ray-Tracing
MLP	Multi-Layer Perceptrons
MSE	Mean-Squared Error
PDF	Probability Distribution Function

Nomenclature

This section summarises the symbols used in this thesis, classified according to the context in which they appear.

Metallurgy	
α	Ferrite
α'	Martensite
P	Pearlite
γ	Austenite
T_{Ac1}	Eutectoid Temperature (Beginning of austentisation)
T_{Ac3}	Austentisation Completion Temperature
Radiative Properties & Pyrometry	
S_λ	The signal generated by the pyrometer due to radiant flux from a target surface
κ_λ	Quantum efficiency of a photonic sensor
Q_e	Surface radiant flux
λ_d	Pyrometric detection wavelength
T	Target surface temperature
T_sw	Single-wavelength pyrometric temperature
T_dw	Dual-wavelength pyrometric temperature
$L'_{\lambda,\mathrm{b}}$	The spectral intensity of a blackbody at a given wavelength
L'_λ	The spectral intensity of the target surface at a given wavelength
$L'_{\lambda,\mathrm{meas.}}$	Measured spectral intensity
$L'_{\lambda,\mathrm{gen}}$	Generated spectral intensity using an emissivity parameter set and surface temperature
ε'_λ	Spectral directional emissivity
α'_λ	Spectral directional absorptivity
ε	Total hemispherical emissivity
α	Total hemispherical absorptivity
$\varepsilon_{\mathrm{r,P}}$	Expected emissivity ratio (dual wavelength pyrometry)
$\varepsilon_{\mathrm{r,T}}$	True emissivity ratio (dual wavelength pyrometry)
θ_p	The angle at which the pyrometer views the steel surface
φ	The azimuthal angle of incidence or emission
Ω	Solid angle viewed the pyrometer
A_d	Area of the photonic sensor
C_1	$2\cdot h\cdot c^2 = 3.7481 \times 10^{-16}$ Wm^2
C_2	$h\cdot c/k_\mathrm{B} = 1.439 \times 10^4$
h	Planck's constant
c	The speed of light in a vacuum

C_λ	The calibration constant of a pyrometric sensor
a_0, a_1 ,.., a_m	Polynomial coefficients of emissivity function in multi-wavelength pyrometry
Furnace Heat Transfer Model	
ρ_s	Steel sheet density
$C_{p,s}$	Steel sheet specific heat capacity
t_s	Steel Sheet thickness
k_s	Steel sheet thermal conductivity
l_s	Steel Sheet length
w_s	Steel Sheet width
$T_{s,\ loc.}$	Local steel sheet temperature
x, $(\tilde{x})$	The distance along sheet length (non-dimensional length)
y, $(\tilde{y})$	The distance along sheet width (non-dimensional width)
z, $(\tilde{z})$	The distance along sheet thickness (non-dimensional thickness)
v	The velocity of the steel sheet through the furnace
t, $(\tilde{t})$	Time (non-dimensional time)
x_f	Distance into furnace
$\dot{q}_{rad,in}$	Incoming radiative heat-flux
$\dot{q}_{rad,out}$	Outgoing radiative heat-flux
$T_{f,\ loc.}$	Local furnace temperature
σ	Stefan-Boltzmann Constant
θ_e	Polar angle of emission from the steel surface
θ_i	Polar angle of incidence onto the steel surface
Integrating Sphere and Reflectance Measurements	
$V_{std,\ s}$	The spectrum obtained with the standard in port and beam shone onto the port
$V_{sample,\ s}$	The spectrum obtained with the sample in port and the beam shone onto the port
$V_{std,\ ref}$	The spectrum obtained with the standard in port and beam shone onto the reference spot
$V_{sample,\ ref}$	The spectrum obtained with the sample in port and beam shone onto the reference spot
$\rho_{\lambda,\ d\text{-}h}$	Spectral directional-hemispherical reflectivity
ρ_{std}	Reflectance spectra of the standard
$\rho_{\lambda,\ n}$	Normal spectral reflectance
n	The refractive index of the substrate
k	The extinction coefficient of the substrate
ϵ_{im}	The imaginary permittivity of the substrate = $2nk$
Surface Topography Characterisation	
R_q	Root-mean-squared roughness

τ	Correlation length
s_r	Surface slope
$p(h)$	Probability distribution of surface heights
$C(x, y)$	Auto-covariance function
C_r, C_p	Cavity ratio, cavity percentage
L_x	Length of the surface along the x direction
L_y	Length of the surface along the y direction
GOA Ray-Tracing Model	
$\rho_\lambda(\Omega_\mathrm{i}, \Omega_\mathrm{r})$	Bi-directional reflectance distribution function (BRDF)
Ω_i	The direction of incidence (Solid Angle)
Ω_r	The direction of reflection (Solid Angle)
$\rho_{\lambda,\mathrm{d-h}}(\Omega_\mathrm{i})$	Spectral-directional hemispherical reflectance for a given incidence direction
$e_{\mathrm{r, s}}$	The energy of the s-polarised reflected ray
$e_{\mathrm{r, p}}$	The energy of the p-polarised reflected ray
$e_{\mathrm{i, s}}$	The energy of the s-polarised incident ray
$e_{\mathrm{i, p}}$	The energy of the p-polarised incident ray
ρ_{ss}	SS co-polarised reflectivity
ρ_{sp}	SP cross-polarised reflectivity
ρ_{pp}	PP co-polarised reflectivity
ρ_{ps}	PS cross-polarised reflectivity
R_s	Fresnel amplitude reflectivity (s-polarised)
R_p	Fresnel amplitude reflectivity (p-polarised)
$\mathbf{v}_\mathrm{i}$	Vector of the incident beam
$\mathbf{v}_\mathrm{r}$	Vector of the reflected beam
$\mathbf{n}$	The local normal of the surface at the reflection point
Factorial Design for Cavity Formation	
C_i	The contrast of the i^{th} independent variable
E_i	The effect of the i^{th} independent variable
SS_i	The sum of squares of the i^{th} independent variable
n	Number of replicates
Neural Networks	
$\mathbf{X}$	A matrix of input values
$\mathbf{Y}$	A matrix of output values
$w^{(\mathrm{n})}_{\mathrm{i,j}}$	The weight of the i^{th} connection to the j^{th} neuron in the n^{th} layer
$x^{(\mathrm{n})}_{\mathrm{i,j}}$	The i^{th} input to the j^{th} neuron in the n^{th} layer
$b^{(\mathrm{n})}_{\mathrm{j}}$	The bias of the j^{th} neuron in the n^{th} layer
$z^{(\mathrm{n})}_{\mathrm{j}}$	The output of the j^{th} neuron in the n^{th} layer
ψ	The tan-sigmoid activation function

N	Number of training samples
$\mathbf{e}$	The residual vector between ground-truth and predicted outputs
FAST-C Sensitivity Analysis	
f	The analysed model
$\mathbf{y}$	The output parameters of the model
$\mathbf{x}$	The input parameters to the model
r	Number of input parameters to the model
s	The common parameter ranging between $-\pi$ and π
ω_i	Integer frequency of the ith input parameter
$\boldsymbol{\omega}$	A vector of all integer frequencies
F	The marginal cumulative distribution function (CDF) of the ith input
A_0	0th Fourier Coefficient
A_p	First Fourier Coefficient
B_p	Second Fourier Coefficient
V	The overall variance of the output across all input-output pairs
V_i	Variance contribution of the ith input parameter to the output
p	The Fourier term
σ_i	Sensitivity index of the ith input parameter
$\mathbf{s}$	A vector containing the common parameters for numerical implementation
$\mathbf{X}$	The matrix of inputs for numerical implementation
M	The order of interference or harmonic of the integer frequencies
N	Number of required samples
Iman and Conover Procedure	
$\mathbf{X}$	The matrix of inputs to be reordered
$\mathbf{C}$	The required Pearson rank-correlation structure among the inputs
RANKS	The matrix containing the ranks of values in each column of **X**
$\mathbf{B}$	The matrix containing the Van der Waerden scores of ranks in **RANKS**
Φ	The cumulative distribution function of a standard normal distribution
CS	The Pearson rank-correlation structure of **B**
$\mathbf{Q}$	The lower triangular Cholesky decomposition of **CS**
$\mathbf{P}$	The lower triangular Cholesky decomposition of **C**
$\mathbf{T}$	A transformation matrix to introduce the required correlation structure to **B**
$\mathbf{Y}$	A matrix containing the transformed Van der Waerden scores in **B** with correlation structure **C**
$\mathbf{R}$	A matrix with ranks of values in each column of **Y**
$\mathbf{W}$	A matrix with permuted values of **X** with rank-correlation structure **C**, and the original marginal cumulative distributions of inputs in **X**

Quote

If I have seen further, it is by standing upon the shoulders of giants.

- *Sir Isaac Newton*

Chapter 1 : Overview and Industrial Motivation

This chapter introduces advanced high-strength steels (AHSS) and continuous annealing. It discusses the advantages of AHSS over conventional high-strength low alloy (HSLA) steels and their use in the automotive industry. A brief overview of other processes in its manufacturing chain, such as hot-rolling, acid pickling and cold-rolling is also provided. The chapter concludes with an outline of the thesis.

1.1: Introduction to Advanced High-Strength Steels

With increasing crashworthiness and emissions regulations, automakers rely on high-strength materials to reduce vehicle weight through downgauging (i.e., using thinner components to reduce overall vehicle weight) [1]. Automotive lightweighting can profoundly reduce fuel consumption and greenhouse gas emissions, as shown in Figure 1-1 [2].

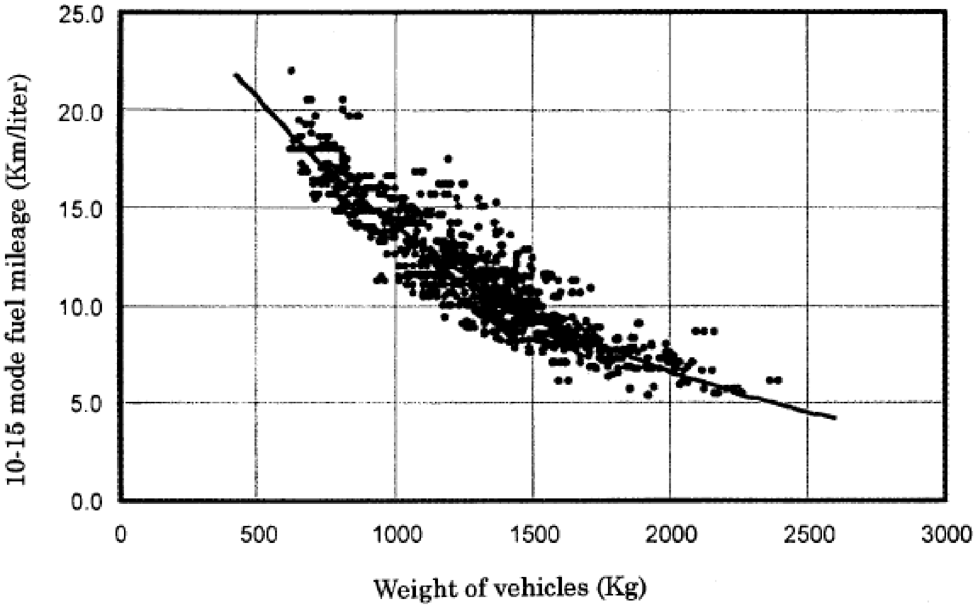

Figure 1-1 Comparison of fuel efficiency and vehicle weight; reducing vehicle weight can have a positive impact on fuel consumption and hence greenhouse gas emissions [2].

Consequently, the use of AHSS in automobiles has increased considerably, as they provide improved tensile strengths (allowing for downgauging) compared to HSLA steels while maintaining ductility. Figure 1-2 compares the tensile strengths and ductility of various steel grades. This work focuses on first-generation advanced high-strength steels, particularly the more widely used dual-phase (DP) ferrite-martensite ($\alpha + \alpha'$) grades.

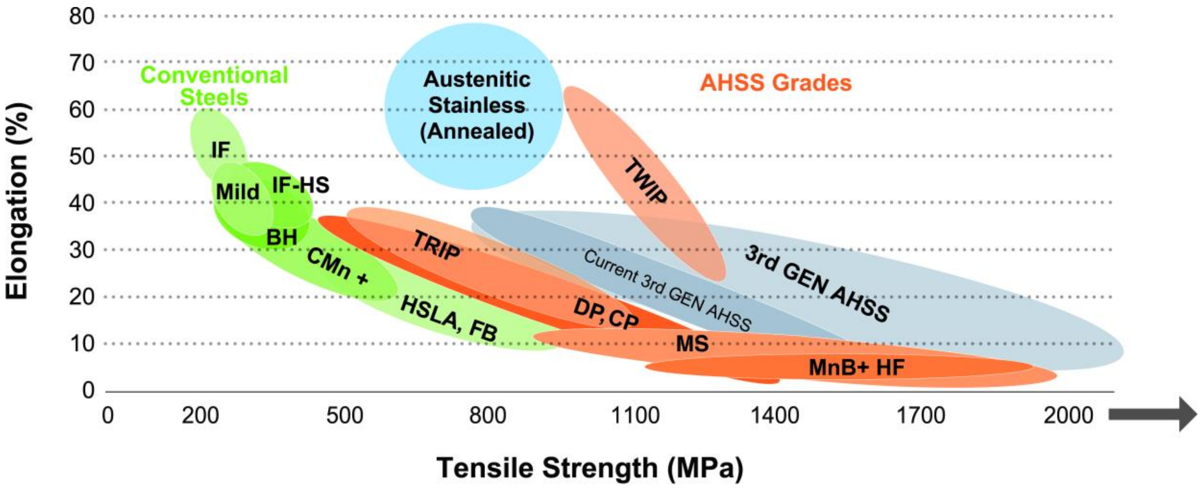

Figure 1-2: Comparison of tensile strengths and ductility of different steel grades (conventional HSS, 1st and 2nd generation AHSS, etc.) [3]. The mechanical properties of 3rd generation AHSS are even more sensitive to temperature excursions due to their complex micro-structures. Therefore, characterising the impact of radiative properties of AHSS on temperature excursions is very important with the rise of 3rd generation grades.

Automakers have also experimented with other low-density non-ferrous metals such as Aluminium and Magnesium and other materials like Carbon-fibre Reinforced Polymers; however, producing these materials results in 7-20 times [4] more GHG emissions than steel. Furthermore, since 30-35% of an automobile's life cycle GHG emissions originate from its production [4], increased GHG emissions from these low-density materials outweigh the reduction in tailpipe emissions. Therefore, AHSS are expected to remain a primary material in the automotive industry and are the focus of the thesis [4].

1.2: AHSS Manufacturing Process

This section introduces the AHSS manufacturing process from casting to galvanising on a continuous galvanising line (CGL). This thesis analyses AHSS samples processed on an industrial line before annealing, as shown in Figure 1-3. The chapter also discusses the microstructure formation of dual-phase steels and the annealing process.

1.2.1 Manufacturing Chain

Manufacturing of AHSS begins with casting, as shown in Figure 1-3, where molten steel is cooled using water jets while being poured into a continuous mould, allowing it to harden into slabs [5]. The slabs are subsequently hot-rolled above their recrystallisation temperature. Hot-rolling allows for reorienting the crystal lattice structure of the steel creating thinner sheets with minimal strain-hardening [6].

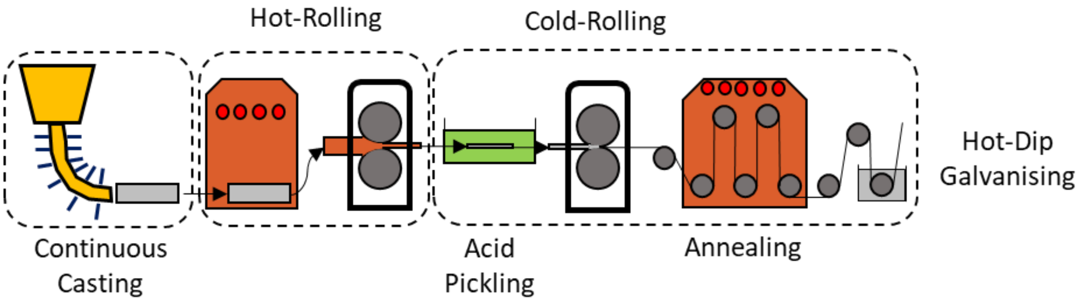

Figure 1-3: AHSS manufacturing chain schematic adapted from Ref. [7]. This thesis analyses the effects of hot-rolling, acid-pickling and cold-rolling on the surface topography and the radiative properties of an AHSS coil before it enters an annealing furnace.

The high temperatures in the hot-rolling process produce iron-oxide scale formation on the steel substrate [8] that must be removed using descaling acid-pickling process, usually performed using Hydrochloric (HCl) or Sulphuric (H_2SO_4) acid [9]. Next, the steel coil is cold-rolled (below recrystallization temperature) to reduce its thickness further and alter its surface state, improving the adhesion of surface coatings such as molten zinc during hot-dip galvanising. Cold-rolling leads to the strengthening of the material; and a reduction in ductility due to strain-hardening [6]. The steel is then heat-treated above its austentisation temperature during annealing [1, 10] to achieve the required mechanical properties on CGLs, followed by hot-dip galvanising.

1.2.2 Annealing Process and Microstructure

Annealing is an essential heat-treatment process to achieve the desired AHSS microstructure [1, 10]. In its final form, the martensitic volume fraction ($V_{\alpha'}$) strongly influences the strength of DP steels; and its formation depends on the applied heating schedule and carbon content [1, 11, 12]. Cold-rolled steel has a ferrite-pearlite (α + P) microstructure, which is transformed into a ferrite-martensite (α + α′) microstructure through annealing [1, 10].

Intercritical annealing heats the steel to a temperature between the austentisation onset (T_{Ac1}, also known as the eutectoid temperature) and completion (T_{Ac3}) temperatures. These temperatures define the *intercritical range* [1, 10] where ferrite and austenite are present, as shown in the Iron-Carbon phase diagram in Figure 1-4. The steel soaks at the intercritical annealing temperature for a set time and is then quenched to room temperature to attain the required microstructure, as shown in Figure 1-5.

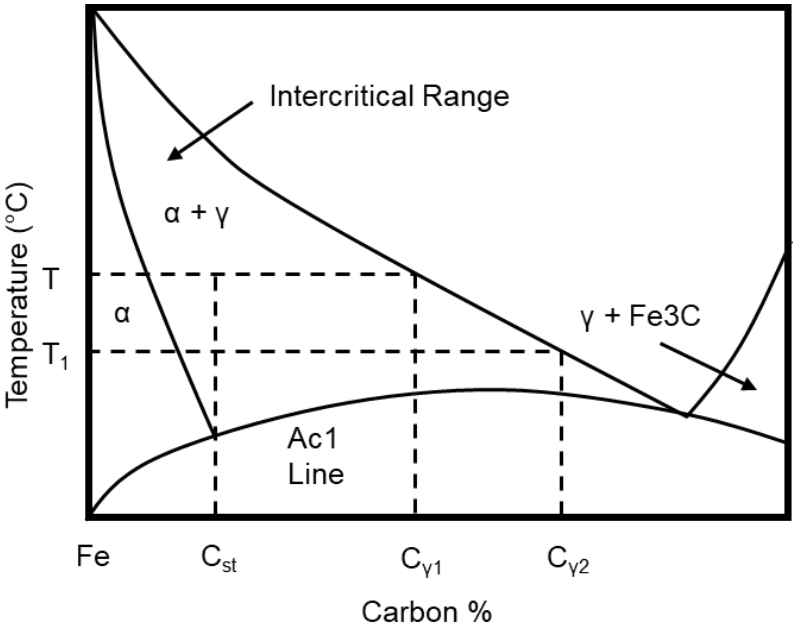

Figure 1-4: Iron-Carbon phase diagram showing the intercritical range (α – Ferrite, γ - Austenite). Figure adapted from Ref. [10].

During the intercritical soak, a proportion of ferrite (α) and all pearlite (P) is transformed to austenite (γ), creating a ferrite-austenite (α + γ) microstructure. Lastly, upon quenching to room temperature, the remaining austenite transforms to martensite (α′), finally creating the ferrite-martensite (α + α′) microstructure in the case of DP steels. The intercritical annealing temperature influences the amount of austenite (γ) formed and, in turn, the amount of martensite (α′) after quenching. Therefore, the quenching rate affects the microstructure and the steel grade created [10], as shown in Figure 1-5.

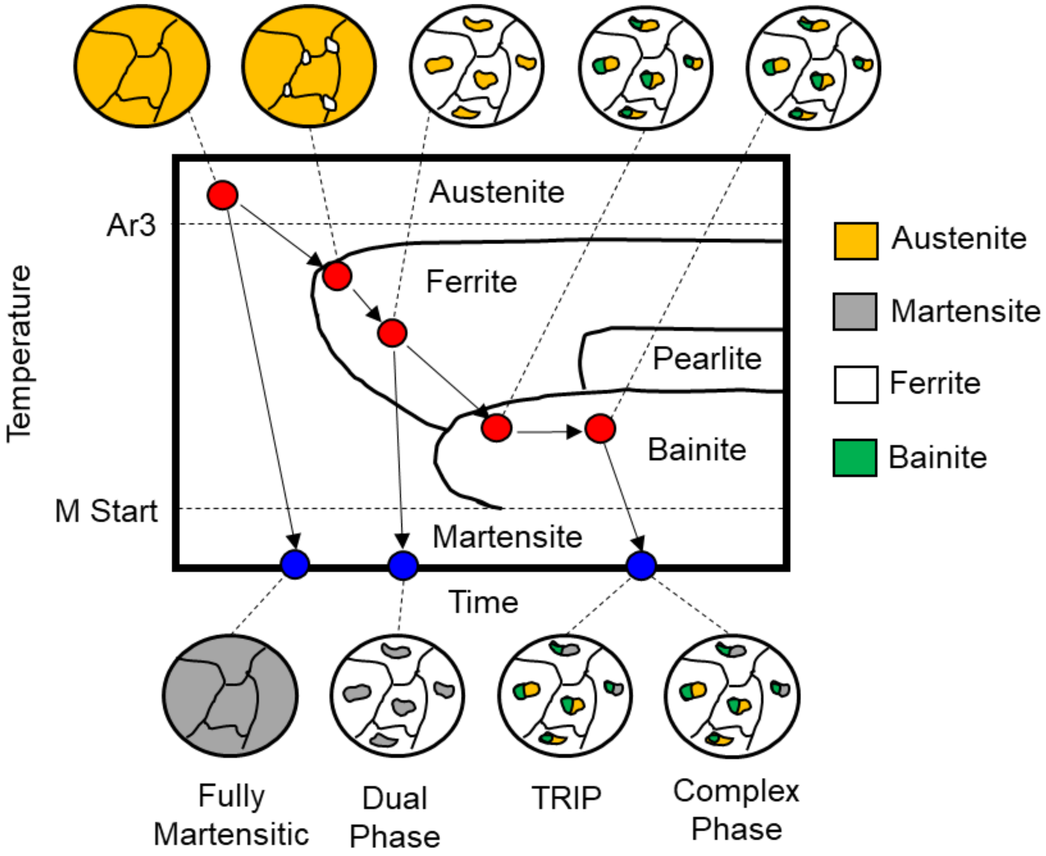

Figure 1-5: Effect of quenching rate on microstructure formation during annealing. Figure adapted from Ref. [10].

1.2.3 Continuous Galvanising Lines

Intercritical annealing is performed before hot-dip galvanising on a CGL, illustrated schematically in Figure 1-6.

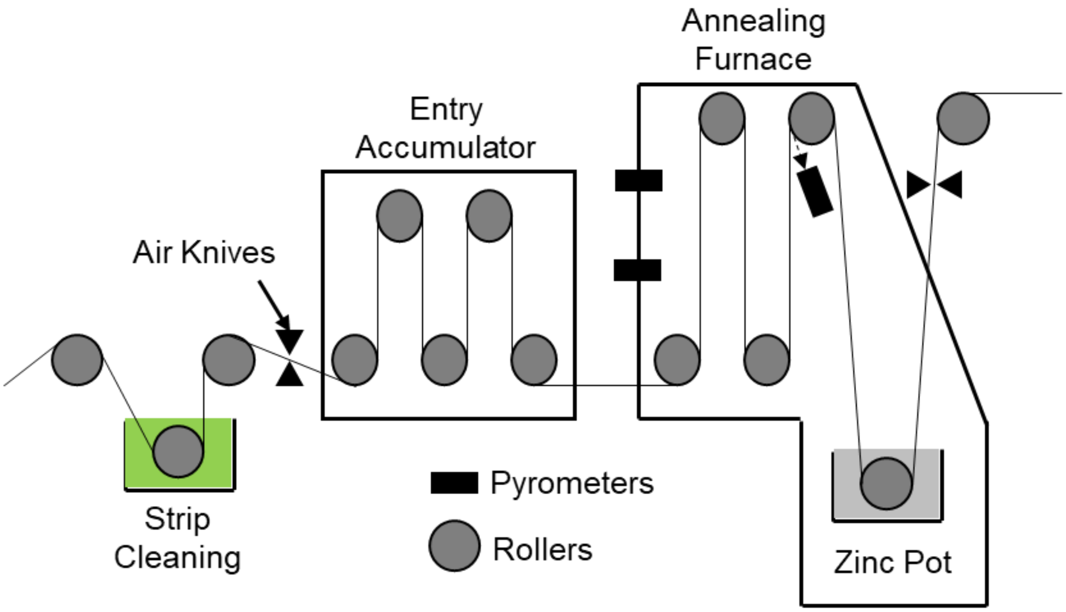

Figure 1-6: Schematic of a typical continuous galvanising line.

Steel coils are unwound and initially welded to the end of the existing coil on the line. The entry accumulator is necessary to keep the continuous annealing furnace operational when welding the new and old coils. The coil subsequently passes through the annealing furnace and then through the molten zinc bath, where it becomes coated with zinc. Annealing is usually performed in a reducing atmosphere comprised of 95% N_2 and 5% H_2 (by vol.) to minimise oxidation of the steel strip [13].

During annealing, the steel strip may experience temperature excursions leading to erratic microstructure changes, causing non-uniform mechanical properties post-annealing. The industry has often attributed these temperature excursions to non-uniform irradiation of the steel strip caused by improper furnace design [14, 15]. However, variations in radiative properties across steel coils may also cause temperature excursions.

Temperature evolution of the steel coil through the annealing furnace is influenced strongly by its radiative properties by altering the strip thermal absorption rate, as radiation is the dominant form of heat transfer due to high temperatures in the furnace [15, 16]. Additionally, furnace temperature control algorithms use pyrometrically inferred strip temperatures as feedback. Pyrometry relies on the spectral irradiance from the steel strip, which is influenced strongly by its radiative properties. Therefore, radiative property variations can also cause furnace temperature control errors through incorrectly inferred pyrometric temperature measurements.

1.3 Research Motivation & Objectives

Given the sensitivity of microstructure evolution to the intercritical annealing temperature, it becomes paramount for steel manufacturers and operators to understand the impact of radiative property variations on strip temperature excursions. Various studies have analysed the evolving AHSS radiative properties during annealing through physics-based and data-driven models. However, the literature has overlooked characterising radiative property variations across a single AHSS coil in its cold-rolled and pre-annealed condition. This thesis fills this knowledge gap and helps explain that upstream processes (of annealing) can also influence the radiative properties of AHSS to an extent, affecting the post-annealed mechanical properties.

As such, the primary objectives of this thesis are to:

I. Characterise radiative property variations across a single AHSS coil in its pre-annealed condition before it enters the annealing line through ex-situ reflectivity measurements of samples extracted from various locations on an AHSS coil fully processed on the industrial line (hot-rolled, acid-pickled, and cold-rolled).

II. Explore the likely impact of these radiative property variations on pyrometrically inferred strip temperatures, strip temperature evolution, and, in turn, strip mechanical properties.

III. Correlate radiative property variations with differences in the surface state through a geometric-optics-approximation (GOA) ray-tracing algorithm and an artificial neural network model. The ANN may be useful for inferring radiative property variations across a single coil before it enters the annealing line in conjunction with on-line strip imaging microscopes.

IV. Use a global sensitivity analysis (GSA) to establish functional dependencies between the various surface topography parameters and the spectral emissivity of strip surfaces, addressing the black-box nature of ANNs.

V. Explore possible reasons for the variations in surface topography across the coil, which lead to the differences in radiative properties. A factorial design analysis addresses the impact of the upstream processes such as acid-pickling and cold-rolling.

1.4 Overview of Thesis

The following provides a summary of each chapter in the thesis:

Chapter 2 includes a literature review; it introduces the three common types of pyrometry (single-, dual- and multi-wavelength) used in industry and discusses annealing furnace design in greater detail. The chapter introduces a preliminary heat transfer model for predicting steel strip temperature evolution, elucidating the importance of understanding steel strip radiative property variations for accurate strip temperature control.

Chapter 3 introduces the experimental work to analyse the *ex-situ* radiative properties of samples extracted from various coil locations on a hot-rolled, acid-pickled, and cold-rolled DP-780 coil processed on an industrial line. The chapter reviews the workings of an integrating sphere and procedures followed to infer the spectral reflectivities, emissivities and total absorptivities of the AHSS samples.

Chapter 4 outlines the work performed in characterising the surface topographies of the samples through optical profilometry, optical microscopy, and scanning electron microscopy (SEM). This chapter establishes a strong correlation between strip radiative properties and cavities on the strip surface through image thresholding of strip optical imagery. The chapter then uses a GOA ray-tracing approach to correlate the surface topography with radiative properties. Lastly, the chapter discusses the replicate technique used to improve surface height map acquisition inside the cavities and hence the GOA predictions. The findings from Chapters 3 and 4 are disseminated as a journal paper in *Steel Research International* [17].

Chapter 5 discusses possible causes for surface cavity formation. Previous studies attribute cavity formation to the dissolution of selective grain boundary oxides (formed during hot rolling) during acid-pickling, which leads to micro-topographical changes to the strip surface. This study shows that the area occupied by the cavities after cold-rolling is linearly proportional to the cold-rolling reduction percentage. However, they are non-uniformly flattened due to non-homogeneous cold-rolling characteristics across single AHSS coils. The chapter finally explores the combined effect of acid pickling time and cold rolling thickness reduction percentage on the surface cavity coverage through a factorial design-of-experiments procedure.

Chapter 6 discusses using a data-driven machine learning model to correlate strip spectral emissivities with surface topography parameters using an ANN; it then evaluates the functional dependencies of spectral emissivity on the topographical parameters through a Fourier amplitude sensitivity test (FAST). Upcoming, *in-situ* strip imaging technologies allow operators to obtain surface roughness measurements and microscope imagery of the strip surface in real time. The ANN may prove helpful in conjunction with these imaging techniques for on-line spectral emissivity predictions before a coil section enters an annealing furnace. In addition, manufacturers may use these *in-situ* measurements to update furnace temperature control and pyrometry algorithms.

Some of the findings from Chapter 6 were presented as conference proceedings at Materials Science & Technology 2022 in Pittsburgh, PA, and are included in a conference paper for the 10th International Symposium on Radiative Transfer 2023 (ISRT) in Thessaloniki, Greece. In addition, an extended version of the ISRT paper, including the FAST analysis, will be submitted to the Journal of Quantitative Spectroscopy and Radiative Transfer (JQSRT).

Lastly, Chapter 7 summarises the research and provides recommendations for future work.

1.5 Research Contributors

Below are researchers who contributed to some of the results, listed according to the order in which they appear.

1. Mr. Devon Hartlen performed optical imagery of the initial set of DP780 samples shown in Figure 4-2 using the Keyence optical microscope.
2. Dr. Nina Heinig and Dr. Lei Zhang are responsible for the SEM images seen in Section 4.1.3 and Section 4.3.1, respectively.
3. The GOA ray-tracing code used in this work was published by Bergstrom et al. [18] (available online at: http://www.mysimlabs.com/). Certain modifications to the code were made, such as adding a loop to analyse incident light of different wavelengths and specific conditions to model the surface cavities as blackbodies.
4. Dr. Kaihsiang Lin is responsible for some of the initial spectral reflectivity measurements on the FTIR and for reviewing the results in Chapters 3 and 4.

5. Ms. Fatima Sulieman is responsible for reviewing some of the results in Chapters 3, 4, and 6.
6. An industrial partner is responsible for the SEM cross-section images of the sample shown in Figure 5-2.

Chapter 2 : Theoretical Background

Chapter 2 provides a theoretical background for mechanisms by which AHSS radiative properties may cause temperature excursions during intercritical annealing. This section introduces pyrometry, a non-contact temperature measurement procedure used to infer steel strip temperatures at various locations within the furnace. Different types of pyrometry commonly used in industry (single-, dual- and multi-wavelength) are outlined.

Second, the chapter outlines the design of a typical continuous annealing furnace and develops a heat transfer model to compute strip temperature evolution. The heat transfer model describes how radiative property variations can directly cause temperature excursions by influencing the rate of thermal absorption by the steel strip.

2.1 Introduction to Pyrometry

Pyrometry, also known as radiation thermometry, is a non-contact temperature measurement procedure used for various applications. The steel industry has adapted it for CGLs to measure steel strip temperatures. Non-contact methods are preferred to prevent damage to the steel strip due to the CGL's continuous nature. Pyrometers infer the temperature of a target surface by measuring radiant surface flux, which is converted into an electrical output signal and then used to infer surface temperature through an algorithm [19].

A pyrometer consists of photonic sensors, various filters, and associated electronics that measure radiant flux from a target surface and generate an output signal,

$$S_{\lambda} = \kappa_{\lambda}\left(\lambda_{\mathrm{d}}\right)\cdot Q_{\mathrm{e}} \tag{2.1}$$

where Q_e is the radiant flux, κ_λ is the quantum efficiency of the photonic sensor, and λ_d is the detection wavelength. The radiant flux is [13],

$$\begin{aligned} Q_{\mathrm{e}} &= \int_{A_{\mathrm{d}}}\int_{\Delta\Omega_{\mathrm{d}}}\int_{\Delta\lambda_{\mathrm{d}}} L'_{\lambda}\left(T,\lambda_{\mathrm{d}},\theta_{\mathrm{p}}\right)\cdot\cos\left(\theta_{\mathrm{p}}\right)\cdot \mathrm{d}\lambda\cdot\mathrm{d}\Omega\cdot\mathrm{dA} \\ &= \int_{A_{\mathrm{d}}}\int_{\Delta\Omega_{\mathrm{d}}}\int_{\Delta\lambda_{\mathrm{d}}} \varepsilon'_{\lambda}\left(T,\lambda_{\mathrm{d}},\theta_{\mathrm{p}}\right)\cdot L'_{\lambda,\mathrm{b}}\left(T,\lambda_{\mathrm{d}},\theta_{\mathrm{p}}\right)\cdot\cos\left(\theta_{\mathrm{p}}\right)\cdot \mathrm{d}\lambda\cdot\mathrm{d}\Omega\cdot\mathrm{dA} \end{aligned} \tag{2.2}$$

where $L'_{\lambda,b}(T, \lambda_d, \theta_p)$ and $\varepsilon'_\lambda(T, \lambda_d, \theta_p)$ are the spectral intensity of a blackbody, and spectral directional emissivity of the target surface at target surface temperature, the detection wavelength λ_d, and viewing angle, respectively (the prime notation represents a directionally dependant property). The area of the photonic sensor is given by A_d, $\Delta\Omega_\mathrm{d}$ is the infinitesimal solid angle viewed by the photonic detector, $\Delta\lambda_\mathrm{d}$ is the infinitesimal spectral band of the pyrometer, and θ_p is the angle between the viewing axis of the pyrometer and the surface normal of the target.

Equations (2.1) and (2.2) can be combined for adequately small spectral bands, and if the viewing axis of the pyrometer is positioned normally to the steel surface ($\theta_\mathrm{p} = 0°$), the signal is [13] expressed as,

$$S_\lambda = \Delta\Omega_\mathrm{d} \cdot A_\mathrm{d} \cdot \kappa_\lambda\left(\lambda_\mathrm{d}\right) \cdot \varepsilon'_\lambda\left(T, \lambda_\mathrm{d}\right) \cdot L'_{\lambda,\mathrm{b}}\left(T, \lambda_\mathrm{d}\right) \cdot \Delta\lambda_\mathrm{d} \tag{2.3}$$

where Planck's distribution [13, 16] gives the blackbody intensity,

$$L'_{\lambda,\mathrm{b}}\left(T, \lambda_\mathrm{d}\right) = \frac{C_1}{\lambda_\mathrm{d}^{5}\left[\exp\left(\dfrac{C_2}{\lambda_\mathrm{d} T}\right)\right]}\left[\mathrm{Wm^{-2}\mu m^{-1}sr^{-1}}\right] \tag{2.4}$$

In Equation (2.4), $C_1 = 2 \cdot h \cdot c^2 = 1.191 \times 10^8$ $\mathrm{W \cdot \mu m^4 \cdot m^{-2} \cdot sr^{-1}}$, and $C_2 = h \cdot c / k_\mathrm{B} = 1.439 \times 10^4$ $\mathrm{\mu m \cdot K}$ where h is Planck's constant (6.626×10^{-34} J·s), c is the speed of light in a vacuum (2.998×10^8 m/s), and k_B is the Boltzmann constant (1.381×10^{-23} J/K). The terms $\Delta\Omega_\mathrm{d}$, A_d, κ_λ and $\Delta\lambda_\mathrm{d}$ are grouped to form a calibration constant, C_λ; therefore,

$$S_\lambda = C_\lambda \cdot \varepsilon'_\lambda\left(T, \lambda_\mathrm{d}\right) \cdot \frac{C_1}{\lambda_\mathrm{d}^{5} \cdot \left[\exp\left(\dfrac{C_2}{\lambda T_\mathrm{steel}}\right)\right]} \tag{2.5}$$

is the signal produced by the photonic sensor. Figure 2-1 illustrates a pyrometer performing surface temperature measurements of a steel strip.

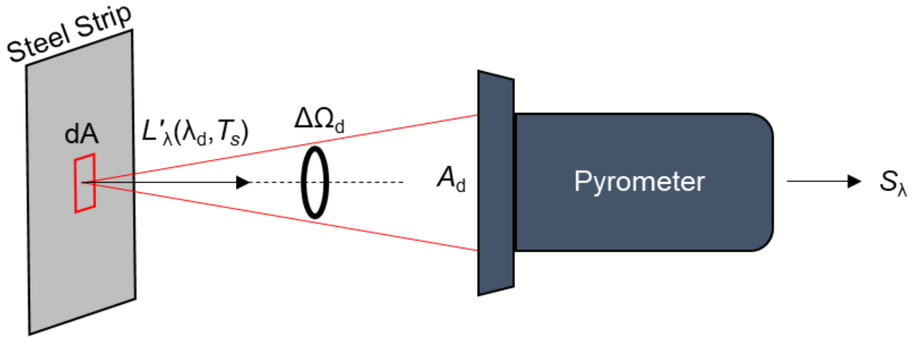

Figure 2-1: Schematic of a pyrometer measuring the surface temperature of a steel strip, showing the infinitesimal area, d*A*, the spectral intensity from the steel strip at the detection wavelength, $L'_{\lambda}(T, \lambda_{\mathrm{d}})$, the solid angle of measurement, $\Delta\Omega_{\mathrm{d}}$, the detector area, A_{d}, and the signal generated by the pyrometer, S_{λ}.

2.1.1 Single-Wavelength Pyrometry

Single-wavelength pyrometry relies on spectral irradiance measurements at a single detection wavelength, λ_{d}. The temperature inference,

$$T_{\mathrm{sw}} = \frac{C_2}{\lambda_{\mathrm{d}} \cdot \ln\left[\dfrac{\varepsilon'_{\lambda}\left(T, \lambda_{\mathrm{d}}\right) \cdot C_1 \cdot C_{\lambda}}{S_{\lambda} \cdot \lambda_{\mathrm{d}}^{5}}\right]} \tag{2.6}$$

is performed by rearranging Eq. (2.5). This method requires accurate knowledge of the spectral emissivity of the target surface at the detection wavelength, $\varepsilon'_{\lambda,\,\mathrm{d}}(T, \lambda_{\mathrm{d}})$. Tanaka and DeWitt [20] suggest that this method is only suitable for stable materials with known spectral emissivities that do not significantly vary during measurement. This assumption is usually untrue during annealing as the surface state and temperature of the steel strip evolve continuously. The user provides the pyrometer with an expected emissivity value and deviations of the actual strip emissivity can lead to temperature errors.

The emissivity of steel is highly sensitive to its temperature and surface state. Steel manufacturers often use single wavelength pyrometry in a wedge-shaped configuration [21, 22, 23] as shown in Figure 2-2. This configuration allows for exploiting a virtual blackbody created within the wedge with an emissivity of approximately unity. However, a significant drawback of the wedge-shaped design is its sensitivity to misalignment, which can lead to erroneous temperature measurements due to a reduction in the target's emissivity if the pyrometer is aimed imprecisely. Additionally, it may not be feasible to install pyrometers in a wedge configuration at all locations along a CGL.

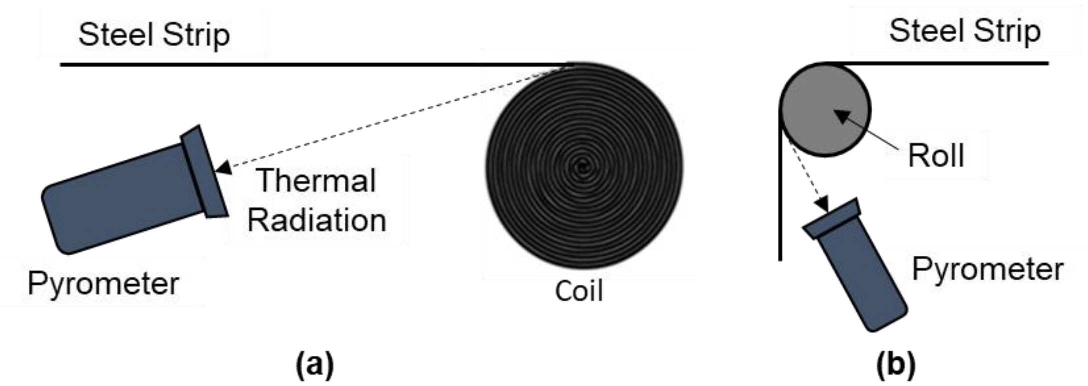

Figure 2-2: Two configurations for a wedge-type pyrometer arrangement. (a) Here the wedge is created between the steel strip and the coil as the coil is unwound (image adapted from Ref. [21]). (b) Here, the wedge is created between the roller and the steel strip. The wedges, in both cases, make a virtual blackbody where the emissivity is approximately unity.

2.1.2 Dual–Wavelength Pyrometry

Dual-wavelength pyrometry can ameliorate some of the issues associated with single-wavelength pyrometry by using spectral irradiance measurements at two detection wavelengths, λ_{d1} and λ_{d2}. The dual-wavelength temperature inference,

$$T_{\mathrm{dw}} = \frac{C_2 \cdot \left(\frac{1}{\lambda_2} - \frac{1}{\lambda_1} \right)}{\ln\left[\frac{\varepsilon'_{\lambda 2}}{\varepsilon'_{\lambda 1}} \cdot \frac{L'_{\lambda 1}}{L'_{\lambda 2}} \cdot \left(\frac{\lambda_1}{\lambda_2} \right)^5 \right]} \tag{2.7}$$

is again derived using Eq. (2.5). Dual-wavelength pyrometry does not require prior knowledge of spectral directional emissivity at each detection wavelength but the relationship between the spectral directional emissivities at the two detection wavelengths must be known [20, 24]. The emissivity ratio is often interpolated from a dataset as a function of the “brightness emissivity.” The brightness emissivity is obtained by comparing the irradiance at one channel with a blackbody intensity computed at a brightness temperature through a grey-body assumption. Therefore, variations in the actual emissivity ratios can produce pyrometric temperature errors.

One may express the error in the pyrometric temperature measurement as,

$$\frac{1}{T_\mathrm{M}}-\frac{1}{T_\mathrm{T}}=\frac{\ln\left(\dfrac{\varepsilon_\mathrm{r,P}}{\varepsilon_\mathrm{r,T}}\right)}{C_2\cdot\left(\dfrac{1}{\lambda_2}-\dfrac{1}{\lambda_1}\right)} \tag{2.8}$$

where T_M is the measured temperature, T_T is the true temperature, $\varepsilon_\mathrm{r,P,}$ is the steel strip's expected emissivity ratio, provided to the pyrometer, and $\varepsilon_\mathrm{r,T}$ is the true emissivity ratio. According to Eq. (2.8), selecting wavelengths further apart minimises the temperature error [25].

Dual-wavelength pyrometry is common in the industry, and Thiessen et al. [26] observed variations between dual-wavelength pyrometric and thermocouple temperature measurements while annealing various transformation-induced plasticity (TRIP) steel samples in a reducing atmosphere (90%Ar and 5% H_2). They attributed these differences to emissivity ratio changes caused by the formation of surface oxides during annealing. Additionally, Somveille et al. [27] also discussed how the oxidation of DP-780 and DP-980 alloys during annealing might influence their emissivity and hence pyrometric temperature measurements.

2.1.3 Multi-Wavelength Pyrometry

Multi-wavelength pyrometry utilises spectral irradiance measurements at three or more detection wavelengths with an emissivity compensation algorithm to infer the temperature of the target surface. This method models the emissivity of the surface as a polynomial function with respect to wavelength [28],

$$\varepsilon_{\lambda_\mathrm{d}}\left(\lambda_\mathrm{d}\right)=a_0+a_1\,\lambda_1+.....+a_\mathrm{m-1}\,\lambda_\mathrm{i}^\mathrm{m-1} \tag{2.9}$$

and infers the polynomial coefficients and the surface temperature together. Multi–wavelength pyrometry results in *n* equations (one for each wavelength) and *m* + 1 unknowns (coefficients of the polynomial and the surface temperature). The algorithm explicitly solves for the polynomial coefficients and the surface temperature or infers them using a least-squares minimisation technique [29]. For the exact method, the number of detection wavelengths *n* must be one more than the number of polynomial coefficients *m*.

The exact method, however, is more susceptible to errors caused by over-fitting when using more than three detection wavelengths due to noise in the data [30]. To overcome this issue, Wen [29] suggests using the least-squares minimisation approach, where the number of detection wavelengths, *n,* must be at least two greater than the number of emissivity coefficients *m.* The least-squares process attempts to find the set of emissivity coefficients and surface temperature such that the sum of squares error,

$$R^2 = \sum_{i=0}^{n} \left(L_{\lambda,\mathrm{meas},i} - L_{\lambda,\mathrm{gen},i} \right)^2 \tag{2.10}$$

is minimised. In Eq. (2.10), $L_{\lambda,\text{ meas},i}$ is the measured spectral intensity and $L_{\lambda,\text{ gen},i}$ is the generated spectral intensity at a given set of emissivity parameters and surface temperature.

Given the reliance of all three pyrometric techniques on accurate spectral emissivity models, it becomes necessary to understand how spectral emissivity may vary with the surface state, the temperature of the steel, and across a single AHSS coil. Variations in spectral emissivities across a single AHSS coil may lead to different pyrometric temperature errors at different coil locations as it passes through the annealing furnace.

2.1.4 Pyrometric Wavelength Selection

Various considerations go into selecting appropriate wavelengths for pyrometry, such as how the atmosphere interacts with the radiation, the stability of the target surface emissivity at a particular wavelength, and nearby radiation sources [31]. For dual-wavelength pyrometry, the separation between the two wavelengths is also crucial as it influences the stability of the inferred temperature [25]. The temperature errors are the greatest when the wavelengths used are closer together, as predicted by Eq. (2.8), and as shown in the experimental results in Figure 3-7.

For annealing steels on CGLs, the reducing atmosphere of 95% N_2 and 5% H_2 is transparent and does not play a significant role in wavelength selection. Shorter wavelengths in the NIR region (0.8 – 2.5 μm) of the EM spectrum are usually selected for steels, as they have larger spectral emissivity values in this region [31]. As such, Williamson® (a key provider of pyrometers to North American galvanisers) commonly uses wavelengths of 1.6, 2.1 and 2.4 μm [32]. Therefore, all pyrometric analyses in this thesis will focus on these three wavelengths.

2.2 Annealing Furnace Basics

2.2.1 Annealing Furnace Design

The design of annealing furnaces is proprietary to the steel manufacturer but generally consist of direct and indirect fired heating zones [33]. First, the steel strip enters a pre-heater, where exhausted flue gasses provide initial heating; the strip then passes through a direct-fired heating zone, where open-flame natural gas burners further heat the strip. The furnace also consists of an airlock which allows producers to maintain an internal reducing atmosphere (95%N_2 and 5%H_2 by vol.) to minimise oxidation. Lastly, the strip passes through an indirectly fired heating zone, where radiant tubes supply heat, within lean combustion of natural gas occurs, as shown in Figure 2-3.

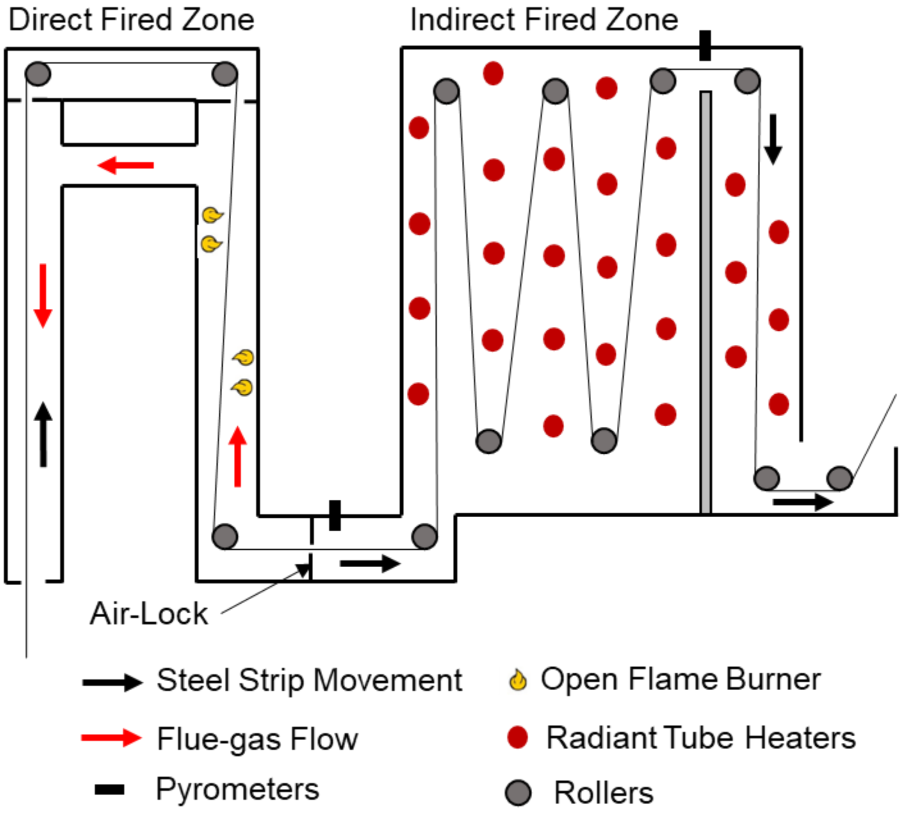

Figure 2-3: A schematic of the annealing furnace installed at Voestalpine Stahl GmbH in Linz, Austria. Image adapted from Ref. [33]

2.2.2 Furnace Heat Transfer Model

One can make several assumptions to model strip temperature evolution: (1) radiation is the dominant form of heat transfer due to the high temperatures involved [15, 16]; (2) the furnace surroundings are large and isothermal; and (3) heat conduction within the steel coil is negligible.

Conduction within the coil can be considered negligible due to its thinness (~1.5mm) in contrast to its large lateral dimensions (~1739m × 2.5m). The heat diffusion equation,

$$\rho_{\mathrm{s}} \cdot c_{\mathrm{p,s}} \left(\frac{\partial T}{\partial \mathrm{t}} + v \cdot \frac{\partial T}{\partial x} \right) = k_{\mathrm{s}} \cdot \left(\frac{\partial^2 T}{\partial x^2} + \frac{\partial^2 T}{\partial y^2} + \frac{\partial^2 T}{\partial z^2} \right) \tag{2.11}$$

governs the temperature distribution within the steel coil, which in its non-dimensional form can be written as

$$\frac{\partial T}{\partial \tilde{t}} + \frac{\partial T}{\partial \tilde{x}} = \frac{k_{\mathrm{s}} \cdot l_{\mathrm{s}}}{v \cdot \rho_{\mathrm{s}} \cdot c_{\mathrm{p,s}}} \cdot \left(\frac{1}{l_{\mathrm{s}}^2} \cdot \frac{\partial^2 T}{\partial \tilde{x}^2} + \frac{1}{w_{\mathrm{s}}^2} \cdot \frac{\partial^2 T}{\partial \tilde{y}^2} + \frac{1}{t_{\mathrm{s}}^2} \cdot \frac{\partial^2 T}{\partial \tilde{z}^2} \right) \tag{2.12}$$

where ρ_{s} is the density of the steel, t_{s} is the sheet thickness, $c_{\mathrm{p,s}}$ is the specific heat capacity, k_{s} is the thermal conductivity of steel, l_s is the length of the sheet, and w_s is the width of the sheet. Assuming characteristic steel properties such as the thermal conductivity (50 $\mathrm{Wm^{-1}K^{-1}}$), density (7000 $\mathrm{kgm^{-3}}$), and average specific heat capacity (600 $\mathrm{Jkg^{-1}K^{-1}}$), one may write,

$$\frac{\partial T}{\partial \tilde{t}} + \frac{\partial T}{\partial \tilde{x}} = \frac{50 \cdot 1739}{2 \cdot 7000 \cdot 600} \cdot \left(\frac{1}{1739^2} \cdot \frac{\partial^2 T}{\partial \tilde{x}^2} + \frac{1}{2.25^2} \cdot \frac{\partial^2 T}{\partial \tilde{y}^2} + \frac{1}{\left(1.5 \cdot 10^{-3}\right)^2} \cdot \frac{\partial^2 T}{\partial \tilde{z}^2} \right) \tag{2.13}$$

$$\frac{\partial T}{\partial \tilde{t}} + \frac{\partial T}{\partial \tilde{x}} = 3.423 \times 10^{-9} \cdot \frac{\partial^2 T}{\partial \tilde{x}^2} + 2.04 \times 10^{-3} \cdot \frac{\partial^2 T}{\partial \tilde{y}^2} + 4600.53 \cdot \frac{\partial^2 T}{\partial \tilde{z}^2} \tag{2.14}$$

where the coefficients of the temperature gradients in the x and y directions are very small. As such, the conduction along the length and width of the coil is negligible. Therefore, variations in the local strip radiative properties dominate the local temperature evolution of a coil section.

Under these assumptions, an ordinary differential equation

$$\begin{aligned} &\dot{q}_{\text{rad,in}} - \dot{q}_{\text{rad,out}} = \rho_{\text{s}} \cdot t_{\text{s}}\, c_{\text{p,s}} \cdot \frac{\mathrm{d}T_{\text{steel,loc.}}}{\mathrm{dt}} \\ &=> \alpha\sigma T^{4}_{\text{furnace,loc.}}\left(x_{\text{f}}\right) - \varepsilon\sigma T^{4}_{\text{steel,loc.}}\left(x_{\text{f}}\right) = \rho \cdot t_{\text{s}} \cdot c_{\text{p,s}} \cdot \frac{\mathrm{d}T_{\text{steel,loc.}}}{\mathrm{dt}} \end{aligned} \tag{2.15}$$

accurately captures local strip temperature evolution. Here, $q_{\text{rad,in}}$ and $q_{\text{rad,out}}$ are the heat absorbed and emitted by the local area on the steel strip due to thermal radiation, $T_{\text{furnace, loc.}}$ and $T_{\text{steel, loc.}}$ are the local furnace surroundings and steel strip temperatures, σ is the Stefan-Boltzmann constant (5.67×10^{-8} $\text{Wm}^{-2}\mu\text{m}^{-4}$), α and ε are the local total hemispherical absorptivity and emissivity of the steel strip, x_{f} is the distance into the furnace, and $\mathrm{d}T_{\text{steel, loc.}}/\mathrm{dt}$ is the first derivative of the local steel temperature with respect to time. This work uses the explicit Euler scheme to solve Eq. (2.15). Figure 2-4 schematically represents the heat transfer model.

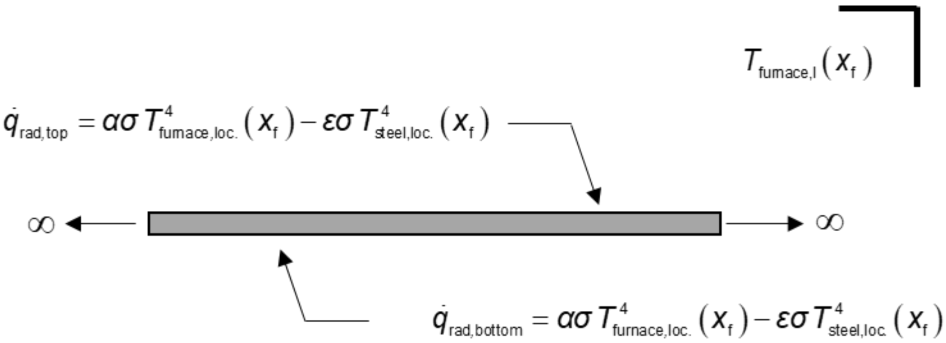

Figure 2-4: Heat-transfer model for predicting local strip temperature evolution through the furnace, where furnace surroundings are assumed to be large and isothermal.

Marginalising the spectral directional radiative properties over all wavelengths of interest and directions:

$$\varepsilon\left(T_{\text{steel}}\right)=\frac{\int_{\cap}\int_{\lambda=0}^{\infty}\left[\varepsilon'_{\lambda}\left(\theta_{\text{e}}\right)\cdot L'_{\lambda\text{b}}\left(T_{\text{steel}}\right)d\lambda\right]\cdot\cos\left(\theta_{\text{e}}\right)\text{d}\Omega_{\text{e}}}{\sigma T_{\text{steel}}^{4}} \tag{2.16}$$

and

$$\alpha\left(T_{\text{furnace}}\right)=\frac{\int_{\cap}\int_{\lambda=0}^{\infty}\left[\alpha'_{\lambda}\left(\theta_{\text{i}}\right)\cdot L'_{\lambda\text{b}}\left(T_{\text{furnace}}\right)d\lambda\right]\cdot\cos\left(\theta_{\text{i}}\right)\text{d}\Omega_{\text{i}}}{\sigma T_{\text{furnace}}^{4}} \tag{2.17}$$

yields the total hemispherical radiative properties, where $L'_{\lambda,\text{ b}}$ is the blackbody spectral intensity. Note here that, through Kirchhoff's law [16]

$$\varepsilon'_{\lambda}\left(\theta_{\text{e}}\right)=\alpha'_{\lambda}\left(\theta_{\text{i}}\right)=1-\rho'_{\lambda,\text{d}-\text{h}}\left(\theta_{\text{i}}\right). \tag{2.18}$$

The radiative properties do not vary with the azimuthal angle, φ, which is usually valid for isotropic random Gaussian surfaces (see Chapter 4).

This model shows that the radiative properties of the steel strip strongly influence the local strip temperature evolution through the annealing furnace; therefore, variations in radiative properties across a single AHSS coil can lead to different parts of the coil evolving in temperature differently, in turn producing different post-annealed mechanical properties. The thesis investigates later the effect of these radiative property variations on temperature excursions.

Chapter 3 : Radiative Property Characterisation

As discussed, no study has analysed radiative property variations across single AHSS coils in their pre-annealed condition before they enter the annealing furnace. This chapter highlights the significant variations in radiative properties across a single AHSS (DP780) coil that is hot-rolled, acid-pickled and cold-rolled on an industrial line, showing that upstream processes (of annealing) can also have a significant effect on strip radiative properties. Furthermore, as discussed in the previous chapter, these varying radiative properties can subsequently induce temperature excursions during the annealing process.

3.1: Sample Extraction and Analysis Performed

This research extracts square samples (35mm × 35mm) from a DP780 coil processed on an industrial continuous galvanising line. These samples are from 18 different coil locations at nine different axial lengths along the coil, from the edge ("Edge samples" or "E") and the middle ("Mid samples" or "M"), as shown in Figure 3-1. This work analyses five samples from each location (a total of 90 samples), and the results presented in this thesis are the averaged values. Additionally, at specific locations (450m Edge, 1684m Mid and 880m Mid), eight more samples are analysed (13 total); the standard error in emissivity values across these samples is computed. The similarity of the spectral emissivity spectra (see Appendix A) across these 13 replicates shows that the results from one sample are representative of the population of samples from one coil location.

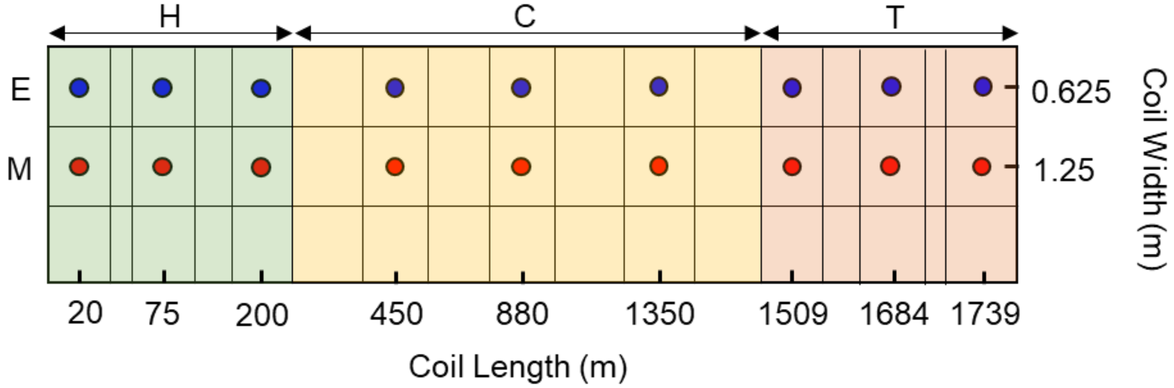

Figure 3-1: Locations of extracted samples on the DP-780 coil, samples from the edge (E) and middle (M) of the coil are labelled with blue and red dots, respectively. The head, centre, and tail sections are marked as H, C, and T. [not to scale]

The radiative properties of the extracted samples are analysed using a Fourier Transform Infra-Red (FTIR) spectrometer between wavelengths of 0.5 and 20 µm. Section 3.2 provides a detailed explanation of the procedure followed and the workings of an integrating sphere. Section 3.3 then discusses the results.

3.2 Ex-Situ Spectral Reflectivity Analysis

This study uses a Bruker® Invenio – X FTIR spectrometer with an integrating sphere to perform *ex-situ* spectral reflectivity measurements. An integrating sphere is a device used to collect light reflected by the sample into all directions of the hemisphere, which is necessary to evaluate the sample's spectral, directional-hemispherical reflectivity. The intensity of the collected light is then measured, allowing the FTIR to infer the spectral, directional-hemispherical reflectivity. The inside of the sphere is coated with a highly reflective, Lambertian material (i.e., the intensity of reflected light is equal in all directions) [34]. This procedure uses integrating spheres coated with Spectralon® (0.5 – 1.1 µm) and Infragold® materials (1.1 – 20 µm) for the two wavelength ranges. Figure 3-2 shows the spectral reflectivity of Spectralon® and Infragold®; the spectral reflectances of both materials are ≥ 90% in their respective operating domains [35].

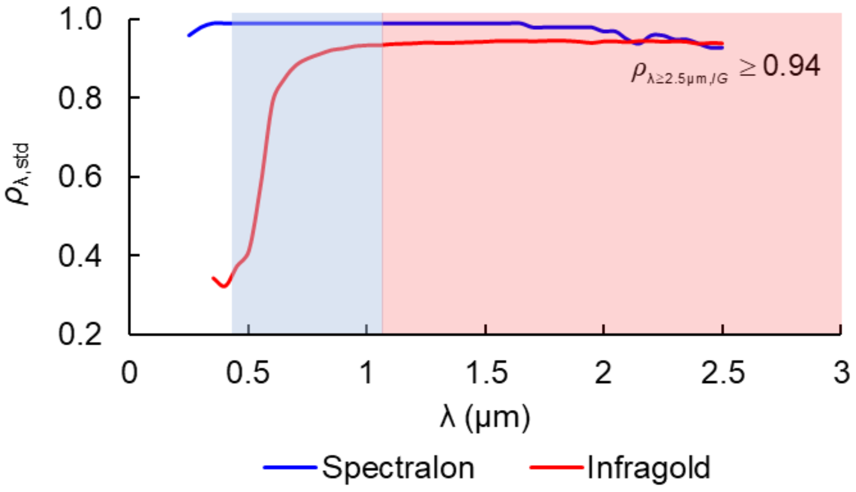

Figure 3-2: Spectral reflectivity of Infragold® and Spectralon® (coatings used in the two integrating spheres). In their respective operating ranges, the spectral reflectivities of both materials are larger than 0.9. The shaded areas show the operating ranges of the integrating spheres [36].

Figure 3-3 shows the schematic of an integrating sphere. The light from the FTIR enters the sphere through the entrance port, and the flip mirror focuses the light onto the sample port, the reference spot or the specular exclusion port. The user may place the sample in the sample port or the specular exclusion port and use the mirror to shine the incident light onto the sample. This study uses the specular exclusion port to hold the sample.

The sphere collects the reflected light, which represents the fraction of incident radiation reflected by the sample into all directions of a hemisphere; the detector then measures the intensity of the collected light. Baffles inside the sphere (not shown in the diagram) prevent specularly-reflected light from entering the detector port directly. By measuring the intensity of collected light, this integrating sphere provides near-normal spectral, directional-hemispherical reflectivity spectra of the sample at an incident angle of 14.8°.

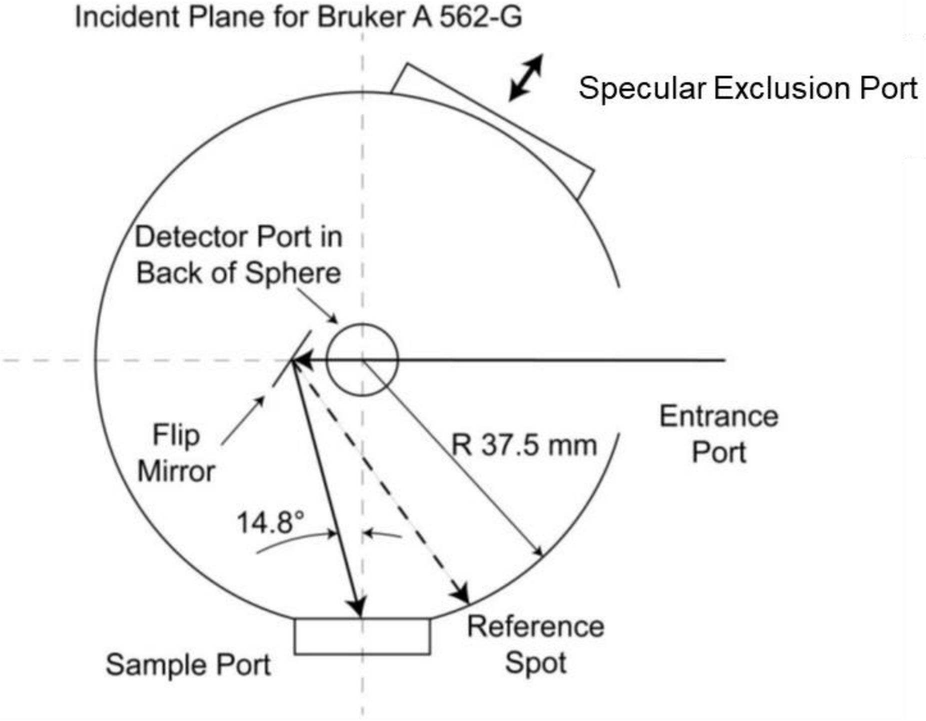

Figure 3-3: Schematic of a Bruker A-562 Integrating Sphere [35]

However, the integrating sphere is not a perfect reflector, which may lead to errors in the spectral reflectivity measurements [35]. Therefore, a user must make a reference measurement at the reference spot shown in Figure 3-3 to account for the imperfect nature of the integrating sphere. This work follows the procedure discussed by Blake et al. [35] to infer the reflectivities of the steel samples through the following steps:

1. A Spectralon® or an Infragold® standard (depending on the wavelength range and the integrating sphere) is placed in the specular exclusion port – a measurement is performed with the beam focused onto the specular exclusion port generating the spectrum, $V_{\text{std, s}}$.
2. Next, the standard is replaced with the sample in question, and a measurement is performed, yielding the spectrum, $V_{\text{sample, s}}$.
3. Thirdly, the beam is switched to the reference spot, and the Spectralon® or the Infragold® standard is placed in the specular exclusion port and a measurement is made, $V_{\text{std, ref}}$.
4. Lastly, while maintaining the beam at the reference spot, the standard is switched with the sample and a final measurement is made, $V_{\text{sample, ref}}$.

The spectral, directional-hemispherical reflectance of the sample is then computed through,

$$\rho_{\lambda,\text{d-h}} = \frac{V_{\text{sample,s}} \big/ V_{\text{standard,s}}}{V_{\text{sample,ref}} \big/ V_{\text{standard,ref}}} \cdot \rho_{\text{std}} \tag{3.1}$$

where ρ_{std} is the reflectance spectra of the standard (Infragold® or Spectralon®) [36]. Kirchoff's law then converts (Eq. (2.18)) the spectral, directional-hemispherical reflectivities to spectral directional emissivities.

3.3 Radiative Property Results for Samples from Different Coil Locations

3.3.1 Spectral Emissivity Variations

Figure 3-4 shows spectral directional emissivity spectra for select samples generated using the procedure described in Sec. 3.2. Pyrometers operate in the NIR region (orange shaded area) of the EM spectrum, as discussed earlier in Section 2.1.4. The Williamson PRO MWX-ST-17 industrial pyrometer, commonly used by North American galvanisers, uses 1.6, 2.1 and 2.4 μm [32]. Therefore, these wavelengths are of particular concern for the continuous galvanising of AHSS.

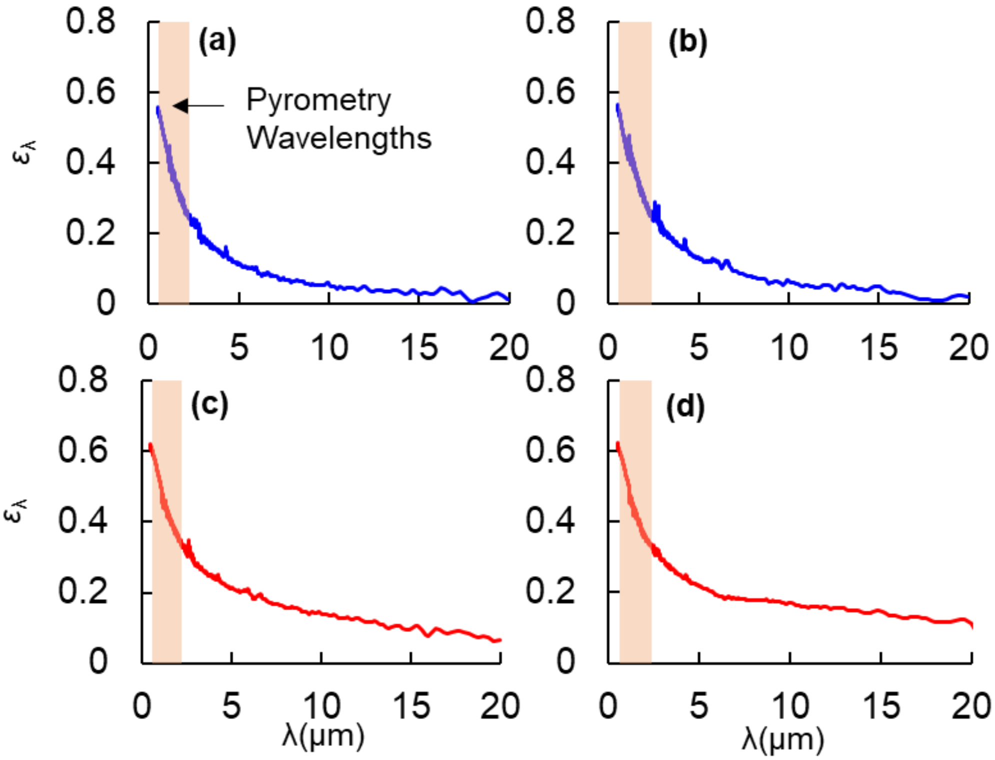

Figure 3-4: Difference in spectral emissivity values between the Edge and Middle of the coil; the Edge samples show lower spectral emissivity values than the Mid samples. The amber-shaded area represents the NIR region important for pyrometry. Samples are from the (a) 20m Edge, (b) 75m Edge, (c) 1509m Mid, and (d) 450m Mid coil locations.

The refractive index *n* and extinction coefficient *k*, dependent on the material and the wavelength of the incident light, fully define the radiative properties of a perfectly smooth conducting material [16]. The Fresnel equation,

$$\rho_{\lambda,n} = \frac{\left[n(\lambda)-1\right]^2 + \left[k(\lambda)\right]^2}{\left[n(\lambda)+1\right]^2 + \left[k(\lambda)\right]^2} \tag{3.2}$$

defines the spectral, normal reflectivity of a smooth surface.

The optical constants for specific AHSS alloys are not readily available; however, Lin et al. [37] measured the spectral reflectivity of several mirror-polished DP980 AHSS alloys and found that they have optical properties corresponding to that of highly polished pure iron. Figure 3-5 shows the optical properties of pure iron and the corresponding normal spectral emissivity computed using Eq. (3.2) and Eq. (2.18). This thesis uses optical constants for iron from Ordal et al. [38] and Johnson et al. [39]. Variations between the theoretical spectral emissivity shown in Figure 3-5 and the measured spectral emissivities of the samples in Figure 3-4 can be attributed to surface roughness differences and surface cavities on the steel substrate, as will be discussed further in Chapter 4.

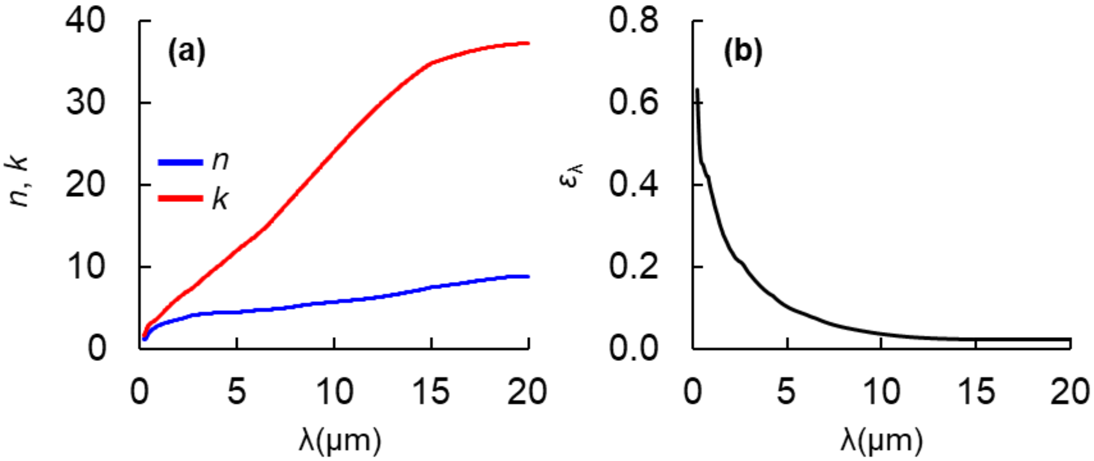

Figure 3-5: (a) Refractive index, *n* and extinction coefficient, *k* of pure Iron, and (b) the corresponding theoretical normal spectral emissivity. The optical properties are from Ordal et al. [38] and Johnson et al. [39]

The surface's reflectivity may also vary depending on the polar angle of incidence or reflectance; the roughness of the surface primarily drives this directional dependence. A rougher surface will reflect light more diffusively (i.e., equally in all directions of a hemisphere) for a given angle of incidence. On the other hand, the reflectance from a smoother surface would be more specular [16]. Usually, for surfaces with random Gaussian height profiles (usually the case with cold rolling), the azimuthal angle, φ, will have a negligible effect on the radiative properties. This assumption was validated by Lin et al. [37] through the GOA ray-tracing approach. The FTIR measurements are performed at a polar incidence of 14.8°, yielding a near-normal spectral reflectance measurement.

Figure 3-6 shows spectral directional emissivities at the three common pyrometric wavelengths of 1.6, 2.1 and 2.4 µm from all 18 coil locations (averaged across the five replicates). There are significant variations in spectral directional emissivities across the coil. Variations along the length of the coil are more pronounced at the head and tail sections, and the spectral directional emissivities of the Mid samples are systematically higher at all coil lengths compared to the edge samples. Such variations in spectral directional emissivities can lead to pyrometric temperature errors when using single-wavelength pyrometry. At select coil locations, 13 (see Appendix A) samples are analysed to compute a standard error. The error bars at these data points, shown in Figure 3-6, reflect this standard error together with the 3% random error of the FTIR apparatus.

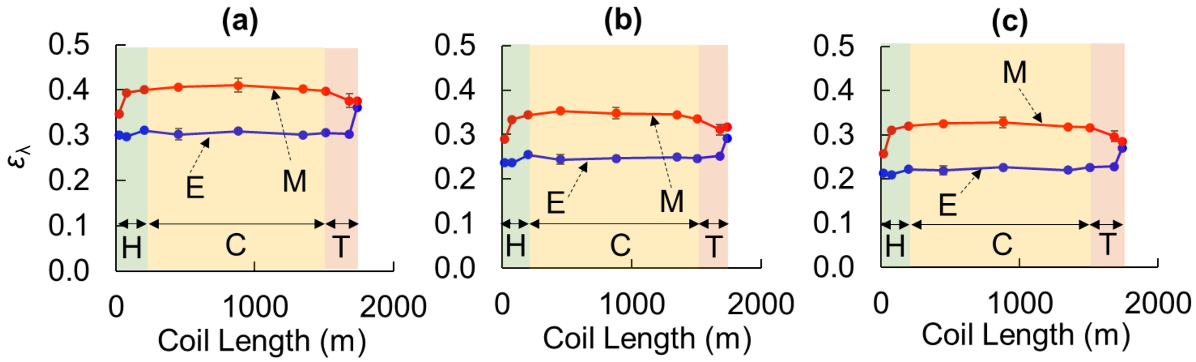

Figure 3-6: Spectral directional emissivities at all 18 coil locations at the three common pyrometric wavelengths of (a) 1.6 µm, (b) 2.1 µm and (c) 2.4 µm. The coil's head, centre and tail sections have been shaded in green, yellow, and orange, respectively.

3.3.2 Emissivity Ratio Variations and Pyrometric Temperature Errors

Figure 3-7 shows significant variations in emissivity ratios at: 1.6 µm/2.1 µm, 1.6 µm/2.4 µm, and 2.1 µm/2.4 µm. As discussed in Sec. 2.1.2, variations in emissivity ratios can lead to dual-wavelength pyrometric temperature errors. The emissivity ratios of the Edge samples are higher than that of the Mid samples, and the emissivity ratios for the 2.1 µm/2.4 µm case are smaller as those wavelengths are closer together. Figure 3-7 also shows the associated expected dual-wavelength pyrometric temperature errors, which are inferred through Eq. (2.8) and by assuming the average emissivity ratio across all samples to be the expected emissivity ratio, $\varepsilon_{r,P}$.

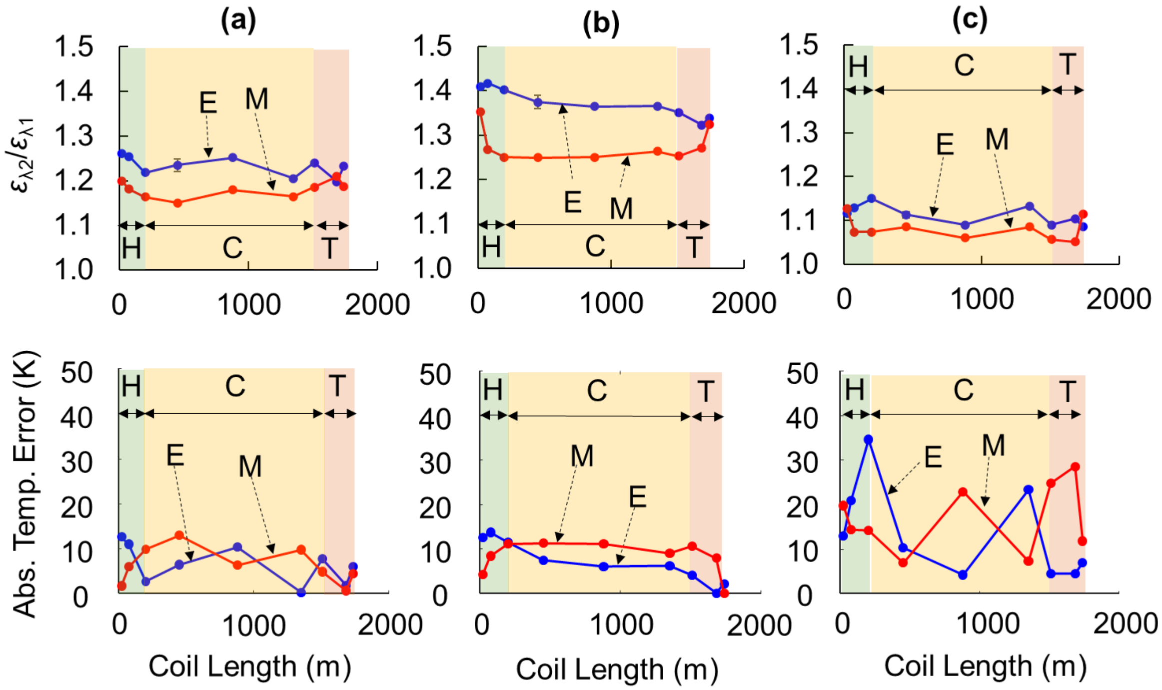

Figure 3-7: Variations in emissivity ratios and the associated temperature errors at common pyrometry wavelengths. Samples extracted from the edge (E) of the coil show larger emissivity ratio values than samples from the middle (M). The head, centre and tail sections are marked with H, C and T, respectively. (a) 1.6/2.1 µm, (b) 1.6/2.4 µm, (c) 2.1/2.4 µm

These emissivity ratio variations cause temperature errors ranging between 0 K and 35 K along the coil's length and width, as predicted by Eq. (2.8). The temperature errors are the greatest when the detection wavelengths are closer together. Temperature swings of this magnitude during the annealing process can lead to erratic changes in the steel microstructure and hence its mechanical properties post-annealing. For instance, Mosser et al. [40] found significant variations in the stress-strain (UTS variations of ~200MPa) behaviours of DP980 samples with intercritical annealing temperature variations of approximately ±25K, as shown in Figure 3-8. Ma et al. [41] also found variations in the stress-strain behaviours of medium-Mn steels for intercritical annealing temperature variations as low as ±5K.

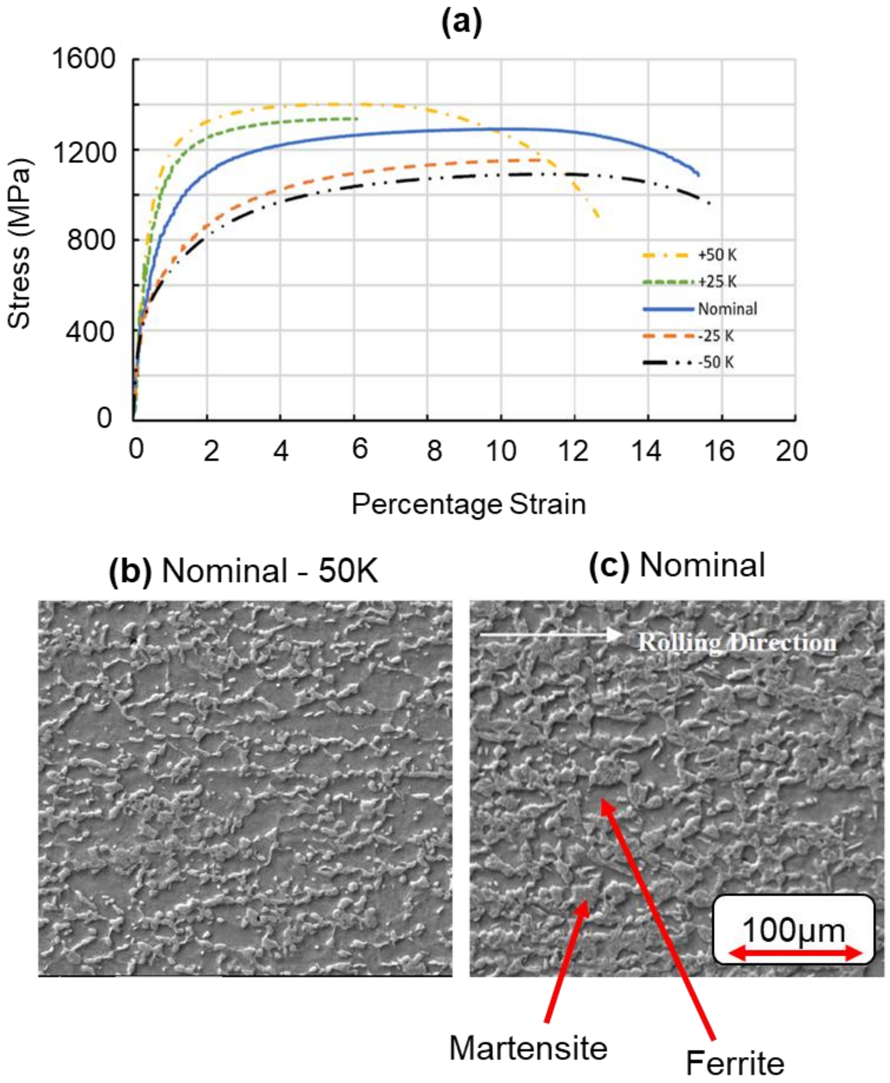

Figure 3-8: (a) Effect of intercritical annealing temperature on the stress-strain behaviour and microstructure of DP980 steels [40]. Different intercritical annealing temperatures cause significant variations in the steels' ultimate tensile strengths (UTS) and yield strengths (YS) due to a difference in the volume fraction of Martensite (α') and Ferrite (α) as shown in the micro-structures ((b) and (c)).

It is important to note that the radiative properties of the steel strip will also vary during the annealing process due to temperature changes (which may influence the optical constants *n* and *k* of the steel [16]) and surface states of the steel, such as roughness and oxidation effects [32, 42, 43].

Smooth and rough AHSS surfaces show the formation of oxide layers and nodules, which influence spectral emissivity through interference and roughness effects, respectively [42]. These further variations may lead to more significant differences in emissivity ratios and temperature errors across the coil. However, emissivity variations during the annealing process are highly unpredictable; therefore, analytically characterising them is a significant challenge and has not been performed in this thesis.

Instead, future work should focus on implementing an empirical approach by processing samples from the different coil locations in an annealing simulator to study how radiative properties and surface states evolve during annealing at different heating rates and atmospheric dew points [32, 42].

3.3.3 Total Hemispherical Absorptivity Variations & Strip Temperature Evolution

This section uses Eq. (2.16) and Eq. (2.17) to compute the total hemispherical emissivities and absorptivities, respectively. The spectral directional emissivities obtained through the experimental analysis are near-normal values and do not contain information regarding their directional dependence, making it challenging to marginalise over all directions of interest. Therefore, the spectral directional emissivities are multiplied by a conversion factor for metallic surfaces, accounting for the typical angular distribution of the spectral directional emissivity [44], to obtain spectral hemispherical emissivities.

Typically, metals have larger spectral directional emissivities at higher incident angles; these correction factors account for this directional dependence. Deviations from this typical behaviour due to surface roughness are possible; however, it is challenging to quantify experimentally with the available apparatus. Samples with high surface roughnesses will reflect light more diffusively. As such, this is an analogue method of making this correction. Figure 3-9 shows these conversion factors.

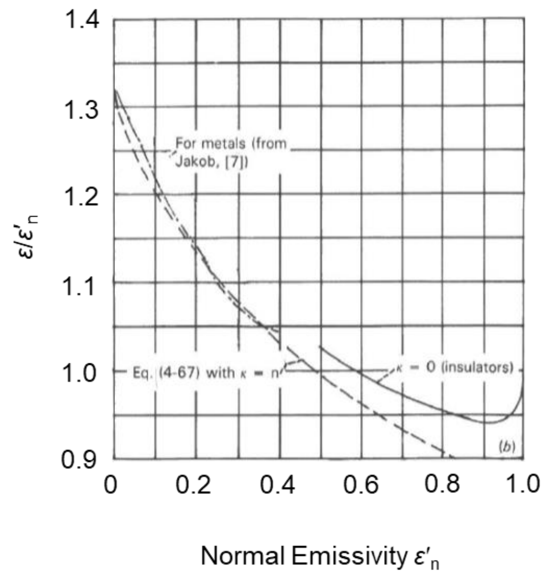

Figure 3-9: Conversion factors for converting normal emissivities to hemispherical emissivities. Adapted from Ref. [44].

This work mathematically models the spectral hemispherical emissivities using a power-law function to compute approximate total hemispherical emissivities and absorptivities by integrating over all wavelengths of interest (0.5 - 20 µm). Figure 3-10 shows the spectral hemispherical emissivities for one of the samples overlayed with the blackbody spectral intensity distribution, assuming a characteristic furnace temperature of 850°C.

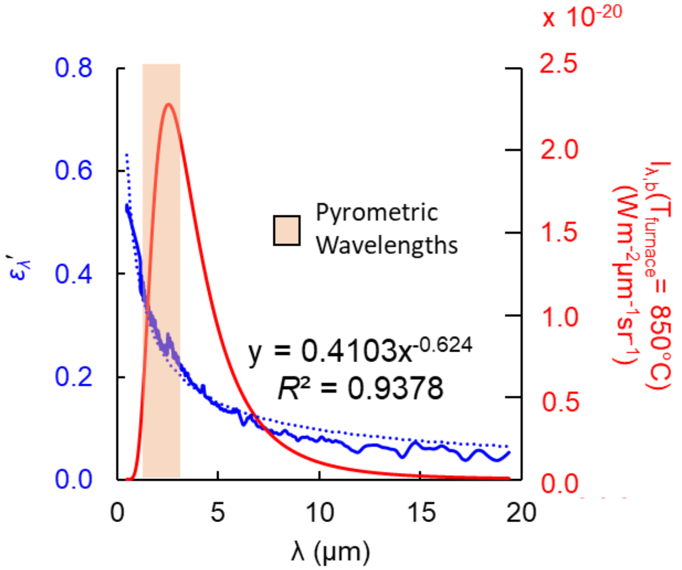

Figure 3-10: Spectral hemispherical emissivity curve for one of the samples, which have been curve-fit using a power law function, overlaid with the blackbody spectral intensity (given by Planck's distribution).

Figure 3-11 shows the variations in total hemispherical absorptivities across the coil through this analysis. Chapter 4 then analyses the surface topographies of the samples highlighted by the black circles through optical profilometry, microscopy and scanning electron microscopy (SEM).

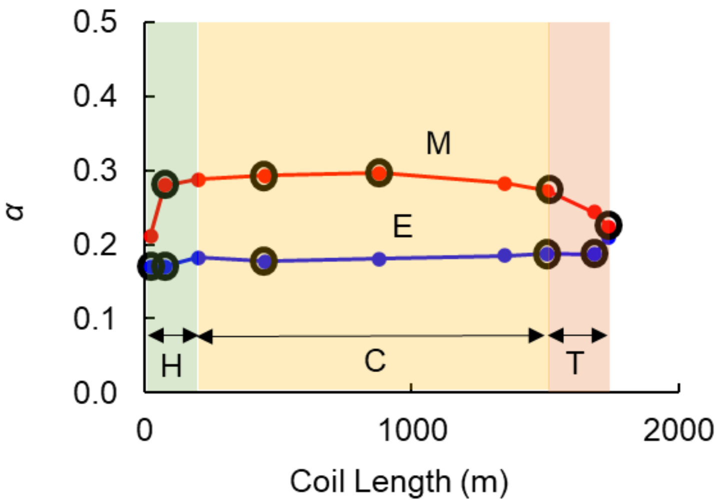

Figure 3-11: Total hemispherical absorptivity variations (at T_{furnace} = 850°C) along the length and width of the coil. Samples from the head, centre and tail sections are shaded in green, yellow, and orange, respectively.

As expected, the total hemispherical absorptivities of the Mid samples are systematically larger than those of the Edge samples with variations along the length of the coil more pronounced at the head and tail sections. The total hemispherical absorptivity results presented in Figure 3-11 are at a representative furnace temperature of T_{furnace} = 850°C; however, while solving Eq. (2.15) using the explicit Euler scheme, the total hemispherical absorptivities and emissivities are computed at each time step as the local temperature of the steel strip and the furnace section change, using Eq. (2.16) and Eq. (2.17).

This section explores two different furnace temperature profiles from Somveille et al. [27], representing the temperature profiles used for annealing the respective DP grades (see Figure 3-12). This analysis assumes a characteristic coil speed of approximately 2 m/s (through discussions with industrial partners). It models the temperature evolutions of two samples showing the largest difference in total hemispherical absorptivity (450m Edge & 450m Mid) according to the heat transfer model in Sec. 2.2.2. Figure 3-14 shows the computed temperature evolutions. Specific heat capacity values for the steel are from Ref. [45], and the heat transfer model uses a characteristic steel density of ~7000 kgm^{-3} (variations in density w.r.t. temperature is smaller than specific heat). Figure 3-13 shows these specific heat values.

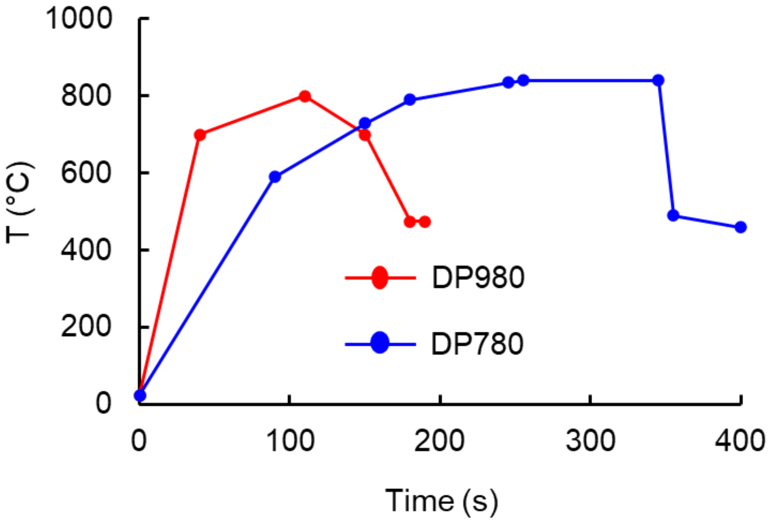

Figure 3-12: Representative furnace temperature profiles for DP780 (blue) and DP980 (red) alloys, taken from Somveille et al. [27]. These furnace temperature profiles have been used to model strip temperature evolutions in this study.

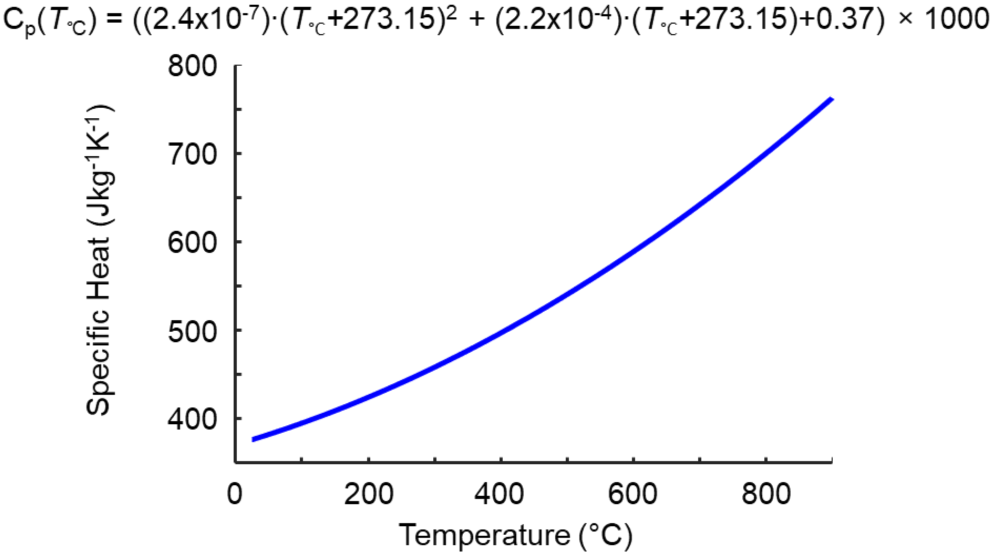

Figure 3-13: Specific heat for DP-980 as a function of temperature, where the relationship follows a quadratic behaviour [45]. These values have been applied for both the DP780 and DP980 heating schedules, as it is challenging to obtain these relationships for all DP grades.

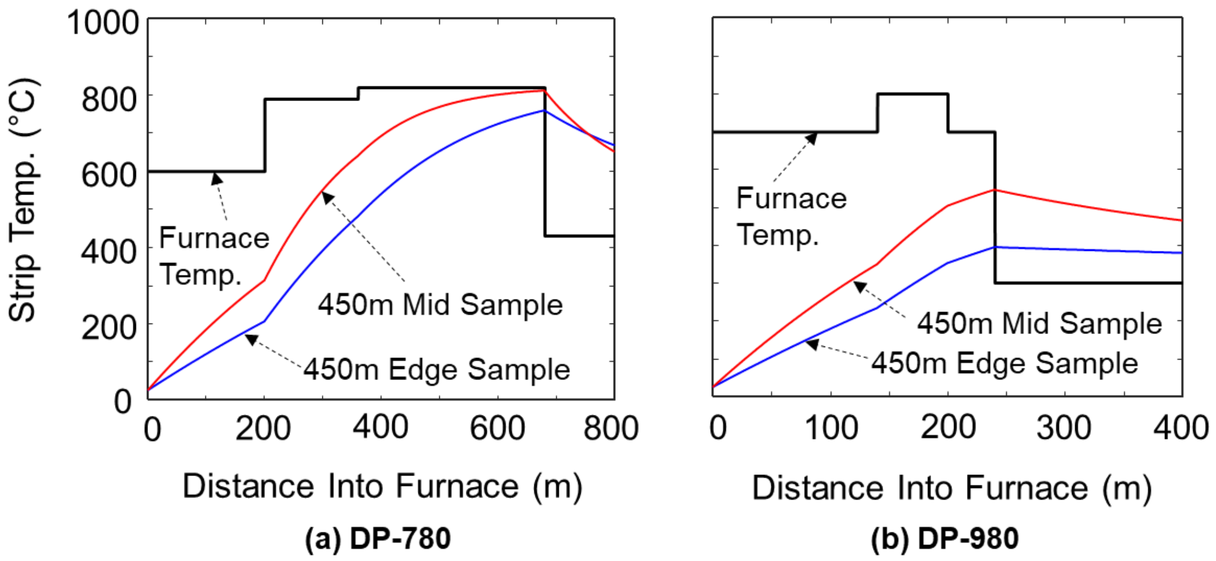

Figure 3-14: Expected temperature evolutions of two samples showing large differences in total hemispherical absorptivities. Furnace temperature profiles for typical (a) DP780 and (b) DP980 alloys.

In practice, these heating profiles are designed based on the AHSS grade (e.g., DP780, DP980, etc.) and the specific alloy composition of the steel, which may vary considerably among producers. Therefore, these curves are representative and cannot be applied globally. Nevertheless, according to the strip temperature evolutions computed in Figure 3-14, the heating schedule strongly influences the effect of total hemispherical absorptivity on strip temperature evolution.

In the case of Profile (b), two locations on the same coil having different total hemispherical absorptivities (Figure 3-14)) exhibit a temperature difference of approximately 150K after heating; such temperature variations can lead to drastic changes in the mechanical properties of the steel as shown by the stress-strain curves in Figure 3-8. Conversely, for a coil heated according to Profile (a), the two locations have enough time to almost reach the same soak temperature: exhibiting a smaller temperature difference of approximately 50K. As such, both cycles show variations in temperature between the two samples which may cause differences in the microstructure that is formed across the coil, as shown in Figure 1-5.

Therefore, depending on the annealing cycle, radiative property variations across the coil may produce non-uniform mechanical properties post-annealing. Figure 3-15 illustrates the effect of total hemispherical absorptivity variations at different coil locations on strip temperature as the coil travels through the furnace.

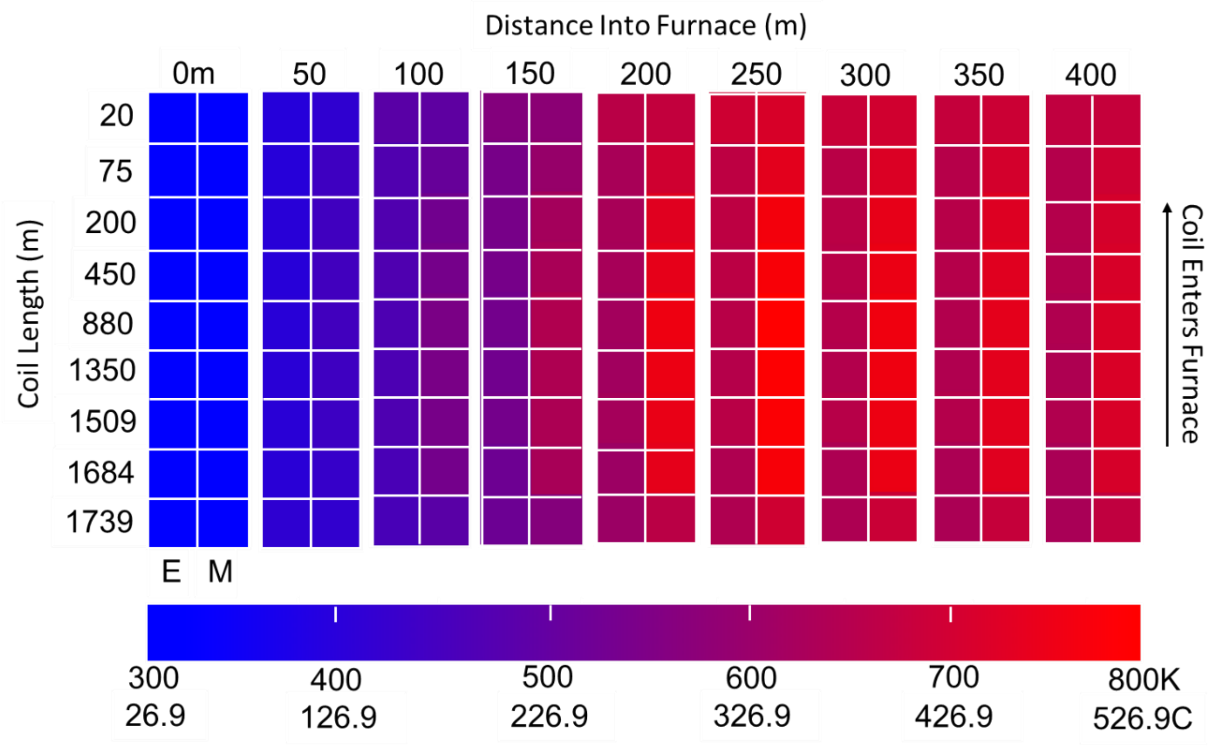

Figure 3-15: The temperatures of different coil locations at various distances into the furnace. The middle of the coil changes in temperature faster than the edge. This diagram follows the DP-980 heating schedule.

This work assumes that irradiation at any position *x* is uniform across the coil width, which may not be the case [15, 16]. Additionally, as the coil travels through the furnace, further variations may also arise in strip radiative properties due to changes in its surface state [32, 43, 42]. As discussed, the evolution of the strip surface state is often unpredictable and challenging to model analytically. As such, these changes may lead to more significant variations in strip temperature evolutions across the coil. However, as discussed earlier, future work should focus on empirically modelling these radiative property evolutions. In addition, variations in the pre-annealed surface state across the coil will impact how the radiative properties evolve at these different coil locations [32, 42].

Chapter 4 : Surface State Characterisation

This chapter discusses the experimental and theoretical work performed to elucidate the origins of the radiative property variations described in Chapter 3. First, methods used to characterise the surfaces, including optical profilometry, optical microscopy and scanning electron microscopy, are introduced. The initial analysis shows the existence of corrugated surface cavities on samples with larger spectral directional emissivities and total hemispherical absorptivities. Subsequently, this section explores the methodology adopted to quantify the number of cavities and highlights the use of the GOA ray-tracing algorithm to correlate the radiative properties of the samples to variations in surface topography. A replicant technique is then employed to improve surface topography acquisition inside the surface cavities, hence the GOA spectral emissivity predictions.

4.1: Mathematical Modelling of Surface Topography

In its cold-rolled and pre-annealed state, surface roughness effects dominate the radiative properties of AHSS; processes upstream of annealing, such as hot-rolling, acid-pickling, and cold-rolling, usually impart these topographical artefacts to the coil, as shown in Figure 1-3. Various studies have elucidated the effect of surface topography on the radiative properties of AHSS and other metals [37, 43, 46, 47]. For instance, Ham et al. [43] found a strong correlation between the average roughness, R_{a} of cold-rolled TRIP steel samples and their total normal emissivities. Lin et al. [37] correlated the spectral directional emissivities of AHSS to their surface slopes, R_{q}/τ; where R_{q} is the root-mean-squared (RMS) roughness,

$$R_{\mathrm{q}} = \sqrt{\frac{1}{L_{\mathrm{x}} \cdot L_{\mathrm{y}}} \cdot \int_0^{L\mathrm{x}} \int_0^{L\mathrm{y}} Z\left(x,y\right)^2 \cdot dx \cdot dy} \tag{4.1}$$

and τ is the correlation length. For a Gaussian surface, the correlation length is,

$$\tau = \frac{\sqrt{2} \cdot R_{\mathrm{q}}}{s_{\mathrm{r}}} \tag{4.2}$$

where s_{r} is the RMS slope,

$$s_{\mathrm{r}} = \sqrt{\frac{1}{L_{\mathrm{x}} \cdot L_{\mathrm{y}}} \cdot \int_0^{L\mathrm{x}} \int_0^{L\mathrm{y}} \left(\frac{\partial Z\left(x,y\right)}{\partial x}\right)^2 + \left(\frac{\partial Z\left(x,y\right)}{\partial y}\right)^2 \cdot dx \cdot dy} \tag{4.3}$$

L_x and L_y are the surface lengths in the *x* and *y* directions, respectively, and *Z* represents the surface height at a given *x* and *y* coordinate.

A 2D surface $Z = h(\mathrm{x, y})$ can be modelled using a height distribution function (HDF) and an auto-covariance function (ACF) [18, 37]. The HDF describes the distribution of heights above and below a mean plane. The ACF describes the distribution of the peaks and troughs in the *x* and *y* directions. In the case of a Gaussian surface, the distribution of heights is normal,

$$p(h) = \frac{1}{\sqrt{2 \cdot \pi \cdot {R_\mathrm{q}}^2}} \cdot \left(-\frac{h^2}{2 \cdot {R_\mathrm{q}}^2} \right) \tag{4.4}$$

$$C(x,y) = \exp\left(-\frac{x^2}{\tau_x^2} - \frac{y^2}{\tau_y^2} \right) \tag{4.5}$$

τ_x and τ_y are the correlation lengths in the *x* and *y* directions, respectively. The Gaussian assumption is valid for most surfaces generated randomly [18, 37, 48], such as during cold rolling (see Appendix B). For an isotropic surface, which has identical distributions of peaks and troughs in both *x* and *y* directions, Eq. (4.5) simplifies to

$$C(x,y) = \exp\left(-\frac{x^2 - y^2}{\tau^2} \right). \tag{4.6}$$

4.1 Surface Imaging Techniques

4.1.1. Optical Profilometry

Figure 4-1 shows the optical profilograms obtained from a subset of samples using a WYKO NT1100 optical profilometer with a lateral scanning resolution of approximately 1.927 μm.

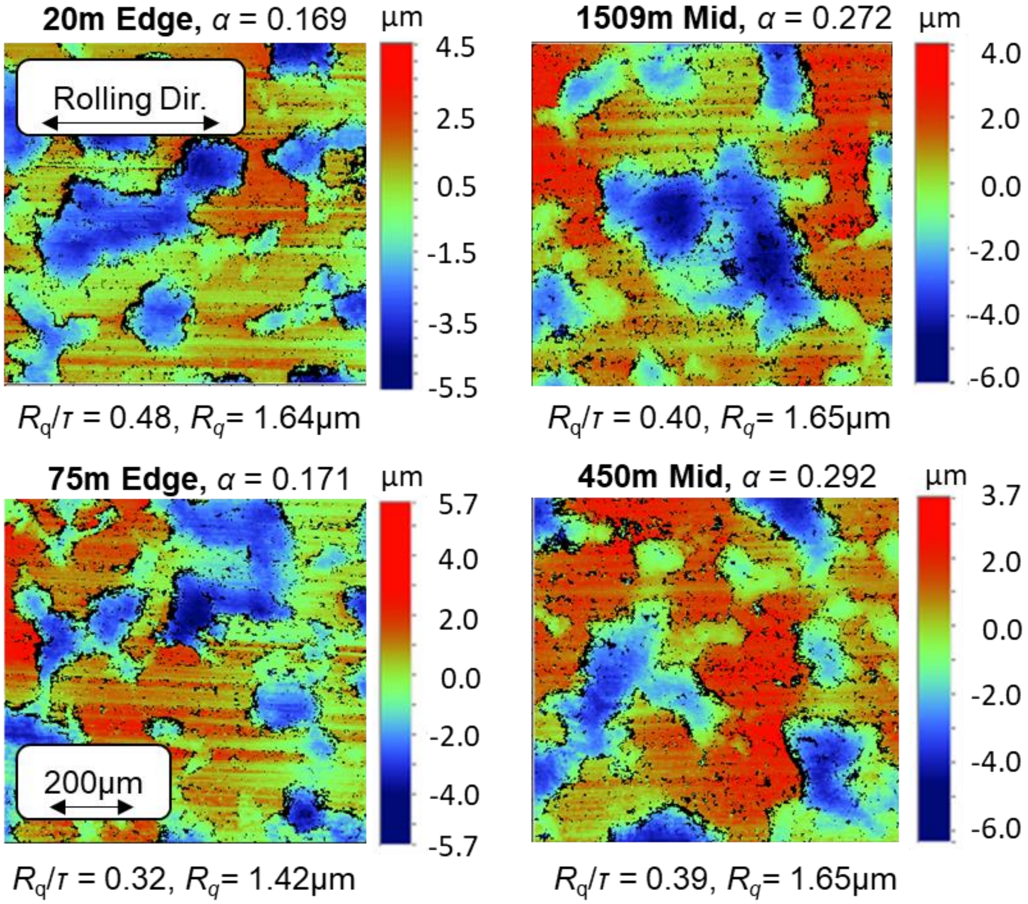

Figure 4-1: Optical profilograms of a subset of samples. The total hemispherical absorptivity (α) values presented are computed at T_{furnace} = 850 °C.

The optical profilograms do not reveal variations in surface topography between the Edge and the Middle of the coil. All profilograms show similar surface slopes, R_q/τ and RMS roughnesses, R_q, despite exhibiting different total hemispherical absorptivities. The insufficient lateral resolution of the optical profilometer is responsible for this lack of correlation.

Ham et al. [43] suggested that microscale topographical features, ~*O*(0.1 μm), strongly influence strip radiative properties, which they inferred from profilograms like the ones shown in Figure 4-1 using a wavelet filtering algorithm. Lin et al. [37, 46] then adopted this algorithm to correlate the radiative properties of AHSS with their surface topographies using the GOA ray-tracing model and the EM Davies' theory.

Lin et al. [37, 46] analysed this approach's veracity by comparing the surface roughness parameters inferred using the optical profilometer and the filtering algorithm with those obtained from atomic force microscopy measurements with a lateral resolution of ~0.02 μm. This work shows that surface height maps generated using depth mapping on an optical microscope with a lateral resolution of ~0.1μm are sufficient to model the radiative properties of the AHSS samples using a GOA ray-tracing model and an ANN, as shown in Sec. 4.3.1 and Chapter 6. However, some samples have surface cavities that must be treated as blackbodies, as shown in Chapter 6.

4.1.2. Optical Microscopy

The samples highlighted by the black circles in Figure 3-11 are analysed using a Keyence VHX-5000 optical microscope (with a lateral resolution of ~0.104 μm) to account for the limitation of the optical profilometer. Figure 4-2 shows optical micrographs of the ten samples. At the finer lateral resolution of 0.104 μm, the samples extracted from the middle of the coil show a larger number of dark patches compared to samples extracted from the edge; correspondingly, the mid samples also show larger total hemispherical absorptivity values.

The dark patches represent surface cavities that trap visible light, preventing the Keyence microscope (and other optical-based imaging techniques) from capturing the cavity's surface topography. This trapped light contributes to the higher spectral emissivities and total absorptivities of the Mid samples through higher-order scattering events, as will be discussed further in Sec. 4.3.1.

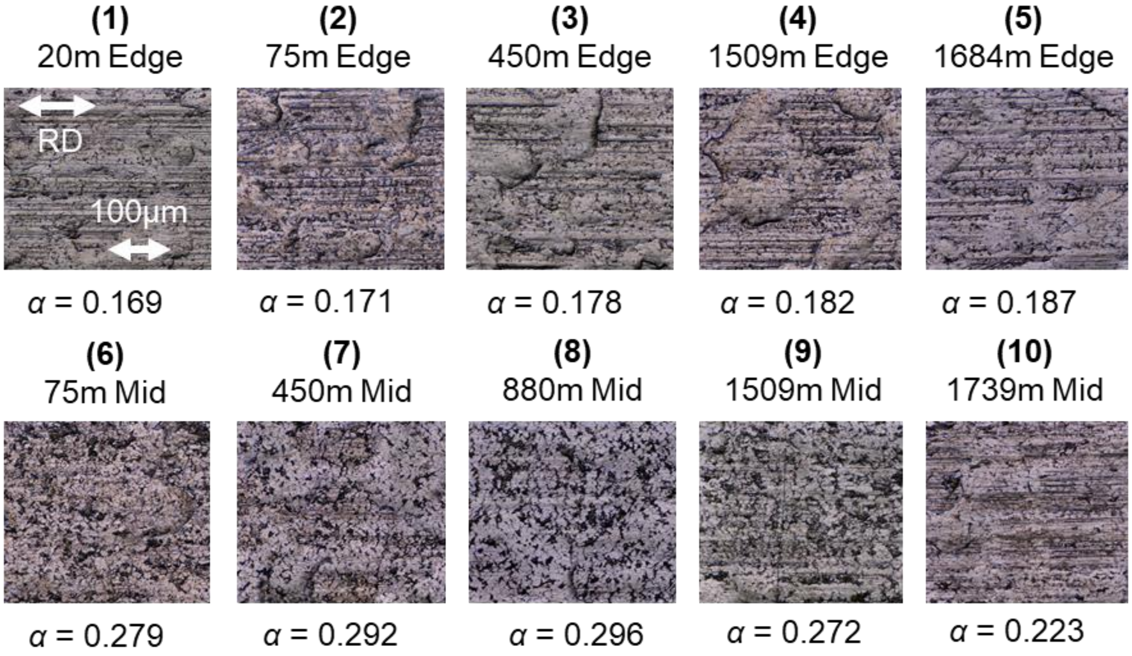

Figure 4-2: Optical micrographs of the ten selected samples taken with a lateral resolution of 0.104 µm. At this magnification, a larger number of dark patches are visible on the surfaces of the Mid samples compared to the Edge samples.

The Keyence optical microscope generates digitised surface height maps through 3D depth mapping. During this process, the digital microscope estimates a height profile by analysing the movement of the lens along the z-axis by moving through different focus planes on the image as regions with different heights come into focus at different focusing lengths. Figure 4-3 shows the digitised 3D surfaces obtained using the Keyence microscope for two select samples (20m Edge & 1509m Mid). Scanning areas of approximately 500 µm × 500 µm are chosen by referring to previous studies that have analysed the surface topography of AHSS [37, 43]. These studies deemed that such a scanning size is representative of the sample whilst minimising undue analysis time associated with larger scanning areas. Appendix C shows the testing of larger scan areas on select samples to validate this assumption.

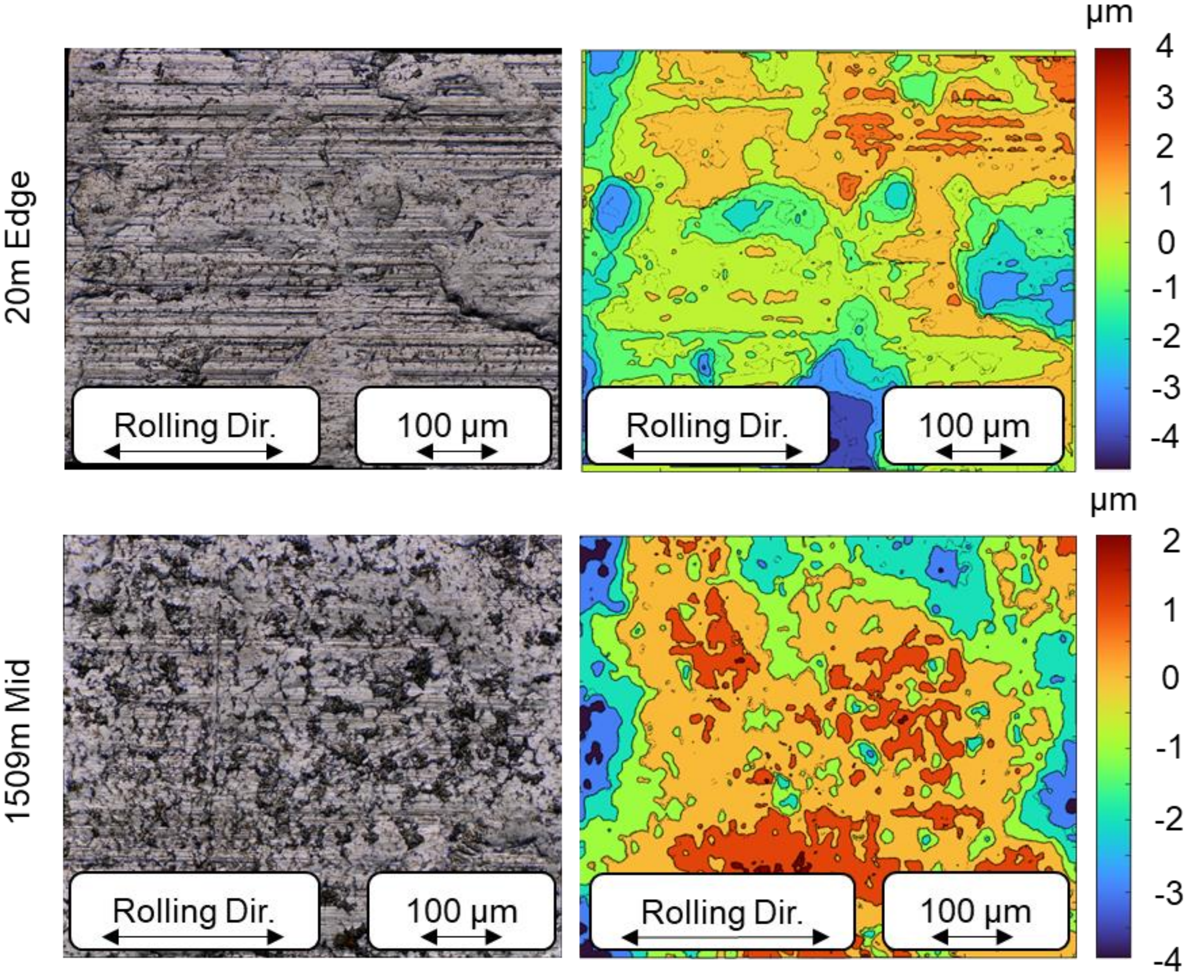

Figure 4-3: 3D digitised surface height maps obtained using the Keyence optical microscope for two select samples (20m Edge and 1509m Mid samples).

The dark patches appear as low-lying areas in contrast to the surrounding region; however, as the microscope cannot focus on the features inside the cavities, it cannot capture the finer surface topography within, which are revealed by the SEM images in Figure 4-5. As such, the surface roughness parameters computed using depth mapping are representative of the surface topography outside the cavities. Table 4-1 summarises the roughness statistics of all ten samples in Figure 4-2 inferred through depth mapping. This finer lateral resolution of ~0.104 µm allows for capturing the high-frequency topography artefacts that affect the radiative properties, as suggested by Ham et al. [43] in areas outside the cavities.

Sample	R_q (μm)	τ (μm)	R_q/τ	α
1	1.361	5.477	0.248	0.169
2	1.235	5.888	0.210	0.171
3	1.678	7.318	0.229	0.178
4	1.481	5.682	0.261	0.182
5	1.519	6.034	0.252	0.187
6	0.930	4.013	0.232	0.279
7	1.441	5.080	0.284	0.292
8	1.423	5.224	0.272	0.296
9	1.469	5.431	0.270	0.272
10	1.329	5.594	0.238	0.223

Table 4-1: Summary of roughness statistics and total hemispherical absorptivities for samples analysed using the digital microscope shown in Figure 4-2.

Figure 4-4 shows the relationship between the inferred surface slopes, R_q/τ and the total hemispherical absorptivities of the samples. A larger number of scattering events for surfaces with higher slopes produces an upward trend [37]. However, the correlation is not very strong, as evidenced by the low R^2 value. The radiative properties for the samples analysed here cannot be fully defined using the inferred surface slope alone as it does not account for the surface cavities that act as perfect emitters (blackbodies) of EM radiation. Chapter 6 discusses the influence of these cavities.

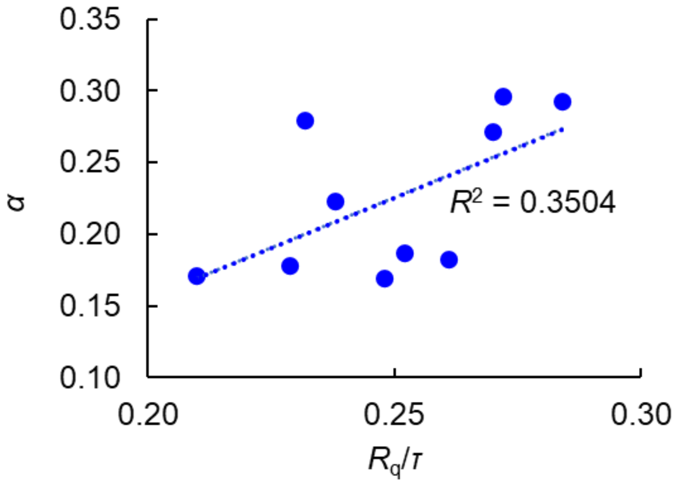

Figure 4-4: Relationship between surface slope and total hemispherical absorptivity for the ten analysed samples in Figure 4-2.

4.1.3 Scanning Electron Microscopy

This section explores the surface topography inside the dark patches/cavities using a Zeiss Merlin scanning electron microscope (SEM) with an acceleration voltage of 20kV. The same location on the 1509m Mid sample is analysed using the optical microscope and the SEM. The SEM imagery reveals a highly corrugated surface inside the cavity, as shown in Figure 4-5.

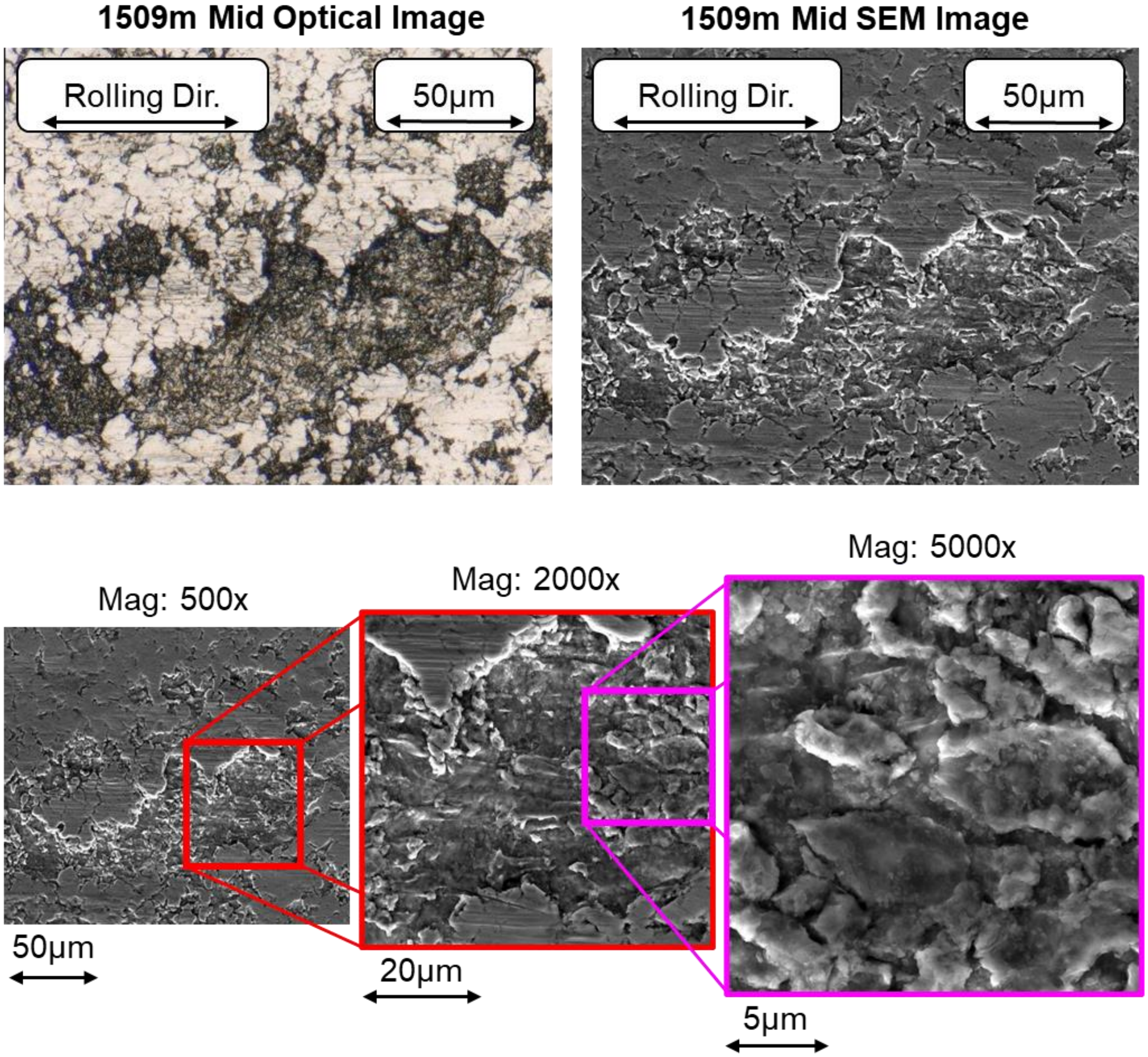

Figure 4-5: Comparison of an optical image and an SEM image (20kV) taken at the same location on the 1509m Mid sample. The SEM image reveals a highly corrugated surface inside the dark patches.

4.2 Cavity Quantification

The optical images from the Keyence microscope are then analysed further to quantify the number of surface cavities and to test whether a correlation exists between surface cavity coverage and the radiative properties of the surfaces. An image thresholding approach shows that the surface cavities strongly drive the total hemispherical absorptivities.

4.2.1 Image Thresholding Approach

Image thresholding exploits the dark colour of the cavities in the optical micrographs to infer the total surface area occupied by the cavities. Surface images are imported to MATLAB® as RGB matrices, where an RGB array represents each pixel of the image. The images are then converted to greyscale with pixel intensities ranging between 0-255, producing an 8-bit image. The contrast of the greyscale images is normalised through gamma correction using MATLAB®'s *imadjust* function for accounting for the microscope's varying exposure and lighting parameters.

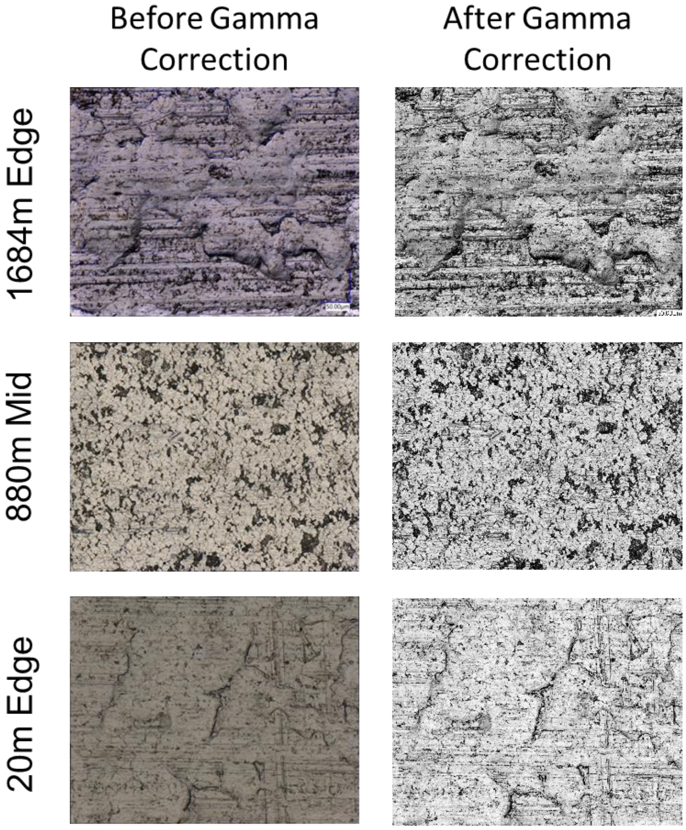

Figure 4-6: Effect of gamma correction on the contrast of a subset of samples. This procedure allows for normalising images in the case of varying microscope imaging characteristics like exposure and lighting settings.

Pixels with values less than 95 are considered dark, where 95 is chosen heuristically by visually inspecting the cavities in the optical micrographs for a subset of samples. Finally, the number of bright pixels in the binary image is divided by the number of total pixels to obtain a cavity percentage for each sample. Figure 4-7 shows an example binary image for the cavity in Figure 4-5.

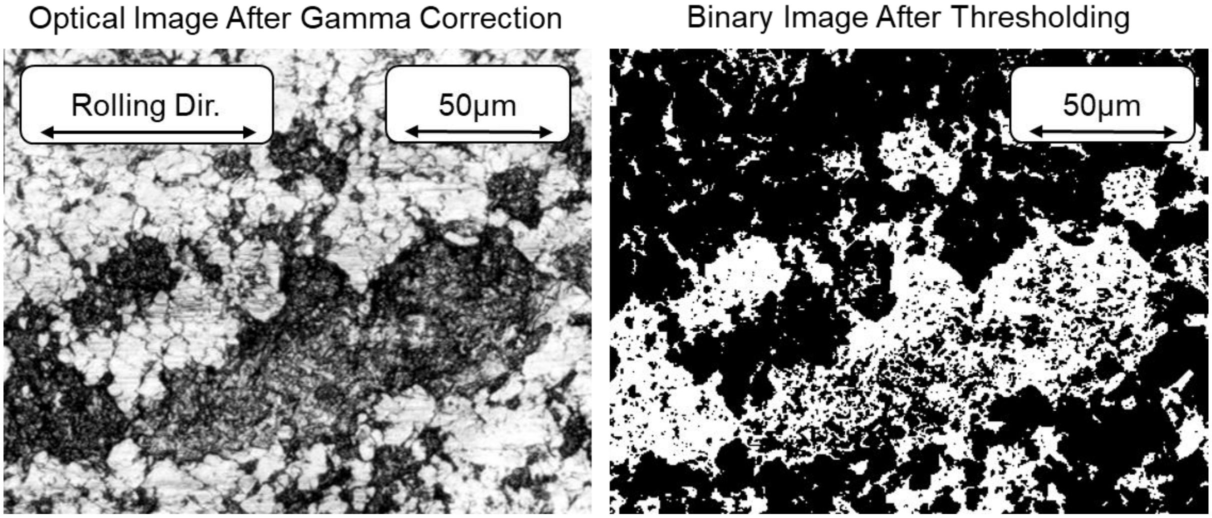

Figure 4-7: Binary image of the cavity shown in Figure 4-5. The correct regions have been identified using the image thresholding approach.

The strength of the correlation between cavity percentage and total hemispherical absorptivity highlights these cavities' strong impact on the samples' overall radiative properties, as shown in Figure 4-8 (c) and (d). Additionally, the poor correlation between surface slope and cavity percentage further bolsters the idea that the Keyence microscope cannot capture the surface topography inside the cavities, which causes them to behave as blackbodies.

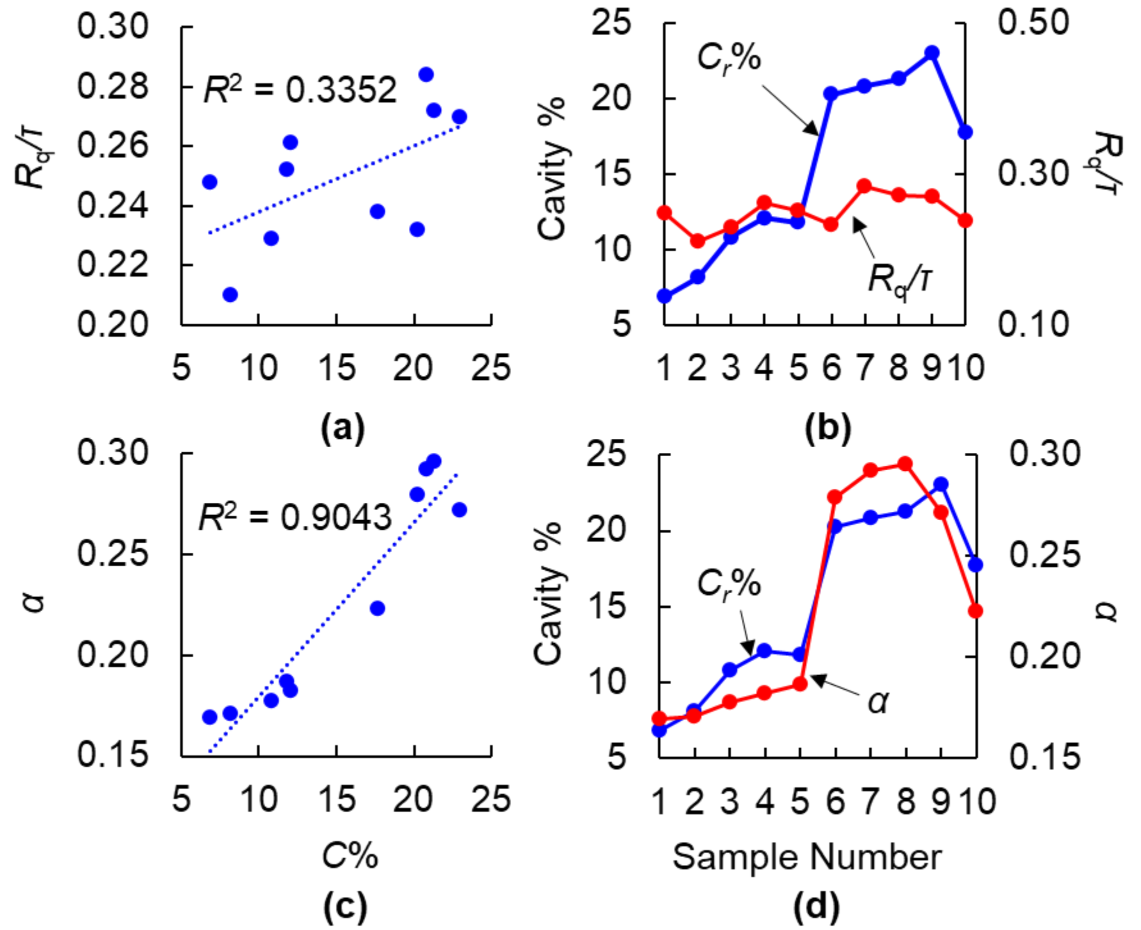

Figure 4-8: Relationship between cavity percentage and total hemispherical absorptivity over the ten analysed samples in Figure 4-2 and Table 4-1.

4.3 GOA Ray-Tracing Model

This section uses the GOA ray-tracing algorithm to theoretically model the steel radiative properties using the depth-mapped surface height data as a boundary condition. The GOA algorithm is a Monte Carlo ray-tracing procedure wherein many ray bundles are traced through their interactions with surface boundaries until they have scattered away from the surface [18, 37, 49]. When an electromagnetic wave impinges on an opaque conducting surface, its energy is absorbed or reflected. The bi-directional reflectance distribution function (BRDF) [16, 18, 37, 48, 50, 49],

$$\rho_{\lambda}\left(\Omega_{\mathrm{i}},\Omega_{\mathrm{r}}\right)=\frac{L'_{\lambda,\mathrm{i}}\left(\Omega_{\mathrm{i}}\right)}{L'_{\lambda,\mathrm{r}}\left(\Omega_{\mathrm{r}}\right)\cdot\cos\left(\theta_{\mathrm{r}}\right)\mathrm{d}\Omega_{\mathrm{r}}} \tag{4.7}$$

expresses the angular distribution of this reflected energy, where $L'_{\lambda,\mathrm{i}}(\Omega_{\mathrm{i}})$ and $L'_{\lambda,\mathrm{r}}(\Omega_{\mathrm{r}})$ represent the incident and the reflected spectral intensities, respectively. Here, θ_{r} is the polar angle of reflection, Ω_{i} is the direction of incidence, and Ω_{r} is the direction of reflection; Figure 4-9 (a) illustrates these quantities. Marginalising the BRDF over a hemisphere yields the spectral directional-hemispherical reflectivity,

$$\rho_{\lambda,\mathrm{d-h}}\left(\Omega_{\mathrm{i}}\right)=\frac{1}{\pi}\cdot\int_{2\pi}\rho\left(\Omega_{\mathrm{i}},\Omega_{\mathrm{r}}\right)\cdot\cos\left(\theta_{\mathrm{r}}\right)\mathrm{d}\Omega_{\mathrm{r}} \tag{4.8}$$

The GOA algorithm computes the BRDF by modelling the energies of the incident and reflected ray bundles and provides an approximate spectral reflectivity prediction through a Monte Carlo integration. The procedure is less computationally expensive than the more rigorous approach of directly solving Maxwell's equations [18, 37]. The GOA approach models each reflection as specular, and the surface is assumed to be locally optically smooth at each reflection point, as illustrated in Figure 4-9 (b).

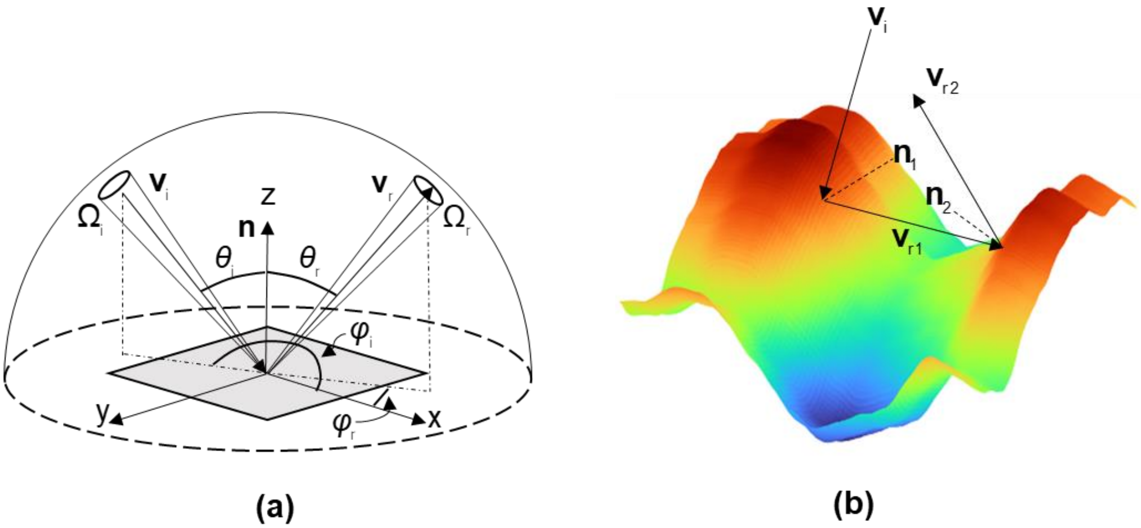

Figure 4-9: (a) Parameters used to define the BRDF. (b) The path of an incident ray as it interacts with a random Gaussian surface.

The energy of an incident ray, e_{i}, is proportional to the projected incidence area according to Lambert's cosine law with respect to the local normal at the reflection point. Bergström et al. [18] decomposed the incident energy into s- and p-polarized components, e_{is}, and e_{ip}, according to the global reference frame (w.r.t. to the normal of the mean plane of the surface) to account for the change in the polarization of the incident ray upon reflection. The reflected energies e_{rs}, and e_{rp} are then given by

$$\begin{bmatrix} e_{\mathrm{r,s}} \\ e_{\mathrm{r,p}} \end{bmatrix} = \begin{bmatrix} \rho_{\mathrm{ss}} & \rho_{\mathrm{ps}} \\ \rho_{\mathrm{sp}} & \rho_{\mathrm{pp}} \end{bmatrix} \cdot \begin{bmatrix} e_{\mathrm{i,s}} \\ e_{\mathrm{i,p}} \end{bmatrix} \tag{4.9}$$

where ρ_{ss} and ρ_{pp}, and ρ_{sp} and ρ_{ps} are the co- and cross-polarised reflectivities, which are computed using the incident and reflected ray vectors, the s- and p-polarised components of the rays, and the Fresnel amplitude reflectivities, R_{s} and R_{p},

$$R_{\mathrm{s}} = \frac{\left(n_1 \cdot \cos\left(\theta_{\mathrm{i}}\right) - p\right)^2 + q^2}{\left(n_1 \cdot \cos\left(\theta_{\mathrm{i}}\right) + p\right)^2 + q^2} \tag{4.10}$$

$$R_{\mathrm{p}} = \frac{\left(p - n_1 \cdot \sin\left(\theta_{\mathrm{i}}\right) \cdot \tan\left(\theta_{\mathrm{i}}\right)\right)^2 + q^2}{\left(p + n_1 \cdot \sin\left(\theta_{\mathrm{i}}\right) \cdot \tan\left(\theta_{\mathrm{i}}\right)\right)^2 + q^2} \times R_{\mathrm{s}} \tag{4.11}$$

$$p^2 = \frac{1}{2} \cdot \left(\sqrt{\left(n_2^2 - k_2^2 - n_1^2 \cdot \sin^2(\theta_\mathrm{i})\right)^2 + 4n_2^2k_2^2} + n_2^2 - k_2^2 - n_1^2 \sin^2(\theta_\mathrm{i}) \right) \tag{4.12}$$

$$q^2 = \frac{1}{2} \cdot \left(\sqrt{\left(n_2^2 - k_2^2 - n_1^2 \cdot \sin^2(\theta_\mathrm{i})\right)^2 + 4n_2^2k_2^2} - n_2^2 + k_2^2 + n_1^2 \sin^2(\theta_\mathrm{i}) \right) \tag{4.13}$$

As discussed, the optical constants for specific AHSS alloys are not readily available; therefore, this work uses the values for pure iron instead [37, 38, 39], as discussed in Sec. 3.3.1.

Assuming a specular reflection, the reflected ray is,

$$\mathbf{v}_\mathrm{r} = \mathbf{v}_\mathrm{i} - 2 \cdot \mathbf{n} \cdot \left(\mathbf{v}_\mathrm{i} \cdot \mathbf{n}\right) \tag{4.14}$$

where **n** is the local surface normal vector at the reflection point, the algorithm also accounts for shadowing effects and multiple scattering events through simple geometric arguments [35,46]. Shadowing occurs when the geometry of the surface shields certain areas from the incident light, and multiple scattering events usually occur within surface cavities.

Tang et al. [49] delineated the validity regime of the 1D GOA model by comparing its predictions to solutions obtained through electromagnetic (EM) wave theory models. They showed that 1D GOA predictions are accurate when $R_\mathrm{q}\cos(\theta_\mathrm{i}) / \lambda > 0.2$ and $R_\mathrm{q} / \tau < 1$. Tang and Buckius [50] then hypothesized that the validity regions for 1D and 2D GOA models are the same. This work uses the MATLAB® GOA code published by Bergström et al. [18] with modifications to analyse different incident wavelengths of light between 0.5 – 20 μm and specific conditions to model the cavities as blackbodies, as discussed in Chapter 6.

Figure 4-10 shows the predictions made by the GOA model. The GOA model provides accurate spectral emissivity predictions for the Edge samples but underpredicts those of the Mid samples. This underprediction is due to the Keyence microscope's inability to capture accurate surface height maps inside the cavities (which makes them act as blackbodies) due to the trapping of visible light within them. Therefore, the GOA model does not capture this blackbody effect when using the Keyence height data as a boundary condition for cavity-rich samples.

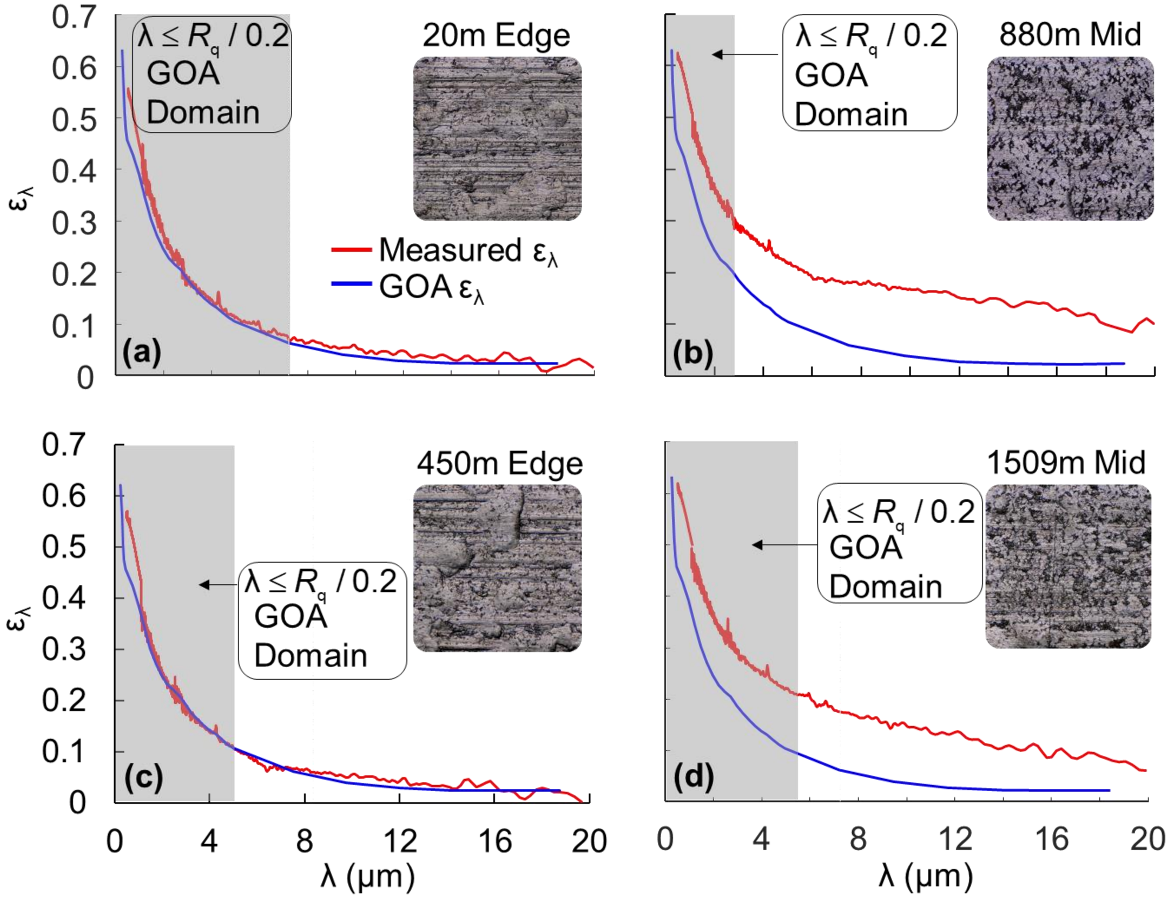

Figure 4-10: GOA spectral emissivity predictions for a subset of samples, comparing GOA results between the (a) and (c) Edge and the (b) and (d) Middle of coil.

4.3.1 Surface Replication Technique

This section further explores the cavity's surface topography using a surface replication technique. The replication technique creates a negative cast of the surface using a hardening silicone paste (Provil® Novo), which converts the surface cavities into peaks. The surface replicates are then imaged using the Keyence optical microscope and inverted numerically to obtain the true surface height profiles of the samples. Figure 4-11 shows the application gun, the silicone paste, the sample, and the replicate.

Figure 4-11: Surface replication apparatus, Top: Application gun, Bottom: 1509m Mid sample and its replicate.

The replicate technique is performed on the sample shown in Figure 4-2 (1509m Mid), after which the same cavity shown in Figure 4-5 is imaged on the replicate surface. The replicate technique captures the topography within the cavity shown by the red boxes (Figure 4-11) since it has a significant difference in height in contrast to its surroundings (Figure 4-11 (b)).

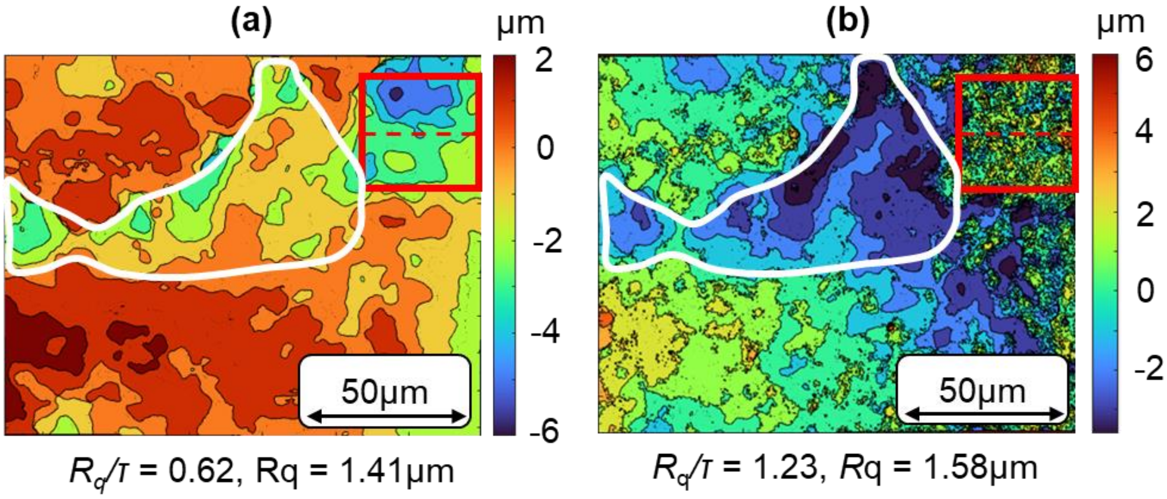

Figure 4-12: Surface height profile of the cavity shown in Figure 4-5 obtained by imaging the (a) original steel surface and (b) the replicate surface.

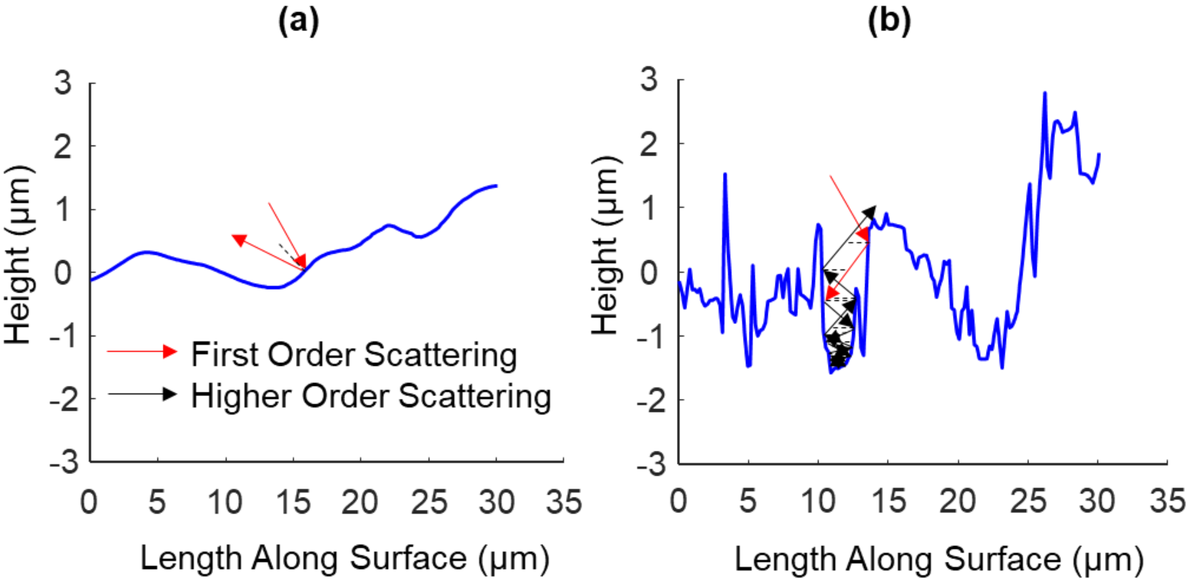

Figure 4-13: Linear height profiles along the red dotted lines. The replicate profile reveals a much rougher surface inside the cavity. A larger number of higher order scattering events are also visible which contribute to the higher spectral emissivities and total hemispherical absorptivities.

Figure 4-13 shows the 1D surface height profile obtained along the red dotted lines in Figure 4-12. The high spectral directional and total hemispherical emissivities of cavity-rich samples may be intuited by examining the path of an incident beam as it interacts with the surface. The rougher surface inferred using the replicate leads to more higher-order scattering events. The cavity is imaged again using the SEM at 54° to validate the spikes in the replicant profile and ensure they are not measurement noise. Figure 4-14 compares the replicant surface height profile, and the SEM image; the spikes seen in the replicate profile are also present in the SEM image, as shown by the red circles.

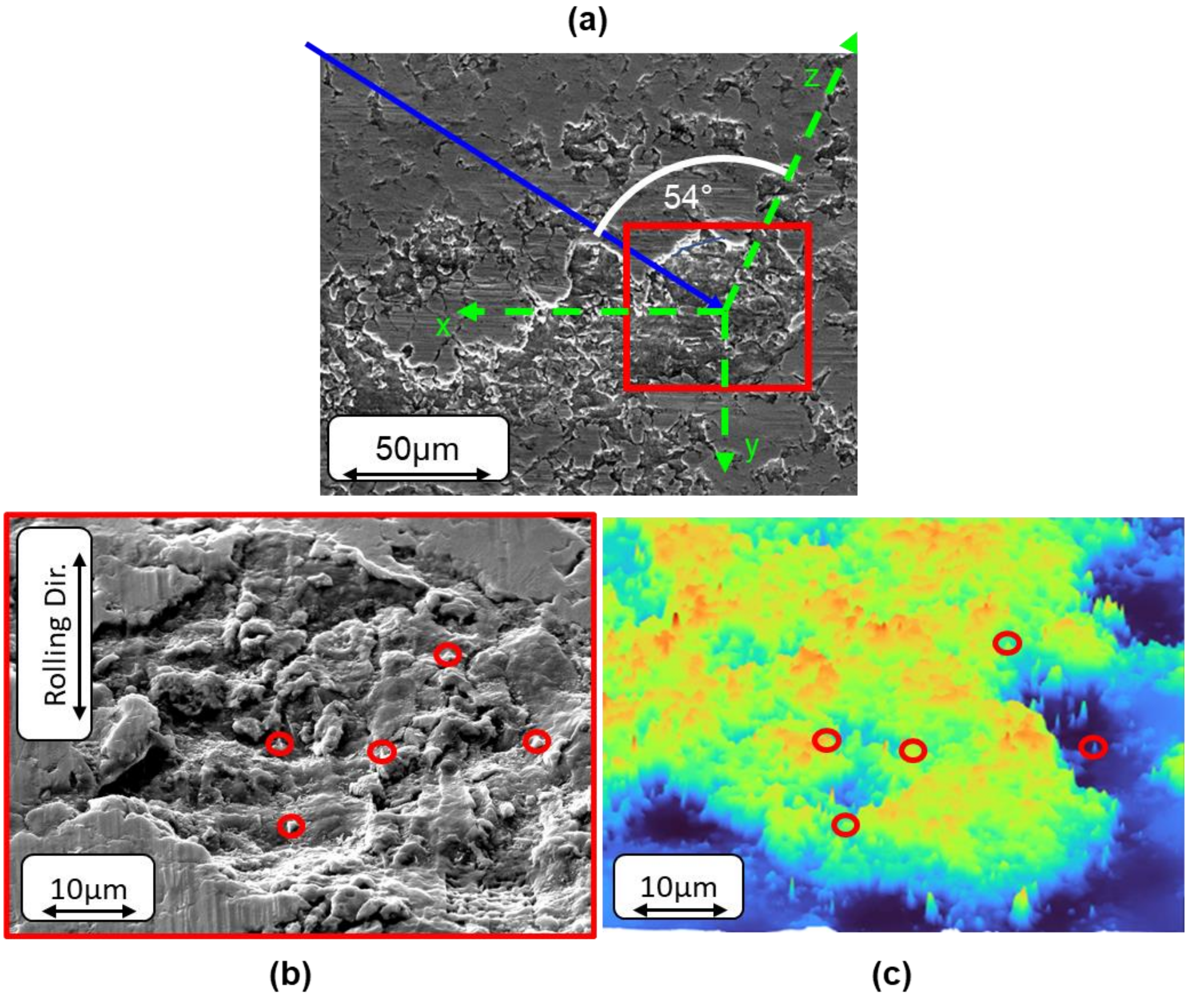

Figure 4-14: Comparison of cavity surface taken using an SEM at 54°, and the replicant surface height profile at 54°. The red circles represent the surface peaks visible in both the SEM image and the replicant surface height profile.

Subsequently, the replicate surface height profile serves as a boundary condition for the GOA ray-tracing model, revealing a more accurate GOA spectral emissivity prediction within its validity regime, as shown in Figure 4-15.

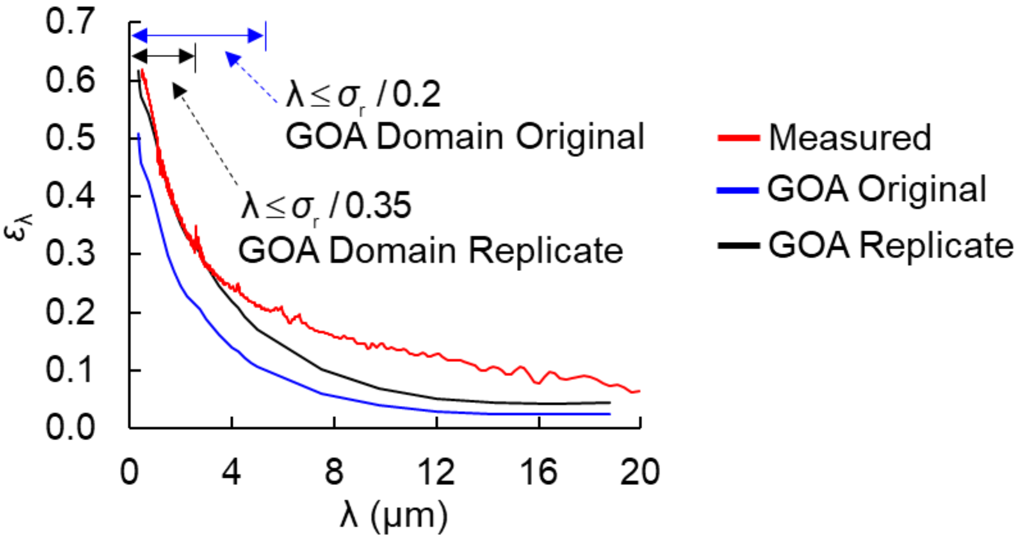

Figure 4-15: GOA spectral emissivity predictions using the surface height profile from the replicant technique. An improved GOA prediction is obtained within its validity domain.

Notably, the GOA predictions for the edge samples are accurate even outside the GOA validity regime (Figure 4-10); however, the algorithm is only accurate inside the validity regime for the 1509m mid-sample. This discrepancy can be attributed to the lower number of higher-order scattering events and EM diffraction effects occurring on the surface of the edge samples at longer wavelengths due to fewer cavities and lower surface roughness [37]. For longer wavelengths, such as those critical for calculating infrared heat absorption within the furnace, a rigorous EM solution may be required for the mid-samples, as shown in the GOA validity regime map created by Tang et al. [49]. Chapter 6 proposes a machine learning data-driven model trained on empirical data to address this issue, requiring less computational effort than a rigorous EM approach.

Chapter 5 : Cavity Formation

The previous chapter describes how surface cavities influence the radiative properties of the steel. This chapter explores the possible reasons for surface cavity formation during processes upstream of annealing. A deeper understanding of the origins of these cavities will allow steel manufacturers to improve their industrial processes to minimise radiative property variations across AHSS coils in their cold rolled and pre-annealed condition before they enter an annealing furnace.

5.1 Literature on Surface Cavity Formation

Few studies have explored the reasons for cavity formation during processes upstream of annealing. However, a recent study by Köpper et al. [51] showed that cavity formation occurs due to the dissolution of selective grain boundary oxides during acid-pickling that initially form during the hot-rolling process in low-oxygen conditions.

They suggest that an oxygen depletion zone may be created between external oxide scales and the steel substrate when a hot-rolled coil is a wound; within this depletion zone, selective Mn, Cr and Si oxide nodules may form due to the low oxygen content like the ones formed in a reducing atmosphere during intercritical annealing [32, 42]. Acid-pickling then dissolves the external oxide scale and some selective oxide nodules in the depletion layer, as shown in Figure 5-1. Finally, cold rolling flattens the remaining oxide nodules and some cavities.

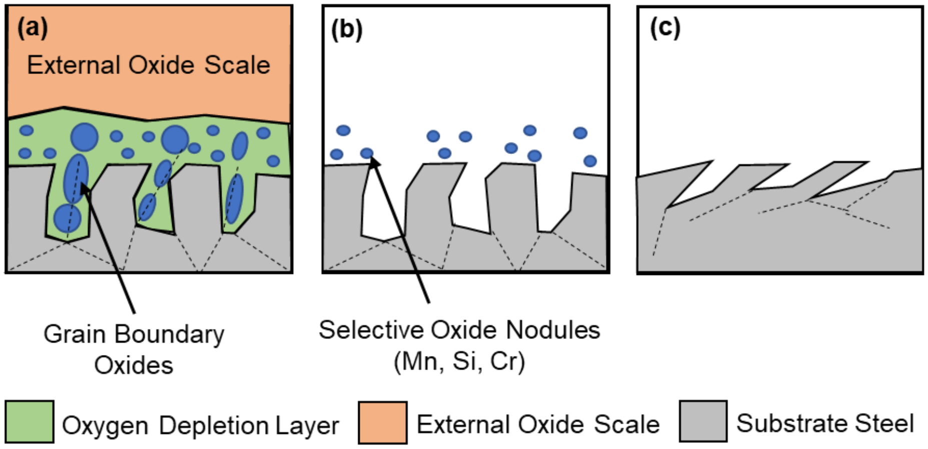

Figure 5-1: Selective oxidation in the oxygen depletion zone created between external oxide scale and the steel substrate after the (a) hot-rolling process. Some of these oxide nodules are dissolved during (b) pickling and subsequently get flattened during (c) cold-rolling. Image adapted from Ref. [51]. Dashed lines represent grain boundaries.

Figure 5-1 shows surface cavities on samples analysed in Ref. [51]; the sample with more cavities shows deformed grain boundary oxides in the cross-section image.

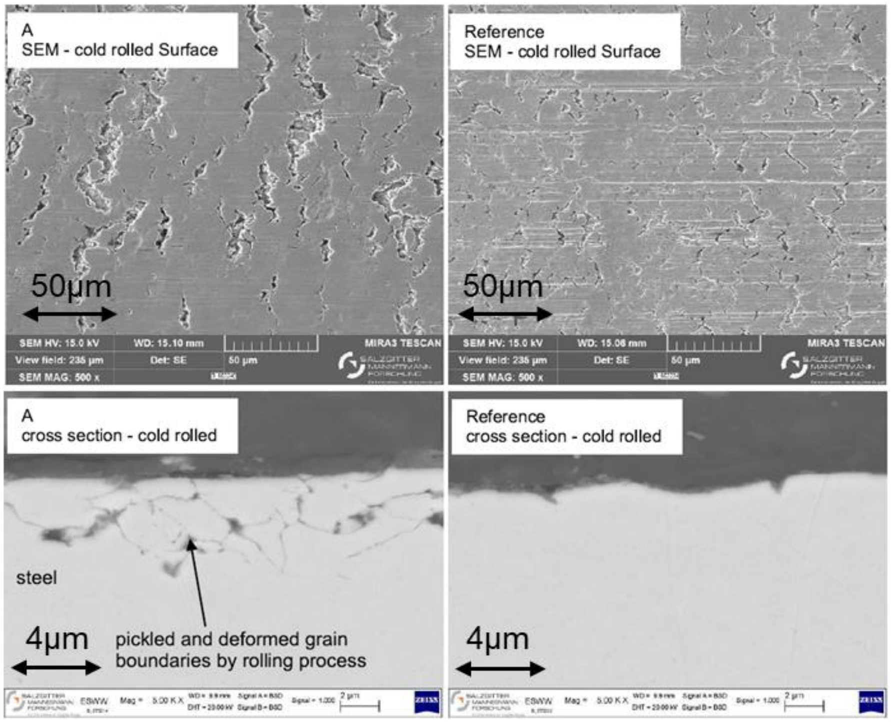

Figure 5-2: Surface cavities seen in samples analysed by Köpper et al [51], the cross-section SEM image of the surface with cavities shows cracks along the grain boundaries due to oxide dissolution during pickling.

Additionally, the sample with fewer cavities shows deeper rolling grooves; this suggests that they are flattened during the cold-rolling process, producing micro flaps as hypothesised by Etzold et al. [52] and Ham et al. [43]. Figure 4-2 shows that samples from the Edge of the coil show deeper rolling grooves than the Mid samples, suggesting non-uniform cold-rolling characteristics across the coil width.

As grain-boundary oxidation, acid-pickling, and cold-rolling may be responsible for surface cavity formation, this chapter analyses DP800 and DP980 samples showing grain boundary oxidation from a hot-rolled coil (processed on an industrial line), which are acid-pickled (45s-180s) and cold-rolled (1% - 53% thickness red.) to different extents in a lab environment (see Figure 5-3). Through discussions with industry, it is hypothesised that external oxide scales are entirely removed after ~50-60 s, and the pickling acid completely dissolves the oxide nodules formed in the depletion zone at approximately 120 s for samples with heavy internal oxidation.

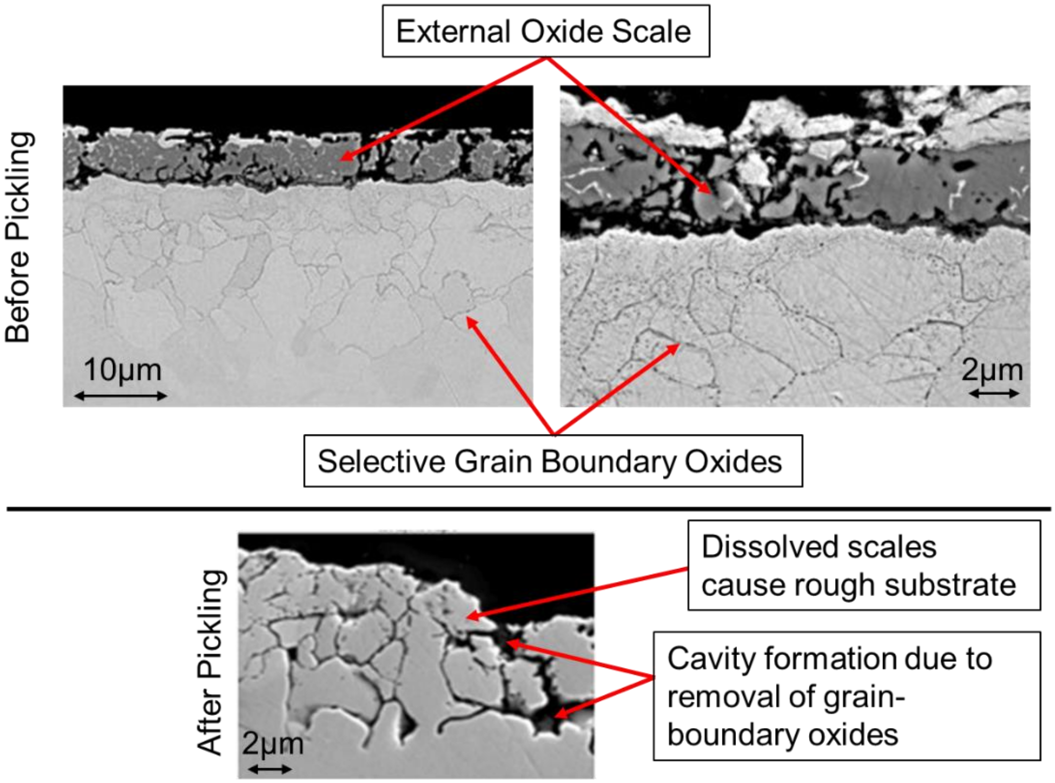

Figure 5-3: SEM cross-section images of one of the analysed samples (pickled to ~50s) provided by our industrial partner. External and grain boundary oxides are removed by pickling leading to a roughened substrate surface and surface cavities, post-pickling. (SEM Images from partner). Higher magnification SEM images are required to ascertain if oxide nodules are present on the surface, as performed in Ref. [46]

The reflectance spectra of certain under-pickled samples (for pickling times less than ~50s) that are cold-rolled to lesser thickness reductions (1-5% thickness red.) show a similar trend to annealed samples (in a reduction atmosphere) with selective oxide nodules analysed by Lin et al. [46] (Figure 5-4). These samples show low spectral reflectivities at shorter wavelengths [46, 51], which may be attributed to the existence of surface oxide nodules. SEM and X-ray diffraction (XRD) spectroscopy may further validate this finding. Remnant external oxide scales (the amber region in Figure 5-1) are also visible to the naked eye on specific samples (see Figure 5-5).

For increased pickling times and the cold-rolling reductions of 180s and 53%, respectively, the reflectance spectra trends approach those of as-received roughened samples analysed by Lin et al. [46], as the oxide nodules are either dissolved or flattened. On an industrial line, the coils are usually cold-rolled to a reduction of ~53% (typical of the industrial process) and either adequately or over-pickled to remove all oxides (120 s – 180 s) thoroughly; therefore, surface cavities and roughness effects should primarily influence the radiative properties of a cold-rolled coil on an industrial line as observed in Chapters 3 and 4.

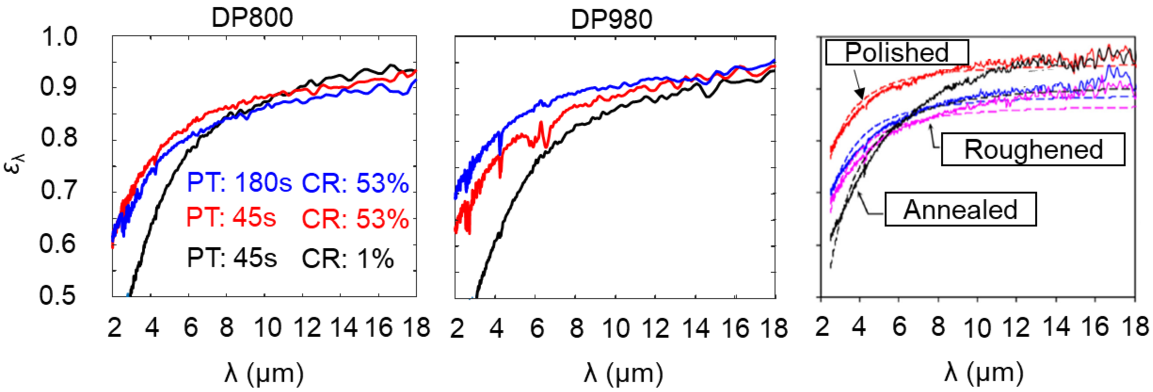

Figure 5-4: Similarity of the reflectivities of under-pickled samples and those of certain annealed samples showing oxide nodules, analysed by Lin et al. [46]**.**

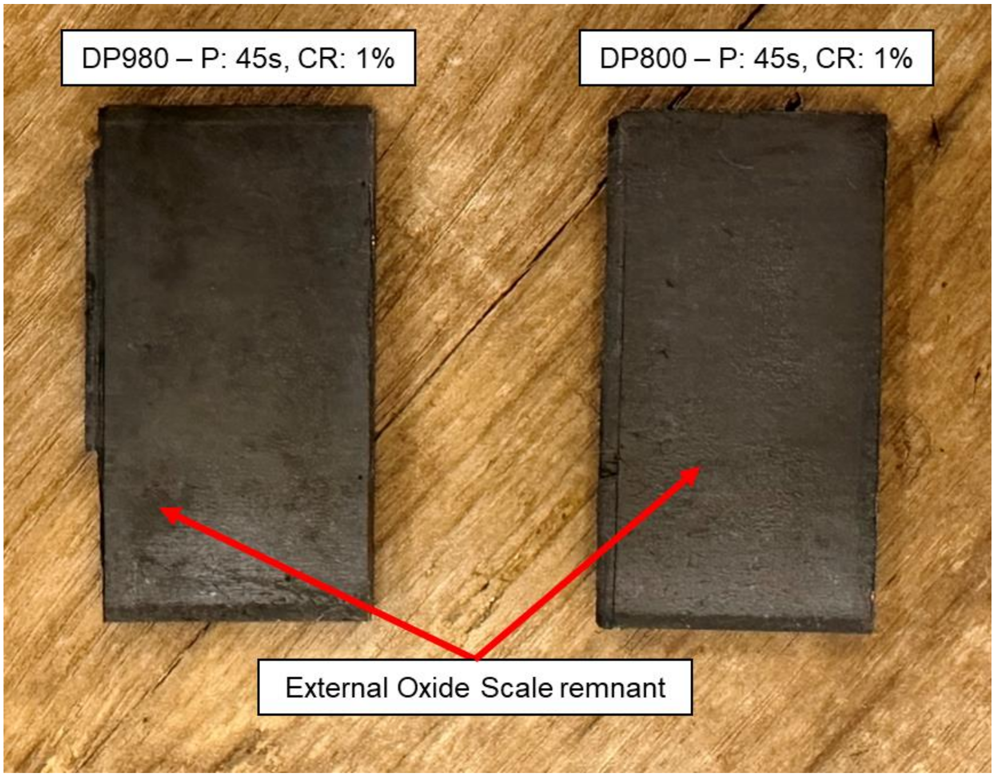

Figure 5-5: External oxide scale remnant visible on certain under-pickled samples represented by amber region in Figure 5-1.

The following section uses a full-factorial analysis to study the impact of acid-pickling time, cold-rolling thickness reduction and steel type on cavity formation and strip radiative properties.

5.2 Factorial Design-of-Experiments Approach

The factorial design-of-experiments approach helps elucidate the combined effect of various process parameters on a response variable of interest. A commonly used factorial model is the 2^k design, which analyses a k number of factors at two levels [53] (high and low levels). This model type is helpful in the early stages of an analysis, where the effect of various factors on the response variable is unknown; hence they are known as "factor screening” experiments. The method assumes a linear relationship between the response variable and each factor, as there are two levels for each factor, and that assumption is subsequently validated using residual analysis.

Various industries have implemented this technique. For example, in the context of AHSS pyrometry, Suleiman et al. [32] applied a $2 \times 2 \times 2 \times 3$ model to study the effect of the annealing dew point temperature, the Si/Mn ratio of the steel, the RMS surface roughness, and wavelengths on how the spectral directional emissivity of AHSS may vary during annealing.

5.2.1 2^k - Factorial Design for Cavity Formation/Flattening

Here, a 2^3 - factorial design model is implemented to elucidate the combined effect of acid-pickling time, cold-rolling reduction, and the alloy composition of the steel (DP800 or DP980) on the formation/flattening of cavities and the radiative properties of AHSS samples. In addition, the Si/Mn ratio of the steel is used as a factor to study the impact of alloy composition on the formation of Mn and Si grain boundary oxides during hot rolling, as Köpper et al. [51] hypothesised that the dissolution of these oxides leads to surface cavities during acid-pickling. This analysis extracts all samples from a hot-rolled coil from the mid-width and tail sections.

Due to physical limitations and cost, only a single replicate is available at each factor combination; therefore, widening the difference between the high and low levels of the factors as much as possible ensures that the model is not overturned [53]. Therefore, 120 s and 180 s and 1% and 53% are used for pickling times and cold rolling reduction percentages, respectively. These pickling times entirely dissolve all internal and external oxides; therefore, roughness effects dominate the radiative properties, which is more representative of the industrial process. Industry partners suggested these pickling times, as discussed previously.

The factors shown in Table 5-1 are applied in different combinations (Table 5-2) to study their individual and interaction effects on the response variables of cavity percentage, spectral emissivities at select wavelengths between 0.5 and 20 μm, and the average spectral emissivity (for wavelengths between 0.5 and 20 μm),

$$\bar{\varepsilon} = \frac{1}{N_{\varepsilon}} \cdot \sum_{\lambda=0.5\mu\text{m}}^{\lambda=20\mu\text{m}} \varepsilon_{\lambda} \tag{G-5}$$

where N_ε represents the number of spectral emissivity measurements between $\lambda = 0.5$ and 20 μm. Table 5-2 shows the response variables for the samples with different factor level combinations.

Factor	Si/Mn Ratio (A)	Cold-Rolling Reduction (B)	Pickling Time (s) (C)
Higher Level	(DP980) 0.45 (+)	53% (+)	180 (+)
Lower Level	(DP800) 0.05 (-)	1% (-)	120 (-)

Table 5-1: Factors and their respective levels used in the 2^3 model.

Sample	Factor Levels			Response Variables							
	A	B	C	Cav. %	$\bar{\varepsilon}$	$\varepsilon_{\lambda=1.6}$	$\varepsilon_{\lambda=2.1}$	$\varepsilon_{\lambda=2.4}$	$\varepsilon_{\lambda=5}$	$\varepsilon_{\lambda=10}$	$\varepsilon_{\lambda=20}$
(1)	-	-	-	38.186	0.684	0.655	0.595	0.566	0.417	0.364	0.279
a	+	-	-	51.829	0.700	0.628	0.580	0.559	0.460	0.433	0.375
b	-	+	-	19.266	0.513	0.437	0.380	0.350	0.238	0.159	0.104
ab	+	+	-	25.497	0.604	0.447	0.406	0.372	0.268	0.187	0.090
c	-	-	+	41.502	0.668	0.642	0.586	0.550	0.410	0.331	0.206
ac	+	-	+	50.640	0.652	0.557	0.504	0.474	0.325	0.244	0.148
bc	-	+	+	23.364	0.506	0.429	0.369	0.345	0.221	0.135	0.070
abc	+	+	+	12.761	0.427	0.355	0.289	0.265	0.158	0.097	0.052

Table 5-2: Eight samples with the three factors applied in different combinations, their respective cavity percentages, average emissivities (computed between $\lambda = 0.5 - 20$μm), and spectral emissivities at the select wavelengths are shown. All reported wavelengths are in μm.

Figure 5-6 shows optical micrographs of the eight samples in Table 5-2. Increasing the cold-rolling reduction percentage reduces the number of dark patches, which is consistent with the findings from Köpper et al. [51] and the hypothesis by Etzold et al. [52] and Ham et al. [43]. They suggest that the surface cavities formed during acid-pickling are flattened with cold-rolling, as discussed in Sec. 5.1 and Figure 5-1.

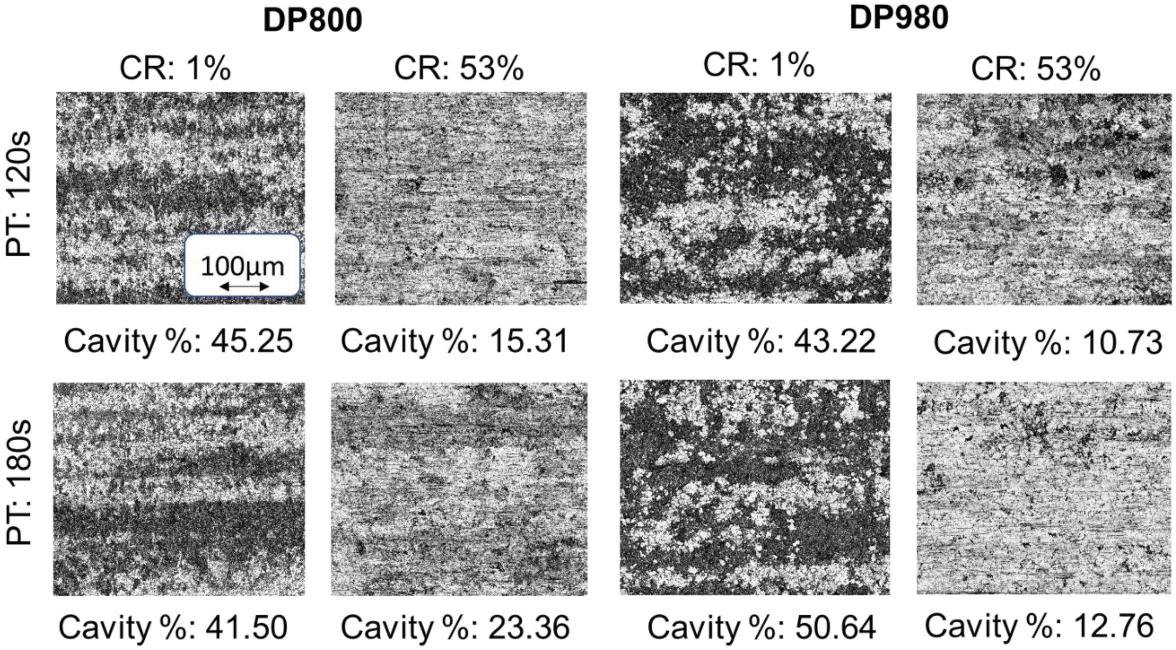

Figure 5-6: Optical micrographs of samples representing the 8 treatment combinations analysed through the 2^3 - factorial design. Fewer dark patches are observed as the cold-rolling reduction is increased from 1% to 53%.

The factor effects, their sum of squares and percentage contributions are computed for the response variables shown in Table 5-2. The full-factorial analysis computes a contrast for each factor by combining the response variable from the eight samples in Table 5-2 according to the algebraic signs shown in Table 5-3. For example, the contrast for factor A is,

$$C_{\mathrm{A}} = \mathrm{abc} + \mathrm{ac} + \mathrm{ab} + \mathrm{a} - (1) - \mathrm{b} - \mathrm{c} - \mathrm{bc}\,. \tag{5.2}$$

where the letters (a, b, c, abc, ac, ab, and bc) represent the response variables of interest for the eight samples with the different treatment combinations in Table 5-2 and Figure 5-6.

The contrast captures the response's change due to a change in the factor level. For a 2^3 - factorial design, the effect estimate is,

$$E_{\mathrm{A}} = \frac{1}{4 \cdot n} \cdot \left[C_A \right] \tag{5.3}$$

where *n* is the number of replicates at each treatment combination. The factor effects represent the change in the response variable for a change in the level of the factor averaged over the levels of the other factors. As discussed, due to physical and cost constraints, only a single replicate is available; therefore, $n = 1$.

Runs	**Factorial Effect**							
	I	A	B	AB	C	AC	BC	ABC
(1)	+	-	-	+	-	+	+	-
a	+	+	-	-	-	-	+	+
b	+	-	+	-	-	+	-	+
ab	+	+	+	+	-	-	-	-
c	+	-	-	+	+	-	-	+
ac	+	+	-	-	+	+	-	-
bc	+	-	+	-	+	-	+	-
abc	+	+	+	+	+	+	+	+

Table 5-3: Algebraic signs for combining the values of the response variables at the different treatment combinations (samples in Table 5-2) to compute the individual and combined factor effects.

The contrasts are then used to compute the sum of squares (*SS*) for each factor,

$$SS_{\mathrm{A}} = \frac{\left(C_{\mathrm{A}}\right)^2}{8 \cdot n} \tag{5.4}$$

Table 5-4 presents the results for the response variables of cavity percentage, average spectral emissivity and spectral emissivities at select wavelengths between 0.5 and 20 µm. Figure 5-7 then shows the percentage contribution by each factor to the response variable, computed by dividing the sum of squares for each effect by the total sum of squares. The book by Montgomery [53] provides more information about the technique.

Cavity Percentage				
Factor	**Effect**	**Contrast**	**SS**	**% Contr.**
A	4.602	18.409	42.363	2.802
B	-25.317	-101.268	1281.893	84.775
AB	-6.788	-27.152	92.154	6.094
C	-1.628	-6.511	5.299	0.350
AC	-5.335	-21.339	56.921	3.764
BC	-2.691	-10.766	14.488	0.958
ABC	-3.082	-12.327	18.994	1.256
Total			1512.112	

$\bar{\varepsilon}$				
Factor	**Effect**	**Contrast**	**SS**	**% Contr.**
A	0.003	0.011	0.000	0.023
B	-0.163	-0.653	0.053	75.754
AB	0.003	0.011	0.000	0.023
C	-0.062	-0.248	0.008	10.950
AC	-0.051	-0.203	0.005	7.312
BC	-0.030	-0.120	0.002	2.562
ABC	-0.034	-0.138	0.002	3.377
Total			0.070	

ε_λ **(1.6µm)**				
Factor	**Effect**	**Contrast**	**SS**	**% Contr.**
A	-0.044	-0.176	0.004	4.117
B	-0.203	-0.814	0.083	88.240
AB	0.012	0.050	0.000	0.330
C	-0.046	-0.184	0.004	4.511
AC	-0.035	-0.142	0.003	2.678
BC	-0.004	-0.016	0.000	0.035
ABC	-0.006	-0.026	0.000	0.089
Total			0.094	

ε_λ **(2.1µm)**				
Factor	**Effect**	**Contrast**	**SS**	**% Contr.**
A	-0.038	-0.152	0.003	2.953
B	-0.205	-0.822	0.084	86.756
AB	0.011	0.042	0.000	0.230
C	-0.053	-0.211	0.006	5.725
AC	-0.044	-0.174	0.004	3.905
BC	-0.011	-0.043	0.000	0.235
ABC	-0.010	-0.039	0.000	0.196
Total			0.097	

ε_{λ} (2.4µm)				
Factor	**Effect**	**Contrast**	**SS**	**% Contr.**
A	-0.035	-0.140	0.002	2.564
B	-0.204	-0.817	0.083	87.526
AB	0.006	0.025	0.000	0.083
C	-0.053	-0.212	0.006	5.906
AC	-0.042	-0.169	0.004	3.761
BC	-0.003	-0.011	0.000	0.017
ABC	-0.008	-0.033	0.000	0.142
Total			0.095	
ε_{λ} (5µm)				
Factor	**Effect**	**Contrast**	**SS**	**% Contr.**
A	-0.019	-0.074	0.001	0.842
B	-0.182	-0.727	0.066	80.432
AB	0.002	0.009	0.000	0.012
C	-0.067	-0.270	0.009	11.081
AC	-0.055	-0.221	0.006	7.395
BC	0.004	0.016	0.000	0.037
ABC	0.009	0.036	0.000	0.200
Total			0.082	
ε_{λ} (10µm)				
Factor	**Effect**	**Contrast**	**SS**	**% Contr.**
A	-0.007	-0.029	0.000	0.102
B	-0.198	-0.793	0.079	77.311
AB	0.002	0.007	0.000	0.006
C	-0.084	-0.337	0.014	13.971
AC	-0.056	-0.224	0.006	6.186
BC	0.027	0.107	0.001	1.418
ABC	0.023	0.090	0.001	1.006
Total			0.102	
ε_{λ} (20µm)				
Factor	**Effect**	**Contrast**	**SS**	**% Contr.**
A	0.001	0.006	0.000	0.005
B	-0.173	-0.693	0.060	66.345
AB	-0.018	-0.071	0.001	0.689
C	-0.093	-0.373	0.017	19.199
AC	-0.040	-0.158	0.003	3.457
BC	0.057	0.228	0.006	7.184
ABC	0.038	0.150	0.003	3.121
Total			0.090	

Table 5-4: Factor effects, their contrasts, and their sum of squares for each response variable. The percentage contributions of each factor have also been shown.

Figure 5-7 shows the percentage contribution of each factor to the response variables. The cold-rolling reduction percentage (factor B) has the most substantial effect on cavity percentage, the average spectral emissivity, and the spectral emissivities at all analysed wavelengths of interest. The similarities of the factor contributions for cavity percentage and the emissivities show that the surface cavities strongly dominate the radiative properties after removing the hot-rolling oxides.

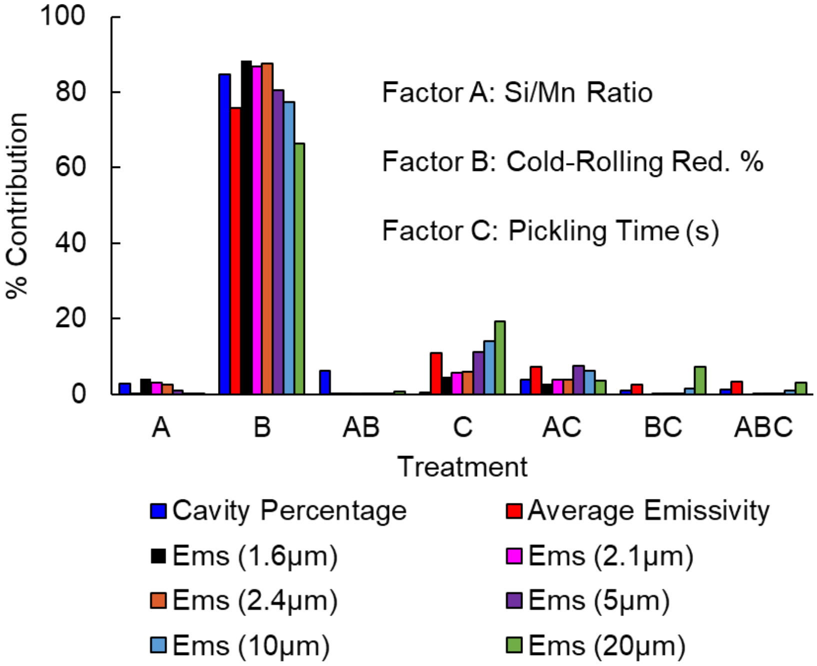

Figure 5-7: Percentage contributions of the processing parameters on the response variables. At all wavelengths, the cold-rolling reduction percentage strongly dominates the radiative properties.

In dual- or multi-replicate factorial designs, the statistical significance of each factor can be identified within a confidence interval through an analysis of variance (ANOVA). However, in a single replicate design as performed here, no intra-treatment error estimate exists. As such, Daniel [54] suggests a heuristic alternative of examining the factor effects shown in Table 5-4 for each response variable using normal probability plots, as shown in Figure 5-8.

The effects of the insignificant factors should behave like samples from a normal population with a mean of 0; as such, those effects will lie very close to the normal line. In contrast, statistically significant effects will behave as samples from a normal distribution with a non-zero mean; as such, they will be far from the normal line. The plots in Figure 5-8 show that the data point for cold-rolling reduction percentage lies far from the normal line for all response variables, suggesting that it strongly influences cavity percentage and strip spectral emissivity at all wavelengths of interest. As discussed earlier, the similarity between the effect of each factor on cavity percentage and emissivity highlights the impact of surface cavities on the overall radiative properties of the steel strip. On the other hand, the effect of acid pickling time, steel type, and all interaction effects have a negligible influence on the response variables.

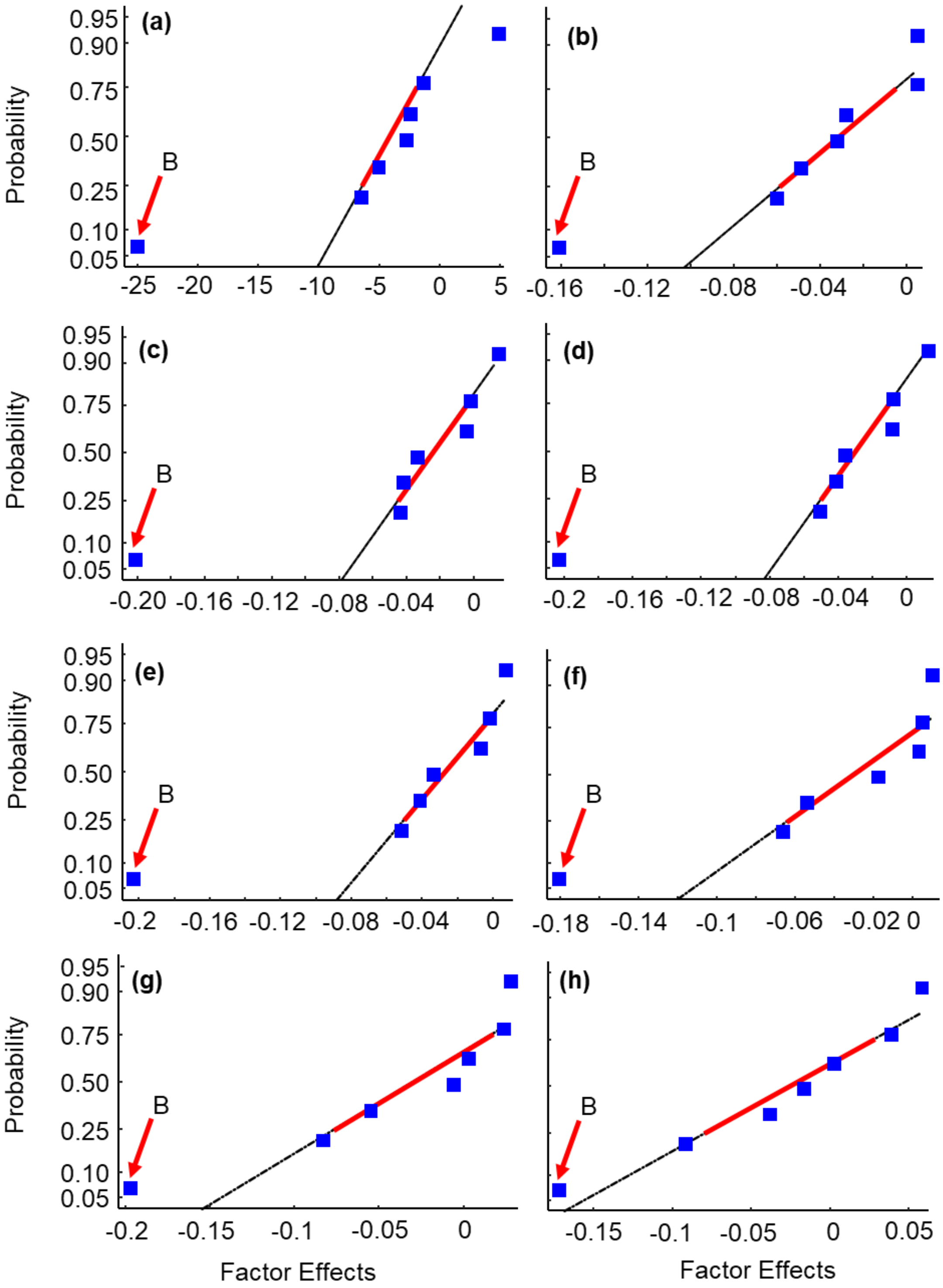

Figure 5-8: Normal probability plots of the effects of each factor on each response variable. All effects lie close to the normal line except for the cold-rolling reduction percentage. (a) Cavity Percentage, (b) average emissivity, spectral emissivities at (c) 1.6, (d) 2.1, (e) 2.4, (f) 5, (g) 10, and (h) 20 µm. The red arrow identifies the effect of the cold-rolling reduction percentage.

5.2.2. Effect of Cold-Rolling on Cavity Flattening

As such, this section proposes a simple single-factor regression model for surface cavity flattening as a function of the cold-rolling reduction percentage. Samples cold rolled to various extents (1%, 5%, 10%, 20% and 53%) are analysed, and samples of the two alloys (DP980 and DP800) pickled to various extents (120s, 150s, and 180s) are combined to yield six replicates at each cold-rolling reduction percentage. Figure 5-9 shows scatter plots of the response variables against cold-rolling reduction percentage for the six replicates overlayed with linear curve fits.

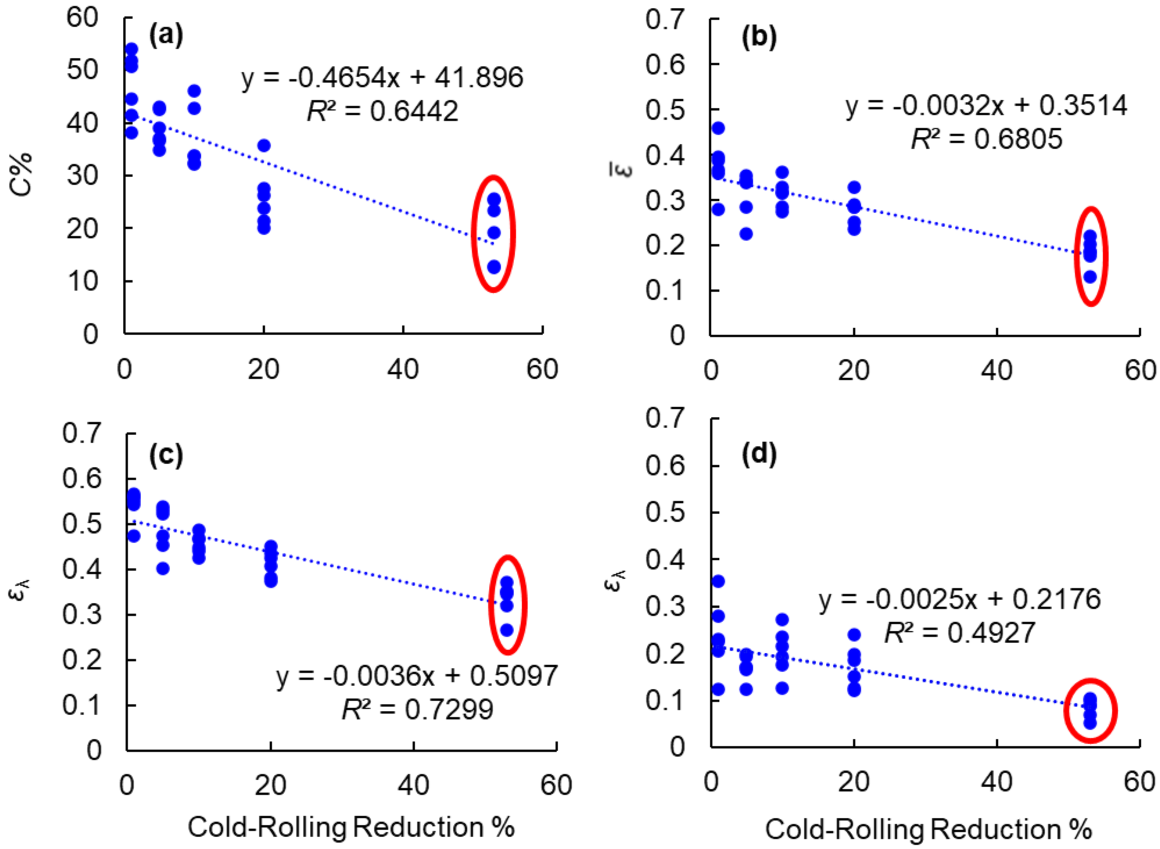

Figure 5-9: Scatter plots of cold-rolling reduction percentage against (a) cavity %, (b) average spectral emissivity, (c) spectral emissivity at λ = 2.4 µm and (d) spectral emissivity at λ = 20 µm. There are six replicates at each cold-rolling reduction value. Similar variations are observed in the number of surface cavities and radiative properties across the DP780 coil in Chapters 3 and 4, as shown by the red ovals.

The validity of the linear curve fits is then evaluated using residual analysis. Normal probability plots of the residuals of cavity percentage, average emissivity, and two select spectral emissivities at $\lambda = 2.4$ and $\lambda = 20$ μm are shown in Figure 5-6 (a), (b), (c) and (d), respectively. The residuals follow a Gaussian distribution identified by the normal probability plots and the various normality tests, as shown in Table 5-5. MATLAB® scripts developed in Ref. [55] are used for these tests.

Cavity Percentage			
Test	**Test Statistic**	**P-Value**	**Normal**
KS Limiting Form	0.8759	0.4268	✓
KS Stephens Modification	0.8991	0.0490	✗
KS Marsaglia Method	0.8759	0.3858	✓
KS Lilliefors Modification	0.1599	0.0486	✗
Anderson-Darling Test	0.6822	0.0496	✗
Cramer-Von Mises Test	0.1209	0.0584	✓
Shapiro-Wilk Test	0.9497	0.1663	✓
Shapiro-Francia Test	0.9576	0.2306	✓
Jarque-Bera Test	1.2079	0.5466	✓
D'Agostino & Pearson Test	2.0060	0.3668	✓
$\bar{\varepsilon}$			
Test	**Test Statistic**	**P-Value**	**Normal**
KS Limiting Form	1.1385	0.1496	✓
KS Stephens Modification	1.1687	0.0100	✗
KS Marsaglia Method	1.1385	0.1294	✓
KS Lilliefors Modification	0.2079	0.0019	✗
Anderson-Darling Test	0.7837	0.0318	✗
Cramer-Von Mises Test	0.1487	0.0248	✗
Shapiro-Wilk Test	0.9466	0.1372	✓
Shapiro-Francia Test	0.9321	0.0549	✓
Jarque-Bera Test	1.4357	0.4878	✓
D'Agostino & Pearson Test	2.655	0.2651	✓

ε_λ ($\lambda = 2.4\mu m$)			
Test	**Test Statistic**	**P-Value**	**Normal**
KS Limiting Form	0.7443	0.6367	✓
KS Stephens Modification	0.7641	0.1500	✓
KS Marsaglia Method	0.7443	0.5895	✓
KS Lilliefors Modification	0.1359	0.1650	✓
Anderson-Darling Test	0.4872	0.2243	✓
Cramer-Von Mises Test	0.0737	0.2504	✓
Shapiro-Wilk Test	0.9511	0.1814	✓
Shapiro-Francia Test	0.9610	0.2802	✓
Jarque-Bera Test	1.6292	0.4428	✓
D'Agostino & Pearson Test	2.7099	0.2580	✓
ε_λ ($\lambda = 20\mu m$)			
Test	**Test Statistic**	**P-Value**	**Normal**
KS Limiting Form	0.6172	0.8407	✓
KS Stephens Modification	0.6336	0.1500	✓
KS Marsaglia Method	0.6172	0.8004	✓
KS Lilliefors Modification	0.1127	0.2000	✓
Anderson-Darling Test	0.3802	0.4030	✓
Cramer-Von Mises Test	0.0597	0.3814	✓
Shapiro-Wilk Test	0.9643	0.3973	✓
Shapiro-Francia Test	0.9570	0.2232	✓
Jarque-Bera Test	2.9143	0.2329	✓
D'Agostino & Pearson Test	4.5539	0.1026	✓

Table 5-5: Testing of cavity percentage, average spectral emissivity and select (2.4μm and 20μm) spectral emissivity residuals for normality using various normality tests. Most tests identify the residuals for all response variables to be normal.

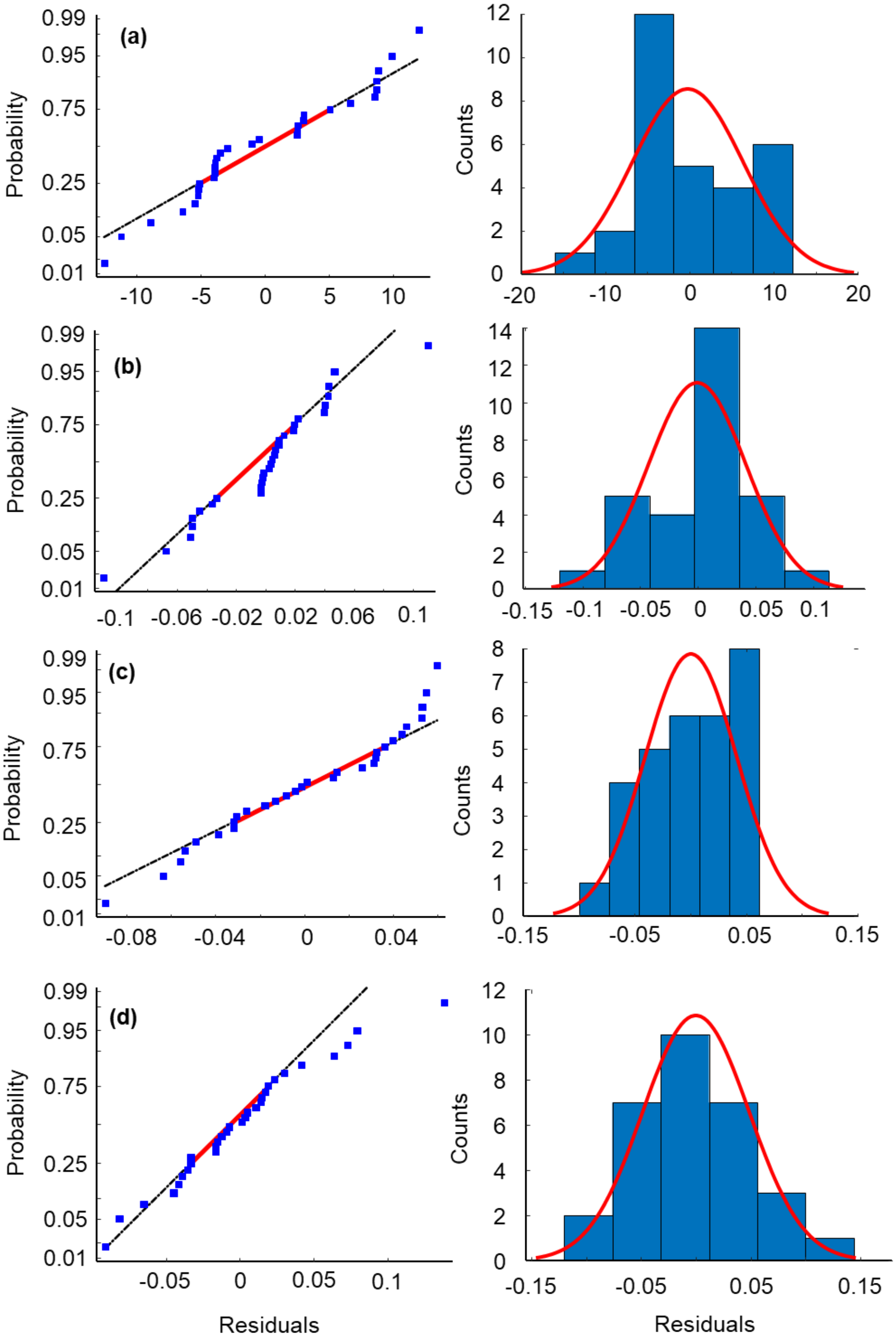

Figure 5-10: Normal probability and histograms for the residuals of (a) cavity percentage, (b) average spectral emissivity between 0.5 and 20µm, and spectral emissivities at (c) 2.4 and (d) 20µm.

The mostly normal residuals validate the linear regression models. This finding shows that the number of cavities on the strip surface and radiative properties are linearly proportional to the cold-rolling reduction percentage at all wavelengths across the spectrum. The minor heteroscedasticities in the plots may be attributed to small contributions by acid-pickling to the roughness of the surfaces after the oxides are entirely removed, slightly influencing the radiative properties. The impact of surface roughness outside the cavities is explored further in Chapter 6 using the neural network model.

Notably, even after cold-rolling to a reduction of ~53% (typical of industrial CGLs), an inherent random variability exists in cavity percentage (~10 – 30%). This variation causes the radiative properties of the steel strip to vary as much as 20%. Furthermore, the emissivities and the number of surface cavities between the edge and the middle of the coil show a similar difference (compare Figure 4-8 and Figure 5-9 – red ovals).

This finding suggests that other cold-rolling parameters (apart from thickness reduction %) may influence cavity flattening and vary across a single AHSS coil. Wiklund and Sandberg [56] suggest variations in cold-rolling pressure across the width of a single steel coil during cold-and temper-rolling processes due to the bending of the rollers. These variations may be responsible for the non-uniform flattening of cavities across a single coil. As such, a more detailed analysis of the cold-rolling process is necessary.

Köpper et al. [51] also hypothesised that the amount of grain-boundary oxidation might vary at different coil locations due to differences in the amount of oxygen infiltration when manufacturers wind the coil after hot-rolling. This analysis has studied samples from the mid-width and the tail of a hot-rolled coil; further work should also analyse samples from the edge-width and different locations along its axial length.

Due to these random variations, it is challenging to robustly model cavity formation and strip radiative properties based on the cold-rolling reduction alone. This issue is addressed in the following section through a data-driven machine learning model using an artificial neural network (ANN).

Chapter 6 : ANN Spectral Emissivity Model

Steelmakers continue to strive for finer strip temperature control during intercritial annealing; as such, reliable methods are required to predict strip radiative properties on CGLs. Given the random variability in surface topography, even after cold-rolling and acid-pickling to a specific extent, it becomes challenging to predict strip radiative properties using process parameters such as acid-pickling time and cold-rolling thickness reduction percentage alone.

Recently, there have been advances in on-line strip imaging technologies which can produce optical imagery and evaluate the surface topography parameters of a steel strip in real-time before it enters an annealing furnace. As such, physics-based or data-driven models correlating strip spectral emissivities with surface topography may allow steel manufacturers to generate *in-situ* spectral emissivity predictions for coil sections before they enter the annealing furnace.

Traditional methods for inferring strip radiative properties, such as the GOA ray-tracing algorithm and electromagnetic (EM), finite difference time domain (FDTD) models, are often computationally expensive and infeasible to implement on-line. Therefore, neural networks may serve as an excellent alternative for generating near-instantaneous spectral emissivity predictions on CGLs, by "front-loading" the computational burden to a one-time training phase. As such, this section explores using an artificial neural network (ANN) model to infer the radiative properties of AHSS using their surface topography parameters and optical microscope imagery.

However, a challenge with neural networks is their "black-box" nature which prevents the user from developing any physical insights into the problem. Therefore, this thesis performs a global sensitivity analysis (GSA) to model the functional dependencies of strip spectral emissivity on the sample's RMS roughness, R_q, surface slope, R_q/τ, and surface cavities. The ANN model developed in this chapter may be helpful with upcoming *in-situ* strip imaging technologies.

The following sections discuss the fundamentals of neural networks, their implementation for inferring the radiative properties of AHSS, and the use of GSA to infer the underlying physics of the problem.

6.1 Introduction to Neural Networks

Artificial neural networks (ANNs) have gained popularity in recent years in various disciplines such as engineering, the natural sciences, medicine, and commerce due to their ability to model the behaviour of complex physical systems and provide near-instantaneous predictions [57, 58, 59] after a one-time training on a dataset. These predictions are usually much faster and require less computation than physics-based simulations, such as finite difference time domain (FDTD) solutions for inferring surface reflectivity. Artificial neural networks are parallel computing devices loosely inspired by the highly interconnected nature of neurons in the human brain [57, 58, 59].

In regression applications, ANNs can map a set of input parameters $X = [x_1, x_2, x_3, \ldots x_n]$, to a set of outputs $Y = [y_1, y_2, y_3, \ldots, y_m]$, by developing an approximate function to model the underlying relationship between them. A common type of ANNs is multi-layer perceptrons (MLPs), consisting of an input layer, a set of hidden layers, and an output layer. The network layer outputs serve as the next layer's inputs. Information passes layer-to-layer until it reaches the output layer, producing the final prediction, Y' as shown in Figure 6-1.

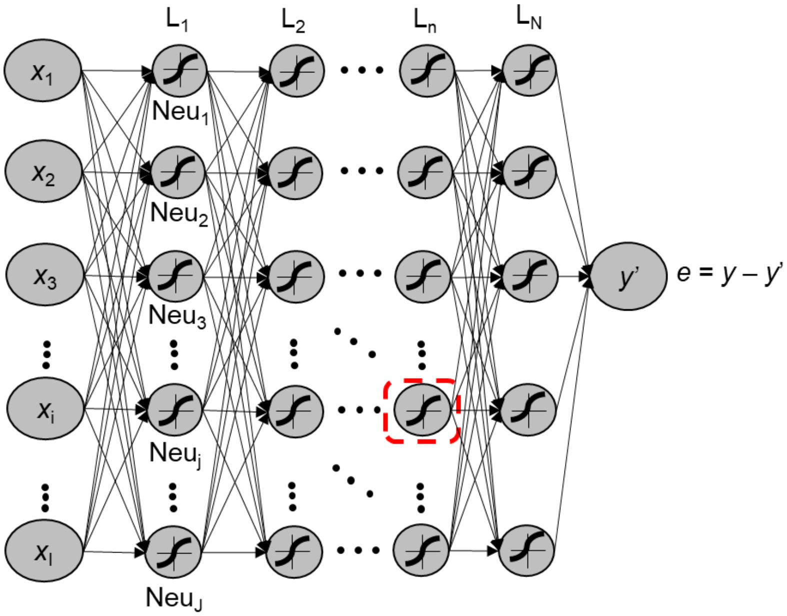

Figure 6-1: A multi-layer perceptron network (MLP) schematic with an input layer, a set of hidden layers, and an output layer. x, y and y' represent the inputs, outputs, and predicted values. e is the residual between y and y'. The neuron marked by the red-dashed box represents a hypothetical j^{th} neuron in the n^{th} layer.

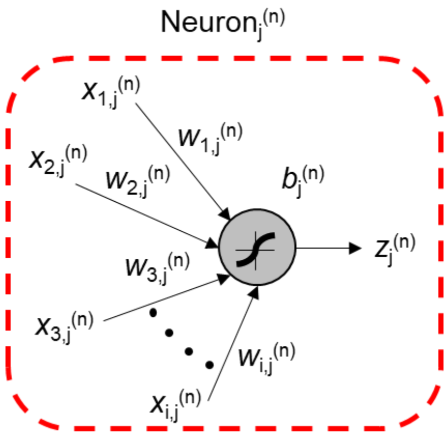

Figure 6-2: Computing the output of the jth neuron in the nth layer. This neuron is highlighted by the dotted red box in Figure 6-1.

The ith input to the jth neuron in layer n, $x_{i,j}^{(n)}$ is multiplied by a weight, $w_{i,j}^{(n)}$, which is unique to each input from the previous layer, and all $w_{i,j}^{(n)} \cdot x_{i,j}^{(n)}$ products are summed, to which is added a bias, $b_j^{(n)}$ (unique to the neuron in question), to compute the neuron's output. This relationship maps the output of a neuron to its inputs in a linear fashion. However, many physical systems are non-linear, and this method cannot model these non-linear relationships. Therefore, the linearly mapped output then goes through an activation function, ψ, to introduce non-linearity to the model,

$$z_j^{(n)} = \psi\left(\sum_{i=1}^{X} w_{i,j}^{(n)} \cdot x_{i,j}^{(n)} + b_j^{(n)}\right) \tag{6.1}$$

where $z_j^{(n)}$ is the output to the neuron, this work uses a tan-sigmoid activation function for all hidden neurons [60] and a linear activation function for the output neuron.

Countless studies have used ANNs to model the radiative properties of various systems and surfaces. For instance, Kang et al. [61] developed an ANN model to predict the radiative properties of mono-dispersed, spherical, packed beads of varying materials and geometries; they trained the network on results from Monte-Carlo simulations. Additionally, Sullivan et al. [62] designed a surrogate ANN model for predicting the radiative properties of patterned surfaces of varying materials and geometries. The authors trained the model on data from solutions to Maxwell's equations using finite-difference-time-domain (FDTD) simulations. Furthermore, Acosta et al. [63] recently proposed a neural network model for inferring the radiative properties of aluminium surfaces manufactured through Femtosecond Laser Surface Processing (FLSP) using manufacturing parameters and surface SEM imagery. As such, this section explores using ANNs to improve spectral directional emissivity predictions of AHSS by training on empirical data.

This chapter implements a regression ANN model to correlate the surface topography parameters of AHSS samples with their radiative properties to enable rapid spectral directional emissivity predictions. Such a model may also serve as an improvement to the linear regression model proposed by Lee [64] (at least for AHSS steels), which was found by Lin et al. [37] to perform poorly on highly rough AHSS surfaces. In addition, galvanisers may implement the proposed ANN with emerging online steel strip imaging technologies [65] for the *in-situ* characterisation of strip radiative properties after hot-rolling, acid-pickling and cold-rolling before the coil enters the annealing furnace.

6.1.1. ANN Training Procedure

One may choose optimum weights and biases through a supervised training procedure. During training, the algorithm initialises the weights to small random numbers, usually between 0 and 0.5, and sets the biases to zero. Their values are optimised iteratively through an optimisation procedure using training and validation datasets. The validation dataset is merely used to test the network's performance and not to update the network parameters, where the training and validation datasets consist of known input and output pairs. The neural network uses the inputs from the training set to generate predictions, and the training procedure tests the network's performance using those predictions through a cost function. Here, the mean-squared-error (MSE),

$$MSE = \frac{1}{N \cdot Y} \sum_{\mathrm{p}=1}^{N} \sum_{\mathrm{M}=1}^{Y} \left(\hat{y}_{\mathrm{p,M}} - y_{\mathrm{p,M}} \right)^2 \tag{6.2}$$

where N is the number of samples, Y is the number of outputs, $\hat{y}_{\mathrm{p,M}}$ is the predicted value, and $y_{\mathrm{p,M}}$ is the ground-truth output. This procedure is known as forward propagation. Subsequently, the effect of a marginal change in each weight and bias on the overall cost function is computed through a chain rule of partial derivatives, known as backpropagation. A minimisation algorithm then iterates the weights and biases; this work uses the Levenberg-Marquardt (LMA) algorithm (see Appendix D) [66]. Additionally, MATLAB® also has an in-built function for the straightforward and seamless implementation of LMA for neural networks.

For training, all inputs are rescaled between zero and one to improve convergence, while the outputs are naturally between zero and one as they are spectral emissivities. In this study, the ANN model applies at a specific wavelength, and it generates a single output which is the spectral emissivity of the strip surface at that wavelength (see Sec. 6.2). An entire training cycle through all data points in the training set is known as an epoch of training. Supervised training algorithms use the MSEs on the training and validation datasets to evaluate the model's performance after each epoch.

If the MSE on the validation dataset is higher at the k^{th} epoch compared to the $(k-1)^{th}$ epoch, and if this has been true for the last n number of epochs (this work uses MATLAB®'s default values of $n = 6$), the algorithm terminates training and saves the optimum weights and biases. This check prevents convergence to a local minimum. Figure 6-3 shows an example training run where at epochs greater than seven, the neural network is being over-fitted to the data, while at epochs less than seven, the network is being under-fitted. The optimum weights and biases yield the lowest error on the validation dataset.

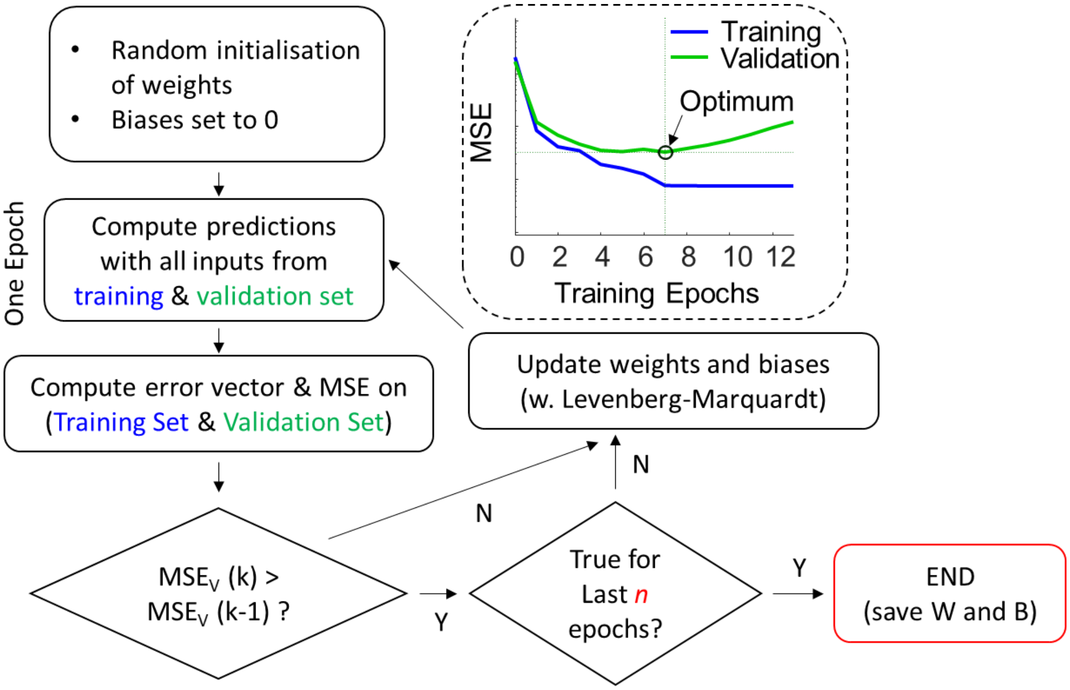

Figure 6-3: ANN training flow to optimise the weights and biases. The value for n is set to MATLAB®'s default value of 6. An example training process is also shown where the lowest error on the validation dataset is achieved at the seventh epoch.

6.2 ANN Regression Model for Spectral Emissivity Predictions

This work proposes the following ANN model to infer the radiative properties of AHSS coils in their cold-rolled condition, which applies at a specific wavelength. The inputs to ANN are chosen as dimensionless groups to capture the pertinent physical phenomena that may influence the spectral emissivity of the steel, as shown in Figure 6-4.

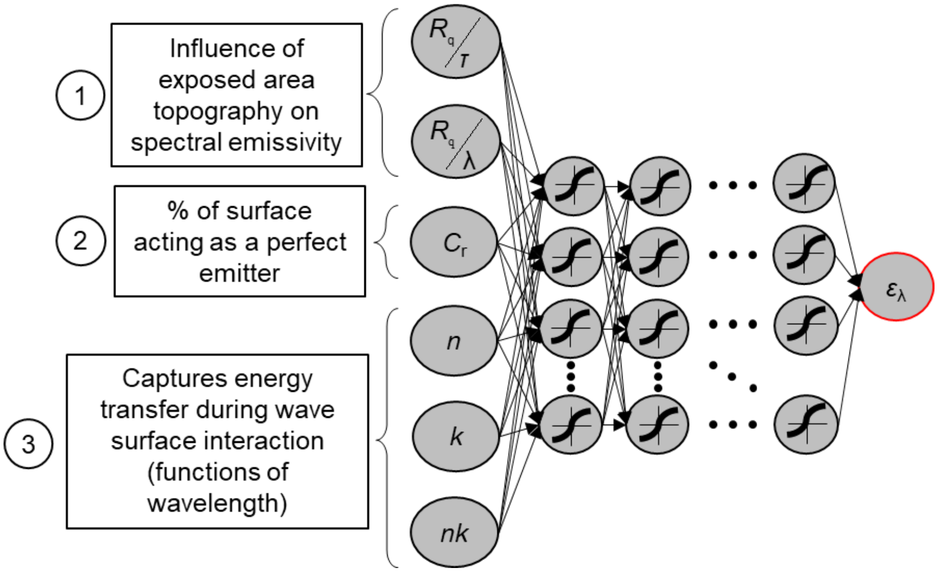

Figure 6-4: Proposed ANN model for inferring the spectral emissivities of AHSS in their cold-rolled condition before entering the annealing furnace.

The points below discuss the physical phenomena captured by each input:

1) The surface slope, R_q/τ and the wavelength-normalised RMS roughness, R_q/λ (inferred using depth mapping on the Keyence optical microscope), capture how the surface topography of the exposed area (outside the cavities) influences the spectral emissivity through scattering and wave diffraction effects, respectively [18, 37, 48, 49, 50, 67]. Roughness artefacts outside the cavities should primarily influence the spectral emissivity at the shorter wavelengths through scattering and at the longer wavelengths through EM diffraction effects.
2) The cavity ratio, C_r found through image thresholding, captures the percentage of the surface assumed to be a perfect emitter of EM radiation. These cavities should influence the spectral emissivity at most wavelengths of interest. This assumption is validated later through a sensitivity analysis.

3) The optical constants of the substrate metal, ‘*n*’ and ‘*k*’, define how the wave interacts with the charge carriers within the surface. The imaginary permittivity $\epsilon_{\mathrm{im}} = 2 \cdot n \cdot k$ (i.e., the interaction effect between *n* and *k*) significantly affects the energy absorbed by the surface due to ray attenuation [68]. When an electromagnetic ray impinges on an opaque conducting material like metal, the beam penetrates the substrate or is reflected. The imaginary permittivity influences the energy attenuation of the penetrated ray as it travels through the material interacting with the charge carriers within the substrate. These charge carriers are free electrons of the substrate material, which oscillate due to the absorbed energy. Therefore, the attenuation of the penetrated ray and, in turn, the imaginary permittivity strongly dictates the metal’s emissivity. As discussed, the optical constants for specific AHSS alloys are challenging to obtain. Therefore, the optical properties of pure iron are used in this study [38, 39], as discussed in Sec. 4.3.

Consider two simple, feedforward ANN models with one layer and one neuron (see Figure 4). In computing the output, z_i, the model may struggle to capture the interaction between *n* and *k* if the ANN does not receive their product as an input, where the weight, w_3, can be adjusted during training to model the impact of the imaginary permittivity, 2*nk*. Here, ψ is the activation function (this study uses the tan-sigmoid function), and *b* represents the bias unique to the neuron. Even more extensive networks with more layers and neurons follow a similar process to compute the output, which may lead to the omission of specific interaction effects without carefully selected inputs.

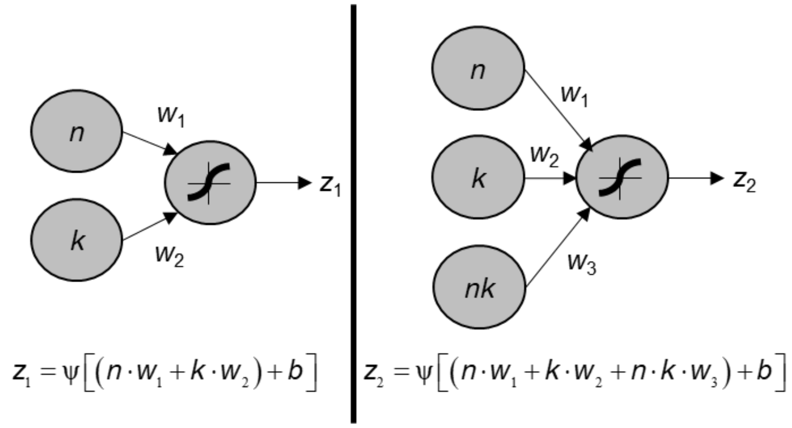

$$z_1 = \psi\left[\left(n \cdot w_1 + k \cdot w_2\right) + b\right]$$

$$z_2 = \psi\left[\left(n \cdot w_1 + k \cdot w_2 + n \cdot k \cdot w_3\right) + b\right]$$

Figure 6-5: Limitation of a neural network in modelling the interaction effect between two variables.

6.2.1 ANN Training Data

This work uses three sets of AHSS samples for training and testing the neural network: (1) 90 DP780 samples extracted from different locations on an industrially processed cold-rolled coil; (2) 44 DP980 samples extracted from a hot-rolled coil, then acid-pickled (for 45-180s) to various extents, and subsequently cold-rolled to a reduction of 53%; and (3) 15 DP800 and 15 DP980 samples extracted from a hot-rolled coil, and subsequently acid-pickled (for 120-180s) and cold-rolled (red. 1% to 53%) to various extents, yielding 164 samples in total. The under-pickled (45s) samples in dataset 2 do not show reflectivity behaviour like the oxidised samples in Figure 5-4, possibly due to extensive cold-rolling (~53% red.) leading to the flattening of oxide nodules as discussed in Sec. 5.1.

The training procedure uses samples in datasets 2 and 3 for training and samples in dataset 1 to test the trained network's performance. First, their spectral-directional emissivities and surface slopes are evaluated using the procedure discussed in Sec. 2.1 and Sec. 2.2. The *ex-situ* spectral directional emissivities of the samples are initially analysed using the procedure described in Sec. 3.2, between 0.5-20 μm. Figure 6-6 shows the obtained emissivity spectra for the three datasets. Next, the training procedure uses the samples which are acid-pickled and cold-rolled to various extents (datasets 2 and 3), to train the neural network; doing so captures the effect of the upstream processes (acid-pickling and cold-rolling) on the surface state and radiative properties of the steel. Lastly, the algorithm tests the trained model on the DP780 samples from dataset 1.

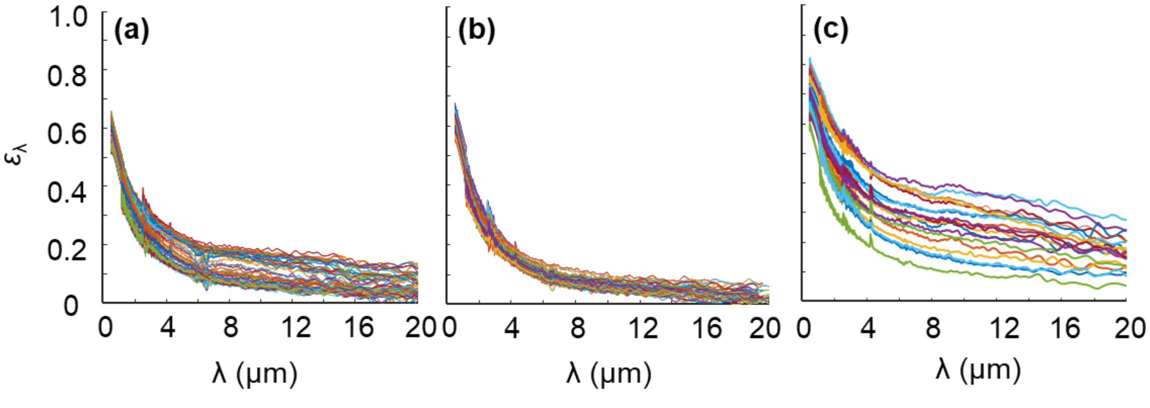

Figure 6-6: Spectral directional emissivities of all 164 samples. (a) Dataset 1, (b) dataset 2, (c) dataset 3. Samples from dataset 3 show the greatest variance in spectral emissivities, as those samples are acid-pickled and cold-rolled to various extents.

According to the procedure described in Sec. 4.2.1, the Keyence VHX-5000 optical microscope generates digitised surface height maps through depth mapping. The height maps can then be used to compute the RMS surface roughness, R_q and the surface slope, R_q/τ. However, the optical microscope cannot image the cavity interior due to trapped visible light, causing the cavities to appear as dark patches. The surface replication technique proposed in Sec. 4.3.1 may be used; however, it would be highly time-consuming to apply to all 164 samples, nor is it suitable for an on-line application, which is one of the goals of this research.

As such, this work assumes that the surface cavities act as perfect emitters at most wavelengths of interest between 0.5 and 20 μm. Therefore, the neural network uses the percentage cavity coverage of the surface as one of the inputs. A global sensitivity analysis then shows the validity of this assumption. The thresholding procedure described in Sec. 4.2.1. is used for cavity quantification. Figure 6-7 shows surface optical imagery from datasets 1, 2, and 3, where the surface cavities appear as dark patches.

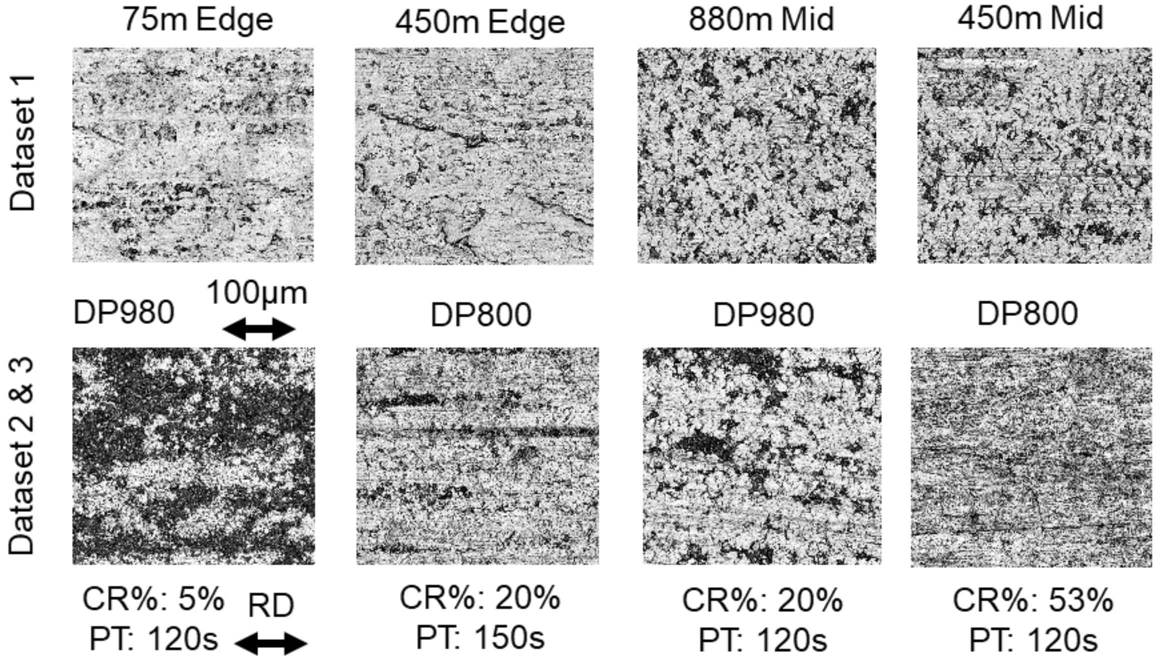

Figure 6-7: Optical micrographs showing varying amounts of surface cavitation amongst the samples analysed from datasets 1, 2 and 3. The reported lengths (75m, 450m and 880m) for samples from dataset 1 represent the axial location along the length of the DP780 coil.

The large variability in surface topography and radiative property parameters amongst the training samples (datasets 2 and 3) allows for the proper training of the regression ANN. Testing of the network on samples from different locations on an industrially processed coil (dataset 1) then mimics how galvanisers may use this model in the industry.

6.2.2 Optimising the Network Topology

This work implements a grid search approach to find the optimum number of hidden neurons and layers. This procedure trains the ANN 100 times for each neuron and layer combination to account for the variance in network performance. Figure 6-8 shows how the MSE on the testing dataset changes as the number of hidden layers and neurons are varied. A single hidden layer can approximate most physical systems [69]; however, adding a second layer has been shown to improve network performance for certain datasets [70]. For this dataset, however, the addition of a second layer shows a deterioration in performance, which can be attributed to overfitting; as such, a single layer with five hidden neurons is chosen.

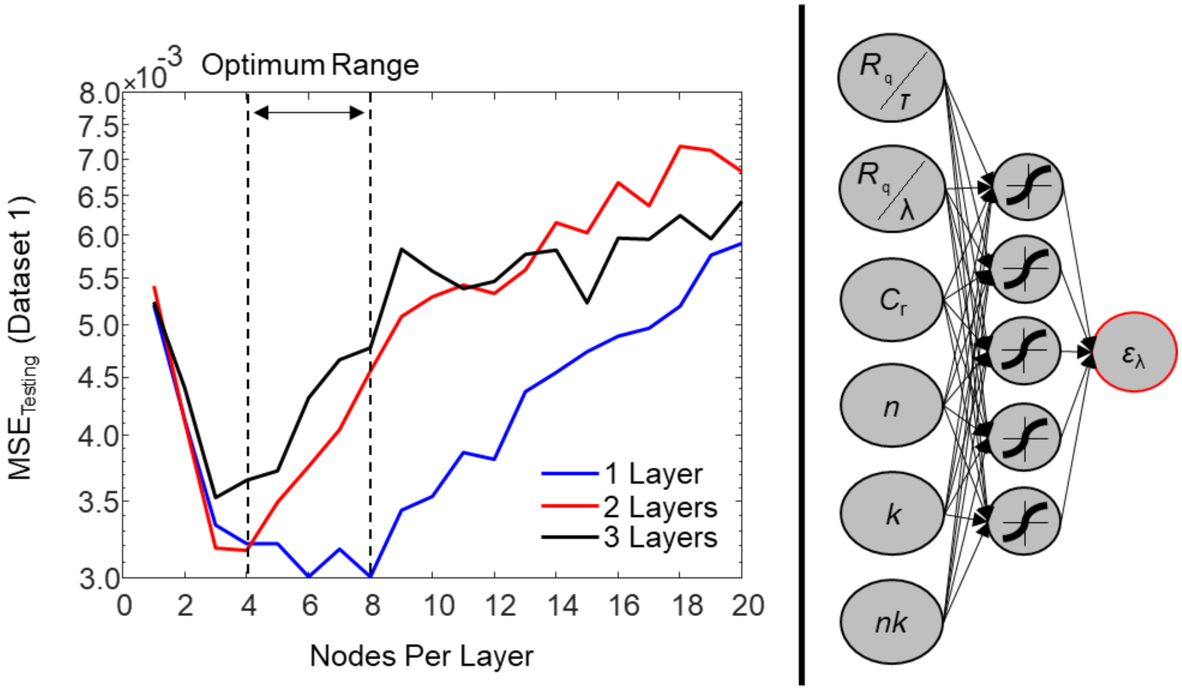

Figure 6-8: Choosing optimum number of hidden neurons and layers through a grid-search approach. A single hidden layer with five neurons yields the lowest error on the testing dataset. As such, a single hidden layer with five neurons is chosen.

6.2.3 ANN Model Results

Figure 6-9 compares the ANN spectral emissivity predictions for samples extracted from various locations on the DP780 coil in dataset 1 with their respective measured values. The selected network topology in Figure 6-10 generates accurate predictions, demonstrating the feasibility of using ANNs for near-instantaneous pre-annealed AHSS spectral emissivity predictions. The neural network predictions are also compared with emissivities obtained by running a geometric optics approximation (GOA) [18, 37] ray-tracing simulation with the digitised surface height maps as boundary conditions. However, the digitised height maps do not contain information regarding the topography inside the cavities; hence the GOA model generates inaccurate predictions for surfaces with many cavities. As such, the neural network model proposed here can be an excellent alternative for near-instantaneous spectral emissivity predictions when implemented with on-line strip imaging tools [65].

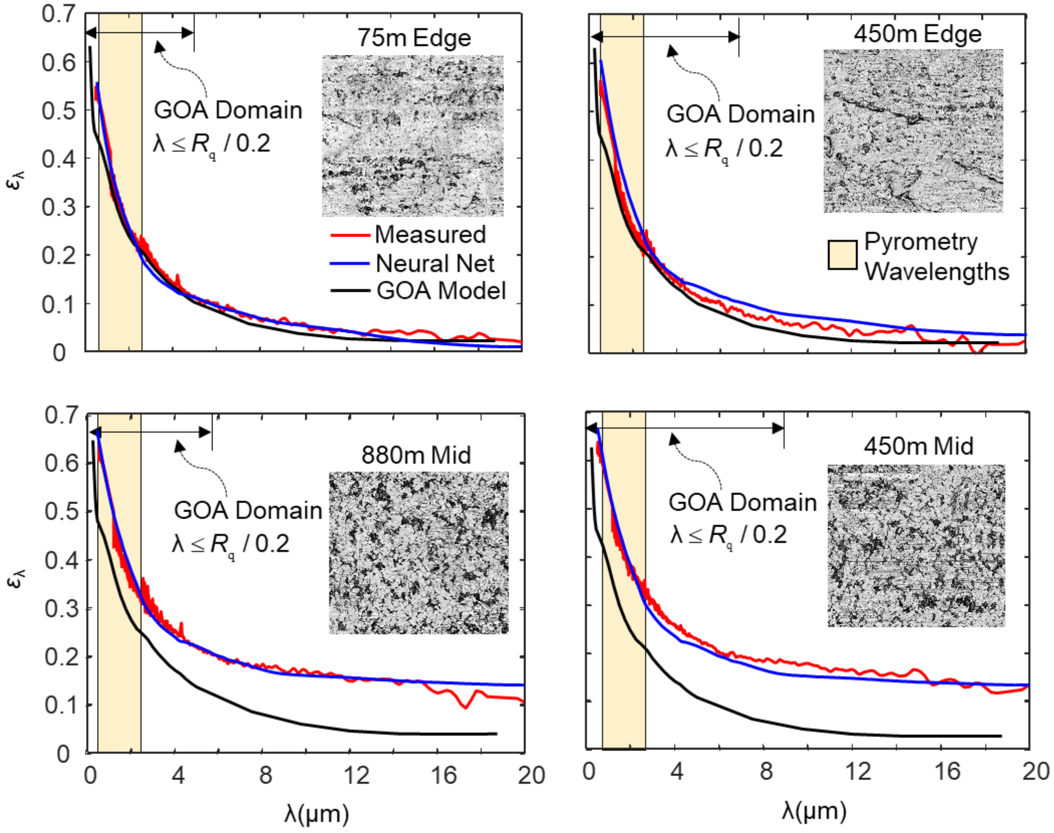

Figure 6-9: Comparison of neural network predictions and the measured spectral emissivities. Predictions from GOA simulations are also presented. Unfortunately, the GOA predictions for surfaces with many cavities are poor as the topography inside the cavities is not captured by optical microscope.

Furthermore, Figure 6-10 shows a residual analysis comparing the ANN predictions with the measured emissivity values for samples in the testing dataset (dataset 1). The residuals are mostly normal, with a skewness at the tail. This result demonstrates the validity of the ANN model and confirms that the input parameters and the ANN model capture the physics of the problem accurately.

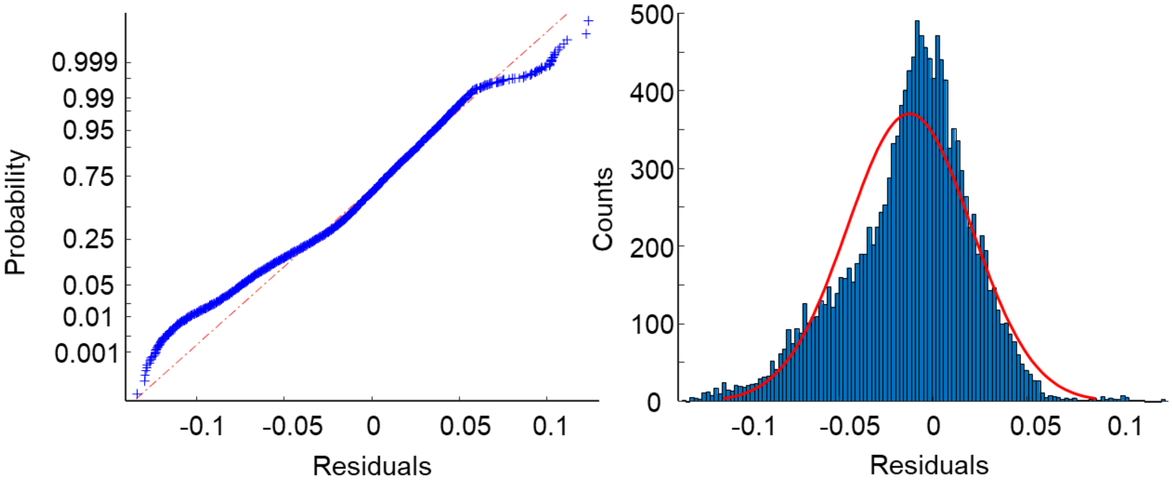

Figure 6-10: Residual analysis of all samples in the testing dataset (dataset 1), the mostly normal residuals signify the validity of the ANN model.

This section shows that the ANN model generates accurate spectral emissivity predictions for the samples analysed in this thesis with an accuracy of approximately ±5%. However, a challenge with neural networks is their inability to provide insight into the physics of the problem; therefore, they are known as “black-box” models. The following section addresses this issue through a global sensitivity (GSA) analysis.

6.3 Global Sensitivity Analysis for ANN Inputs

The "black box" nature of ANNs is a significant drawback, which prevents the user from developing any physical insights into the underlying problem. As such, this work implements a global sensitivity analysis (GSA) to model the functional dependencies of the output spectral emissivity on the inputs of the neural network. For example, Eghtesad et al. [71] recently implemented an ANN model to infer the radiative properties of porous media using the material's geometric and optical features.

They then implemented a sensitivity analysis to quantify the influence of a factor on the output by removing it as an input and evaluating the change in model performance. This work uses the Fourier amplitude sensitivity test (FAST) instead to compute sensitivity indices for each input parameter, allowing the user to infer the impact of each input simultaneously. These indices range between zero and one and quantify each input's variance contribution to the output's total variance.

Practitioners commonly use FAST due to its ease of implementation in contrast to more rigorous Monte-Carlo approaches like the SOBOL technique [72, 73] and its compatibility with non-linear and non-monotonic models [74, 75]. Various studies have employed the FAST technique, including studying the importance of process parameters in the catalytic conversion of chlorofluorocarbons (CFCs) [76] and evaluating factors affecting greenhouse gas emissions in the transportation sector [77]. This thesis implements the method to determine the effect of each surface topography parameter on strip radiative properties.

6.3.1 Fourier Amplitude Sensitivity Testing

The traditional FAST method explores the influence of each parameter on the output of a computational model (in this case, the ANN),

$$Y = f\left(x_1, x_2, ..., x_r\right) \tag{6.3}$$

by exploring the parameter space of all inputs $\Omega_n = (X \in x_{i,\min} < x_i < x_{i,\max};\ i = 1, 2, 3, \ldots r)$. The parameter space, Ω_n, is explored by simultaneously oscillating each parameter between $x_{i,\min}$ and $x_{i,\max}$ at distinct integer frequencies ω_i, [72,73]. The procedure samples each input parameter according to its marginal cumulative distribution function. Xu and Gertner [74] and Saltelli et al. [78] suggest the following sampling function:

$$x_{\mathrm{i}} = F_{\mathrm{i}}^{-1}\left(\mathrm{prob}_{\mathrm{i}}\right) = F_{\mathrm{i}}^{-1}\left(0.5 + \frac{1}{\pi}\cdot\sin^{-1}\left(\sin\left(\omega_{\mathrm{i}}\cdot s\right)\right)\right) \tag{6.4}$$

where s is known as the common parameter and is varied between $-\pi$ and π, and F_{i} is the marginal cumulative distribution function of the variable x_{i}. This sampling function explores all regions of the parameter space, Ω_{n}, equally and acts as a transformation between the s and x domains (Ref. [78] provides further details on this technique).

The computational model, $f(s)$, is then expanded as a Fourier series,

$$f\left(x_1, x_2, x_3, \ldots, x_{\mathrm{r}}\right) = f\left(s\right) = A_0 + \sum_{p=1}^{\infty}\left\{A_p\cdot\cos\left(p\cdot s\right) + B_p\cdot\sin\left(p\cdot s\right)\right\} \tag{6.5}$$

where

$$A_0 = \frac{1}{2\pi}\cdot\int_{-\pi}^{\pi} f\left(s\right)\mathrm{d}s \tag{6.6}$$

$$A_p = \frac{1}{\pi}\cdot\int_{-\pi}^{\pi} f\left(s\right)\cdot\cos\left(s\cdot p\right)\mathrm{d}s \tag{6.7}$$

and

$$B_p = \frac{1}{\pi}\cdot\int_{-\pi}^{\pi} f\left(s\right)\cdot\sin\left(s\cdot p\right)\mathrm{d}s \tag{6.8}$$

are the analytical Fourier coefficients. The variance, V, of function, $f(\mathrm{s})$, is expressed as,

$$V = \mathrm{E}\left[f\left(\mathrm{s}\right)^2\right] - \left[\mathrm{E}\left\{f\left(\mathrm{s}\right)\right\}\right]^2 \tag{6.9}$$

where E represents the expected value. Substituting Eq. (6.5) into Eq. (6.9) gives the total variance (see Appendix E for complete derivation),

$$V = \frac{1}{2}\sum_{p=1}^{\infty}\left(A_p^2 + B_p^2\right) \tag{6.10}$$

where $\Lambda_p = ½\left(A_p^2 + B_p^2\right)$ is known as the spectrum. The variance contribution, V_{i}, of the distinct i^{th} integer frequency, ω_i, to the output is equivalent to the variance contribution to the output by the i^{th} input parameter, x_{i}. Therefore, the sensitivity index for the i^{th} input is given by,

$$\sigma_{\mathrm{i}} = \frac{V_{\mathrm{i}}}{V} = \frac{\frac{1}{2}\cdot\sum_{p=1}^{\infty}(A_{p\omega_{\mathrm{i}}}^{2} + B_{p\omega_{\mathrm{i}}}^{2})}{\frac{1}{2}\cdot\sum_{p=1}^{\infty}\left(A_{p}^{2} + B_{p}^{2}\right)} \tag{6.11}$$

where *p* represents the analytical Fourier term [74, 75]. The Fourier sensitivity index is analogous to a first-order SOBOL sensitivity index and a main effect in a full-factorial design [74]. As such, the sensitivity index of the product of two inputs represents their first-order interaction. This method quantifies the interaction effect of *n* and *k* (i.e., the influence of the imaginary permittivity ϵ_{im}).

6.3.2 Numerical Implementation

For a real-world numerical solution, Xu and Gertner [74] generate a total of *N* common parameters,

$$\mathbf{s} = \left\{s_{1}, s_{2}, s_{3}, \ldots s_{\mathrm{j}}, \ldots, s_{N}\right\} \tag{6.12}$$

$$s_{j} = -\pi + \frac{\pi}{N} + \left(\frac{2\cdot\pi}{N}\right)\cdot\left(j-1\right) \tag{6.13}$$

where *s* is varied between -π and π. Using the assigned integer frequencies, ω_{i} and Eq. (6.4), they generate a set of $x_{\mathrm{i,j}}$'s to form a matrix,

$$\mathbf{X} = \begin{bmatrix} x_{1,1} & \cdot & \cdot & x_{1,r} \\ \cdot & \cdot & \cdot & \cdot \\ \cdot & \cdot & \cdot & \cdot \\ x_{N,1} & \cdot & \cdot & x_{N,r} \end{bmatrix}_{N\mathrm{x}r} \tag{6.14}$$

whose jth row serves as an input to function $f(s_{\mathrm{j}})$, where *N* represents the number of samples and *r* represents the number of input parameters to model *f*, which is evaluated as,

$$\begin{gathered} Y\text{=}\left\{f\left(s_{1}\right), f\left(s_{2}\right), \ldots f\left(s_{\mathrm{N}}\right)\right\} = \\ \left\{f\left(x_{1,1}, x_{1,2}, \ldots x_{1,r}\right), f\left(x_{2,1}, x_{2,2}, \ldots x_{2,r}\right), f\left(x_{3,1}, x_{3,2}, \ldots x_{1,r}\right), \ldots f\left(x_{N,1}, x_{N,2}, \ldots x_{N,r}\right)\right\}. \end{gathered} \tag{6.15}$$

The discrete method expresses the Fourier coefficients as,

$$A_p = \frac{2}{N}\sum_{\mathrm{j}=1}^{N} f\left(s_{\mathrm{j}}\right)\cdot\cos\left(s_{\mathrm{j}}\cdot p\right), B_p = \frac{2}{N}\sum_{\mathrm{j}=1}^{N} f\left(s_{\mathrm{j}}\right)\cdot\sin\left(s_{\mathrm{j}}\cdot p\right) \tag{6.16}$$

where p is the numerical Fourier term and the sensitivity indices for all inputs x_{i} is computed as follows,

$$\sigma_{\mathrm{i}} = \frac{V_{\mathrm{i}}}{V} = \frac{\frac{1}{2}\cdot\sum_{p=1}^{\frac{N-1}{2\cdot\omega_{\max}}}\left(A^2_{p\omega_i} + B^2_{p\omega_i}\right)}{\frac{1}{2}\cdot\sum_{p=1}^{\frac{N-1}{2}}\left(A_p^2 + B_p^2\right)}. \tag{6.17}$$

Xu and Gertner [74] and Saltelli et al. [78] state that the minimum number of numerical Fourier terms should be (N-1)/2, and (N-1)/(2$\omega_{\max}$) for computing V and V_{i} respectively, according to the Nyquist critical frequency, to capture the influence of all the integer frequencies in set $\boldsymbol{\omega}$ and their higher harmonics.

Various studies choose the set of integer frequencies, $\boldsymbol{\omega} = \{\omega_1, \omega_2, \omega_3, \ldots, \omega_r\}$ to be linearly independent to ensure that interference effects are minimised [74, 78, 79]. For instance, if $\omega_1 = a\omega_2$, where a is an integer, interference may arise when computing V_1 and V_2 through Eq. (6.17). Furthermore, when sampling input values from their respective marginal inverse CDFs through Equation (6.4), using a linearly independent frequency set allows for an even exploration of each input's probability space, as shown in Figure 6-11.

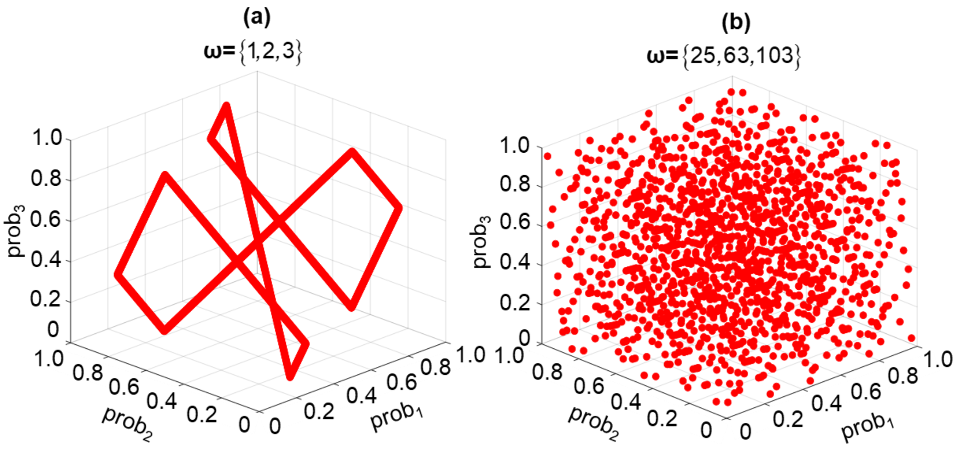

Figure 6-11: Exploration of the probability space of each input for a hypothetical model with three input parameters when sampling through Eq. (41), using (a) linearly dependent and (b) independent frequency sets.

Cukier et al. [79] suggest that a set of frequencies are linearly independent if

$$\sum_{\mathrm{i}=1}^{\mathrm{r}} a_{\mathrm{i}} \cdot \omega_{\mathrm{i}} \neq 0, \sum_{\mathrm{i}=1}^{\mathrm{r}} |a_{\mathrm{i}}| \leq M+1 \tag{6.18}$$

where a_{i} can take any integer, and M represents the number of harmonics of the fundamental frequency, ω_{i}. Usually, in the FAST algorithm, frequencies are set to be free of interference up to the fourth or sixth order (i.e., $M = 4$ or $M = 6$) [74]. As such, Cukier et al. [79] used a trial-and-error procedure to compute interference-free frequency sets that satisfy Eq. (6.18) for several inputs ranging from two to ten for $M = 4$. This thesis uses a frequency set developed by Cukier et al. [79] for six inputs: $\boldsymbol{\omega} = \{25,63,103,135,157,177\}$, with an order of $M = 4$. Saltelli et al. [78] generated at least

$$N = 2M\omega_{\mathbf{max}} + 1 \tag{6.19}$$

samples using Eq. (6.4) and (6.13), to avoid aliasing effects. Through Eq. (6.19), with $\omega_{\mathrm{max}} = 177$ in the set, $\boldsymbol{\omega}$, 1417 samples are used.

6.3.3. Accounting for Correlated Inputs

The non-dimensional input groups to the ANN are combinations of the RMS roughness, wavelength, correlation length, cavity ratio, and the optical constants of the substrate material. Therefore, correlations may exist amongst these non-dimensional groups; however, the traditional FAST technique is limited to independent inputs [74, 75]. As such, this work implements the FAST-C technique proposed by Xu and Gertner [74], an extension of the traditional FAST approach for correlated inputs.

In the FAST-C approach, the inputs, **X**, are found using Eq. (6.4), similarly to the traditional FAST technique, but are subsequently reordered to introduce the correlation structure amongst them using the Iman and Conover [80] procedure (see Appendix G). Here, the input parameters are sampled from their marginal distributions (F_{i}) estimated by fitting non-parametric kernel distributions using MATLAB®'s *fitdist* and *ksdensity* functions (see Appendix F) to data in datasets 1, 2 and 3. Non-parametric distributions are chosen to avoid making assumptions regarding the data distribution.

The Iman and Conover procedure takes the input matrix **X**, together with a required Pearson rank correlation matrix **C**, and returns a matrix **W** (a permuted version of **X**), which has the same rank correlation structure as **C**. Figure 7 shows the true correlation structure **C** amongst the non-dimensional inputs inferred from datasets, 1, 2, and 3 (see Figure 6-12 (a)), the correlation structure amongst the input parameters **X**, independently generated through Eq. (6.4) (Figure 6-12 (b)), and lastly, the correlation structure of the values in **W**, after reordering **X** with the Iman and Conover [80] procedure, which is close to **C** (Figure 6-12 (c)).

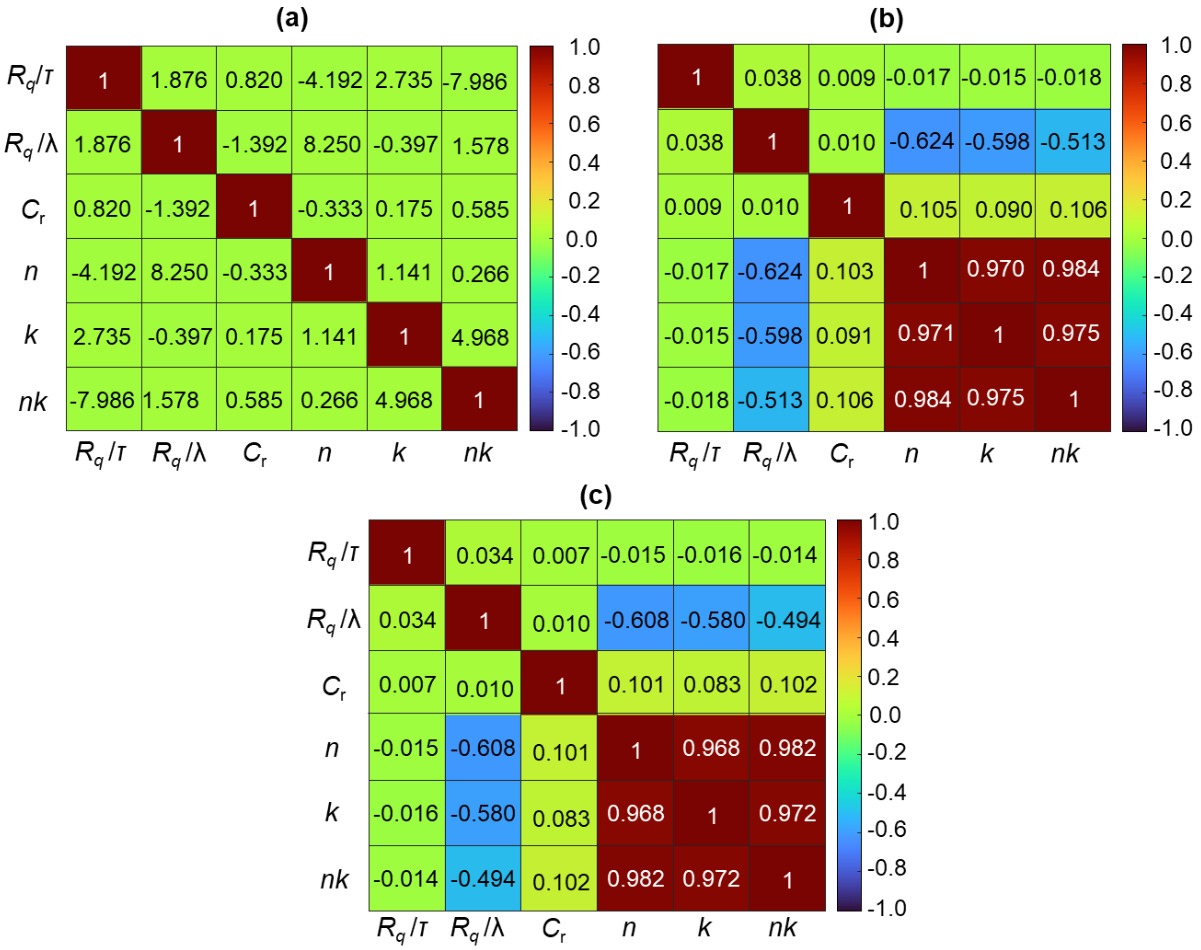

(a)

	R_q/τ	R_q/λ	C_r	n	k	nk
R_q/τ	1	1.876	0.820	-4.192	2.735	-7.986
R_q/λ	1.876	1	-1.392	8.250	-0.397	1.578
C_r	0.820	-1.392	1	-0.333	0.175	0.585
n	-4.192	8.250	-0.333	1	1.141	0.266
k	2.735	-0.397	0.175	1.141	1	4.968
nk	-7.986	1.578	0.585	0.266	4.968	1

(b)

	R_q/τ	R_q/λ	C_r	n	k	nk
R_q/τ	1	0.038	0.009	-0.017	-0.015	-0.018
R_q/λ	0.038	1	0.010	-0.624	-0.598	-0.513
C_r	0.009	0.010	1	0.105	0.090	0.106
n	-0.017	-0.624	0.103	1	0.970	0.984
k	-0.015	-0.598	0.091	0.971	1	0.975
nk	-0.018	-0.513	0.106	0.984	0.975	1

(c)

	R_q/τ	R_q/λ	C_r	n	k	nk
R_q/τ	1	0.034	0.007	-0.015	-0.016	-0.014
R_q/λ	0.034	1	0.010	-0.608	-0.580	-0.494
C_r	0.007	0.010	1	0.101	0.083	0.102
n	-0.015	-0.608	0.101	1	0.968	0.982
k	-0.016	-0.580	0.083	0.968	1	0.972
nk	-0.014	-0.494	0.102	0.982	0.972	1

Figure 6-12: Pearson rank correlation structures of (a) experimental data from datasets 1, 2, and 3, (b) samples generated using Eq. (6.4) (x10^{-5}), and (c) FAST-C samples after Iman and Conover restructuring.

A correlation exists amongst the wavelength-normalised RMS roughness, the optical properties *n* and *k* of the substrate and *nk* as they are functions of wavelength. However, the correlation between the surface slope, R_q/τ and the wavelength-normalised roughness, R_q/λ is not very strong; this indicates that the surface slopes are driven more strongly by the correlation lengths, τ, and to a lesser extent by RMS roughness. Two surfaces with the same RMS roughness can have drastically different surface slopes due to differences in their correlation lengths, as shown in Figure 6-13. The poor correlation among the cavity ratio, the surface slope, and wavelength-normalised RMS roughness highlights that the microscope cannot infer the topography within the cavities. The roughness parameters, therefore, represent the exposed area topography outside the cavities.

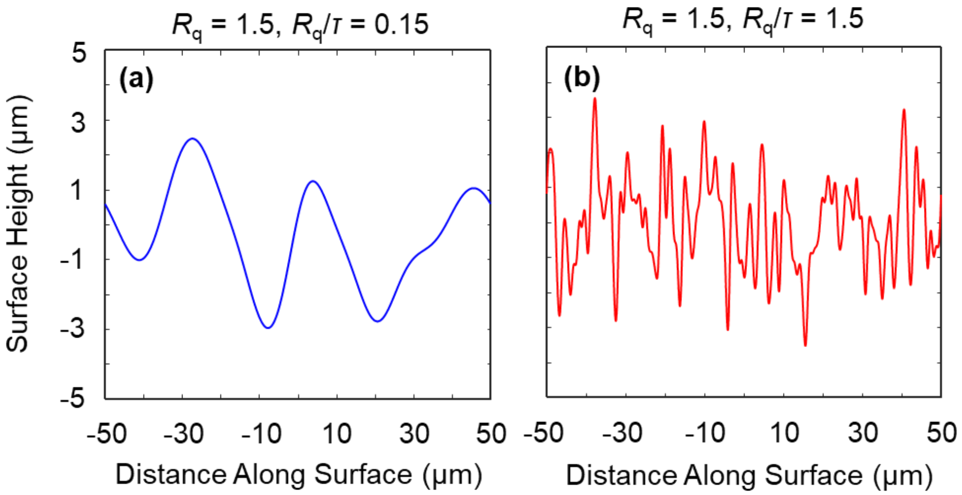

Figure 6-13: Two hypothetical surfaces with the same RMS roughness but with drastically different surface slopes due to differences in their correlation lengths.

This method then uses the restructured samples in **W** to compute the overall variance, *V*, across all samples using the denominator in Eq. (6.17) by evaluating *f*(**s**) (the ANN) on data in **W**. The values in **W** are scaled between zero and one as required for the ANN using minimum and maximum values for the parameters from datasets 1, 2, and 3. However, introducing the correlation structure after the reordering process alters the original sampling order and hence the characteristic oscillation frequency of each input, as shown in Figure 6-14 [74] for the refractive index, *n*.

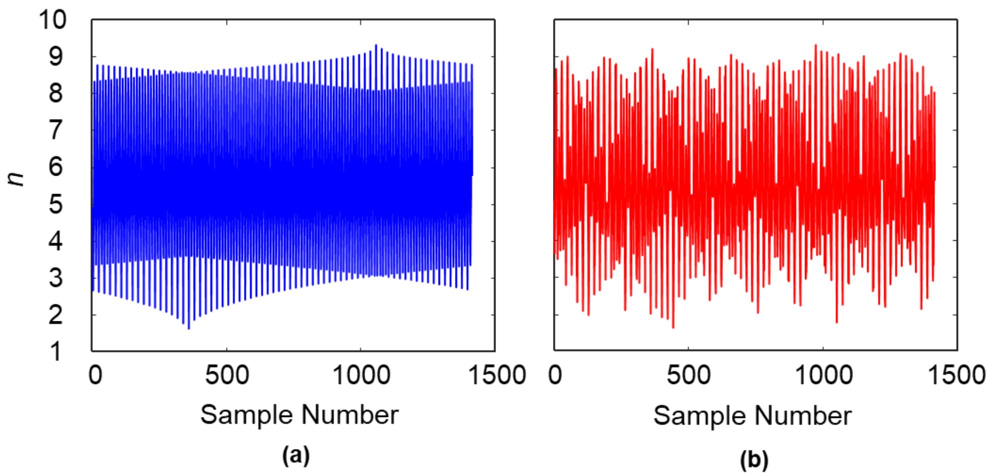

Figure 6-14: (a) Original and (b) altered oscillation frequencies for the refractive index (n) after restructuring using the Iman and Conover [80] procedure.

The samples in the input x_i's respective column are returned to the original order (i.e., the order before restructuring) to compute the variance contribution of a given input. Simultaneously, the entries in the other columns are set to the corresponding values from matrix **W**. Doing so ensures that the original oscillation frequency is restored for each input while maintaining the correlation structure. As such, each characteristic frequency also contains information regarding the correlation among the input parameters. The results are saved as a matrix, $\mathbf{XW}_i$, yielding r $\mathbf{XW}_i$ matrices, as illustrated in Figure 6-15. The sensitivity indices, σ_i, for each input, x_i, are then computed, where the neural network is evaluated on the entries in the jth row in the corresponding $\mathbf{XW}_i$ matrix to compute $f(s_j)$.

X

I1	I2	I3	I4	I5
1	1	1	1	1
2	2	2	2	2
3	3	3	3	3
4	4	4	4	4
5	5	5	5	5

W

I1	I2	I3	I4	I5
2	3	5	1	4
3	2	3	5	1
1	4	4	2	5
4	1	2	4	6
5	5	1	3	7

XW_2

I1	I2	I3	I4	I5
4	1	2	4	6
3	2	3	5	1
2	3	5	1	4
1	4	4	2	5
5	5	1	3	7

XW_4

I1	I2	I3	I4	I5
2	3	5	1	4
1	4	4	2	5
5	5	1	3	7
4	1	2	4	6
3	2	3	5	1

Figure 6-15: Example showing the restoration of the characteristic oscillation behaviour for a given input i. Here, XW_i examples are given for the hypothetical inputs 2 and 4.

6.3.4. Overall Sensitivity Indices

In this study, the FAST-C algorithm is written in MATLAB® and subsequently validated on an analytical problem from Xu and Gertner [74], after which it is used to compute the sensitivity indices for the ANN model. Figure 6-16 (a) and (b) show sensitivity indices for the six non-dimensional input groups using the FAST and FAST-C techniques.

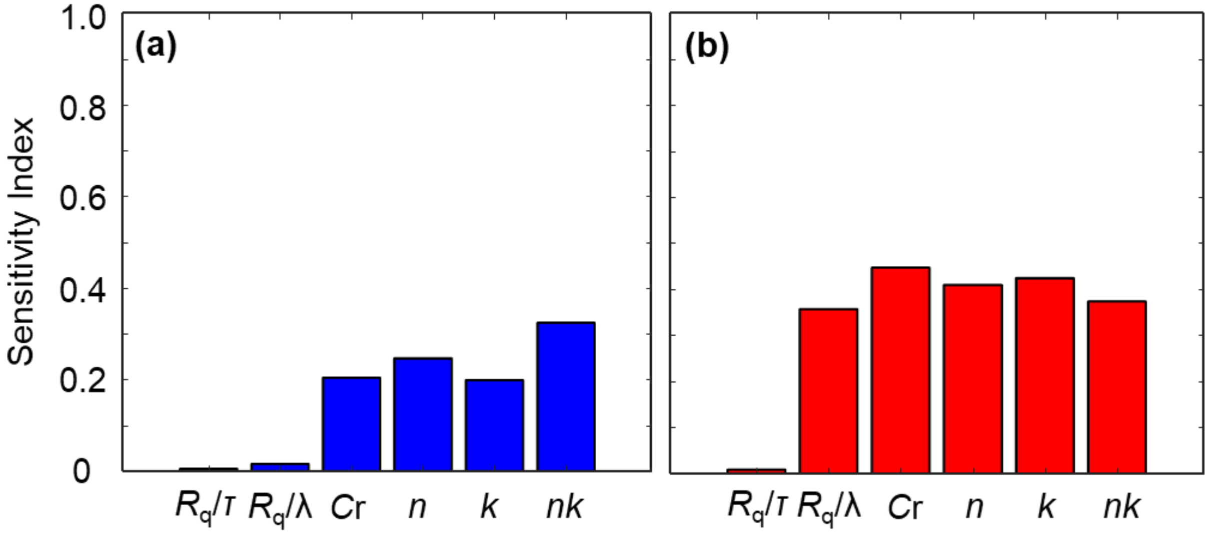

Figure 6-16: Overall sensitivity indices for non-dimensional input parameter groups; (a) assumes that that the non-dimensional groups are independent, while (b) accounts for the correlation structure amongst the inputs shown in Figure 6-12 (c).

The plots in Figure 6-16 highlight the importance of accounting for the correlation structure amongst the non-dimensional input groups, which leads to a change in their sensitivity indices. The strong correlation among the optical constants *n* and *k*, the wavelength-normalised RMS roughness, and the product *nk* increase their impact on spectral emissivity. Furthermore, the high sensitivity index of input *nk* highlights the interaction effect between *n* and *k* on spectral emissivity, which is representative of the imaginary permittivity, ϵ_{im} as discussed in Sec. 6.2 and Figure 6-4.

The optical constants *n* and *k*, their product *nk*, and the number of surface cavities show the most substantial effect on strip spectral emissivity. The surface slope of the exposed area shows a negligible sensitivity index. This finding suggests that the primarily smooth topography of the exposed surface area outside the cavities has a smaller overall influence on strip emissivity than the surface cavities.

The impact of the wavelength-normalised RMS roughness and surface slope outside the cavities can be visualised further by the overlaying their distributions (from samples in datasets 1,2 and 3) on the reflectivity regime map created by Tang et al. [49]. The wavelength-normalised RMS roughness differentiates between the EM, specular and GOA domains, while the mostly uniform low surface slopes do not influence the radiative properties, their sensitivity indices agree with this finding.

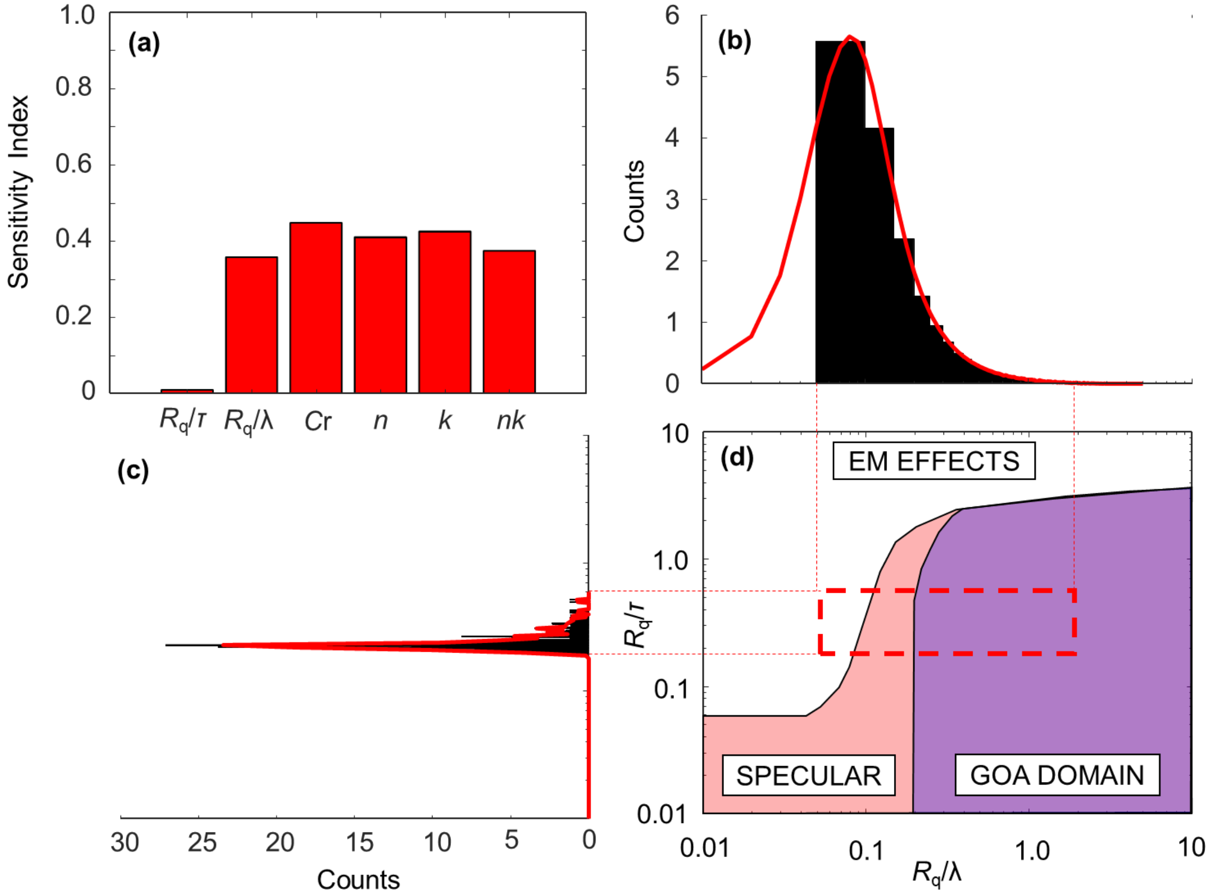

Figure 6-17: Sensitivity indices and distributions of the wavelength-normalised RMS roughness and surface slopes of the exposed area of samples analysed in datasets 1, 2, and 3, overlayed on the regime map by Tang et al. [49]. The wavelength-normalised RMS roughness differentiates between the EM, specular and GOA domains, as such has a higher sensitivity index compared to surface slope.

6.3.5. Wavelength Dependent Sensitivity Indices

This section evaluates the sensitivity indices for RMS roughness, surface slope and cavity percentage as functions of wavelength between 0.5 and 20 μm. For a given wavelength, the optical properties of the substrate are interpolated from a data table [38, 39]. The Iman and Conover technique [80] accounts for the correlation structure amongst the three variables as they are sampled in the FAST-C algorithm using distributions in Appendix F and Eq. (6.4). According to Cukier et al. [79], the integer frequency set, $\boldsymbol{\omega} = \{25,63,103\}$, is used. With $\omega_{\max} = 103$ and $M = 4$, 825 samples are generated according to Equation (6.19).

As shown in Figure 6-18 (a), the RMS roughness has the most potent effect at the shorter wavelengths where the surface is optically rough. The surface cavities influence the radiative properties equally at all wavelengths of interest, as they act as perfect emitters of EM radiation, and the surface slope has a negligible effect.

Tang et al. [49] and Fu and Hsu [81] pointed out that the surface slope strongly influences the number of scattering events and the amount of EM diffraction effects when the surface is optically rough and smooth (i.e., at shorter and longer wavelengths), respectively. Most samples in datasets 1, 2 and 3 have an exposed area surface slope of approximately 0.2 (see Appendix F and Figure 6-18 (a)), and Lin et al. [37] showed that the spectral reflectivities of smooth DP980 samples ($R_q/\tau < 0.3$) were very close to that of pure iron at all wavelengths between 0.5 and 20 μm. This finding suggests that the area outside the cavities shows few higher order scattering events and EM diffraction effects.

The surface slopes are then sampled from two hypothetical uniform distributions as shown in Figure 6-18 (b) and (c) (Case A: Min: 0.2, Max: 0.55, Case B: Min: 0.2, Max: 0.75) to explore the impact of larger surface slopes. Doing so increases the surface slope's sensitivity index, as shown in Figure 6-18 (b) and (c). For DP980 samples with slopes greater than ~0.4, Lin et al. [37] found that GOA predictions become inaccurate at longer wavelengths, suggesting the onset of EM diffraction phenomena. Furthermore, the GOA model accurately captures the radiative properties at shorter wavelengths for surfaces with slopes greater than ~0.4 μm; because, at the shorter wavelengths, higher-order scattering dominates the radiative properties. The results from case (c) should be treated with caution, however, as some of these slope values lie outside the training domain of the ANN model (> 0.50). Additional training using samples with larger surface slopes would be beneficial.

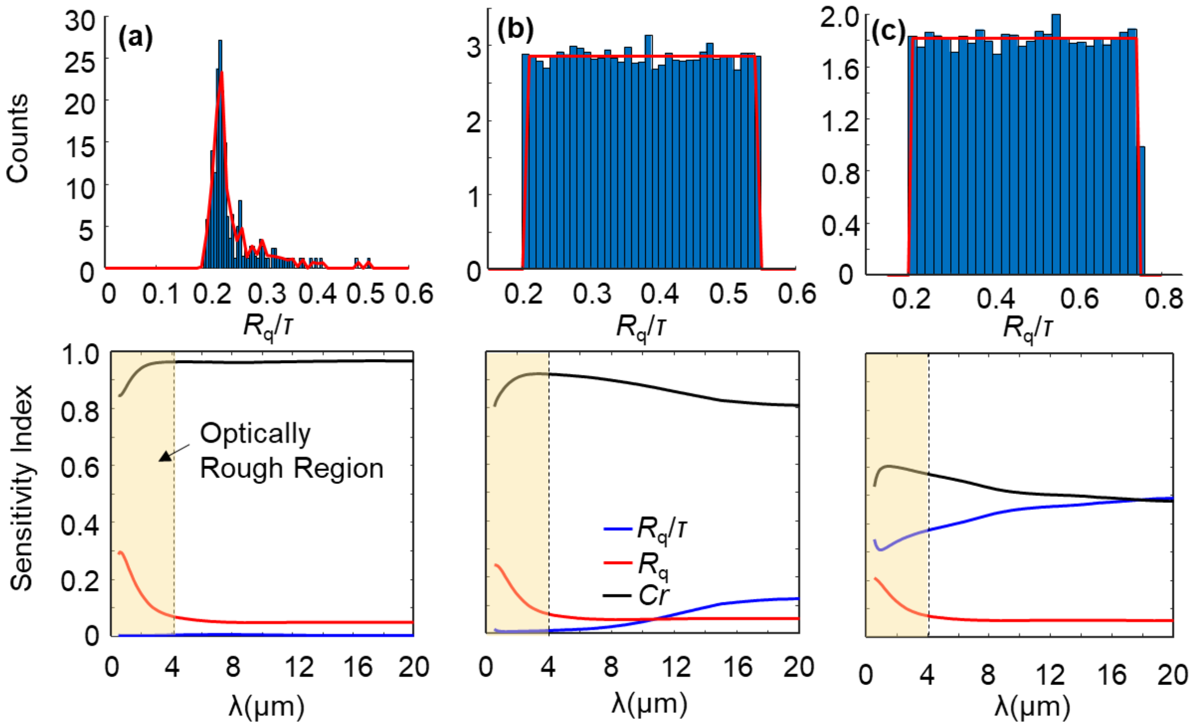

Figure 6-18: Impact of surface topography parameters on spectral emissivity at different wavelengths of incident light between 0.5 and 20 μm. The surface slope values are (a) sampled from the kernel distribution fit to data in datasets 1,2 and 3 (see Appendix C), (b) sampled from a uniform distribution with Min and Max values of 0.2 and 0.55, (c) sampled from a uniform distribution with Min and Max values of 0.2 and 0.75.

For the samples analysed in this work, the surface topography outside the cavities has a minor influence on spectral emissivity (Figure 6-18 (a)). However, when sampling the surface slope outside the cavities from broader distributions, the exposed area shows a more significant influence on spectral emissivity through higher-order scattering and EM diffraction, as evidenced by the increase in the sensitivity index of the surface slope. Furthermore, as the surface slope of the exposed area approaches the surface slope inside the cavities, as shown in Figure 4-12, the sensitivity indices of the surface slope and cavity ratio tend to converge (Figure 6-18 (c)). This increase in the surface slope sensitivity index suggests that the ANN starts to capture higher-order scattering and EM diffraction phenomena.

6.3.6 Validation of Cavity Blackbody Assumption with GOA

The GOA model is then used to validate the blackbody assumption for the cavities further. In these GOA runs, the model assumes the surface cavities to be blackbodies; therefore, any ray that intercepts them is fully absorbed. As in the earlier sections, the surface topography outside the cavities is inferred using depth mapping on the Keyence microscope. This approach improves the spectral emissivity predictions for cavity-rich samples, as shown for two select samples in Figure 6-19. This finding further validates the cavity ratio sensitivity indices shown in Figure 6-18 and conclusively proves that the surface cavities behave as perfect emitters at all wavelengths of interest. Furthermore, the ANN and the GOA models now generate similar spectral emissivity predictions.

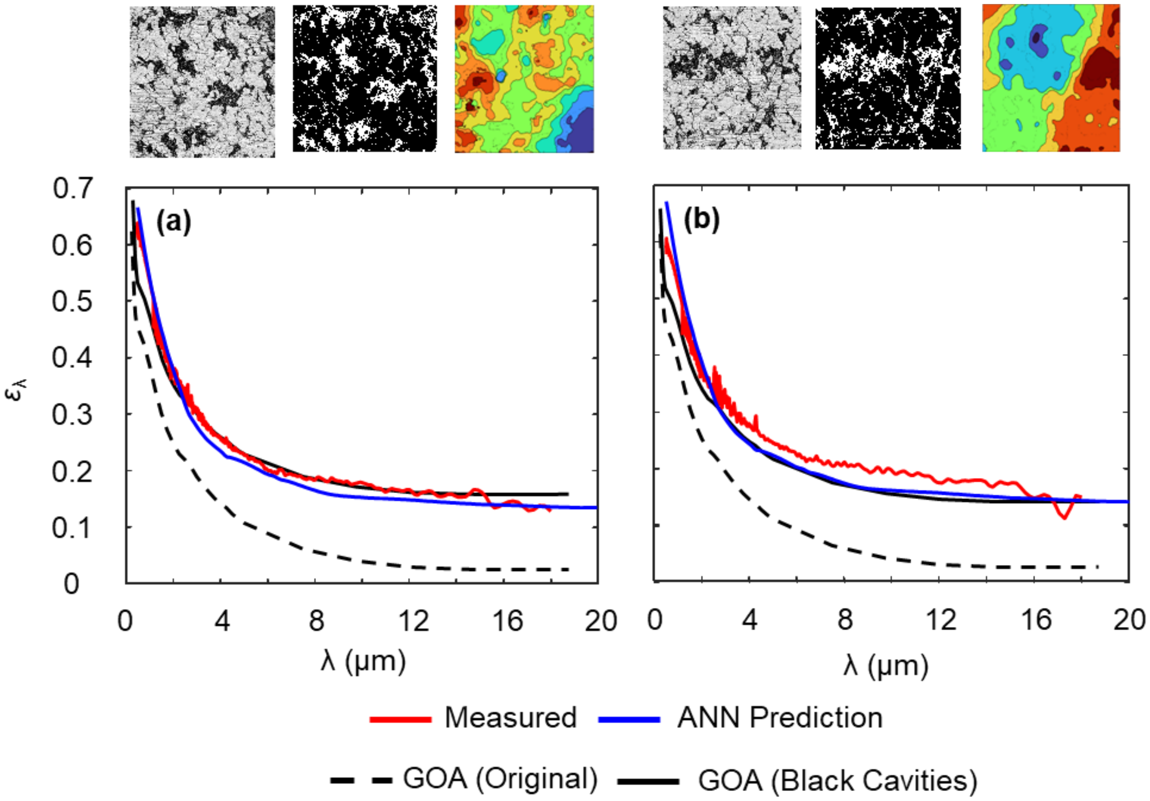

Figure 6-19: GOA spectral emissivity predictions by setting the areas covered by the cavities as blackbodies for two select samples with many cavities, (a) 450m Mid and (b) 880m Mid.

6.4 Prospective Application and Future Improvements

The previous section showed that an ANN model could be used effectively in a lab environment where the strip surface topography parameters and optical imagery are easily inferable. This section explores whether the ANN model can be implemented on an industrial line to infer the radiative properties of the steel before it enters the annealing furnace. This section also discusses prospective future improvements to the ANN model.

6.4.1 On-Line Implementation for In-Situ Spectral Emissivity Prediction

Recently, there have been advances in *in-situ* strip imaging technologies. Amepa Process Measurement Systems, for example, has developed a microscope capable of inferring the 3D topography and generating optical imagery of the steel strip surface at different coil locations [65]. The microscope can image different coil parts by moving along rails, as shown in Figure 6-20.

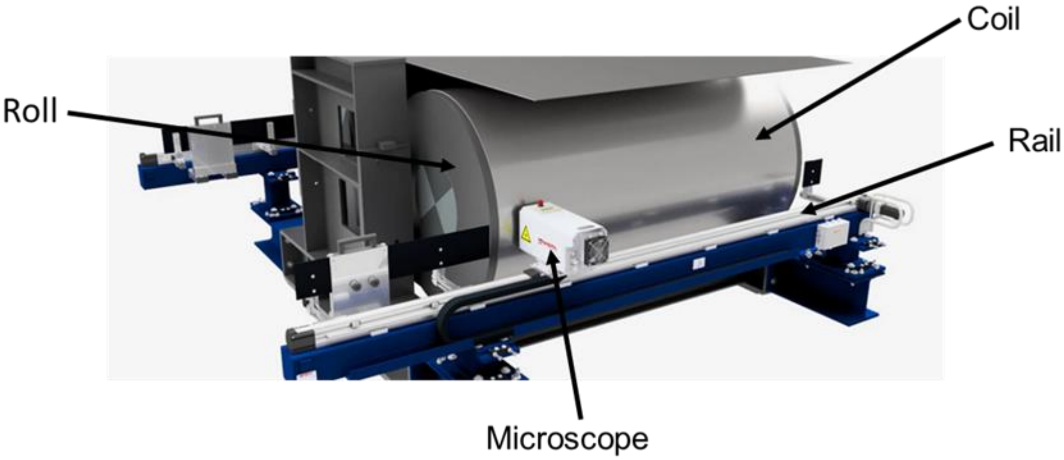

Figure 6-20: On-line microscope for imaging the strip surface at different coil locations along its width, where the microscope can move along rails [65].

A charge-coupled device (CCD) camera captures the image of the strip surface, and a laser light source illuminates the surface. The deformation of a thin laser sheet in the lateral directions is observed and converted into a height map, as shown in Figure 6-21 (a). The device can generate a 3D surface height map with a lateral resolution of ~0.1μm (with FOVs ranging from 25 – 2500 μm) [65]; the Keyence microscope uses a similar resolution for the optical micrographs in Figure 4-2 and Figure 6-7.

Figure 6-21 (b) shows an example surface height profile obtained using the Amepa on-line microscope. The obtained surface height map should be representative of surface topography outside the cavities as the cavities behave as perfect absorbers and emitters of EM radiation at most wavelengths of interest.

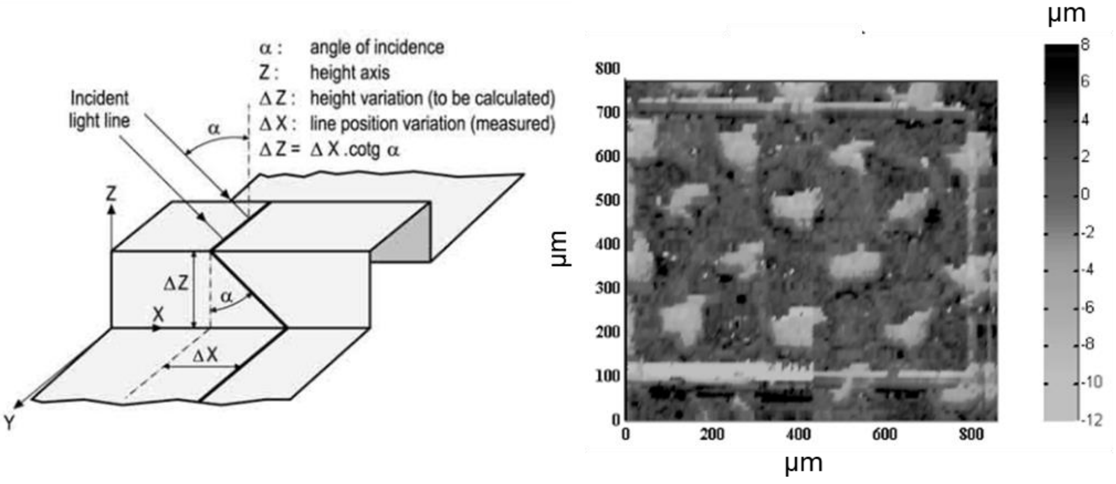

(a) **(b)**

Figure 6-21: (a) Surface height-map acquisition by Amepa microscope, through the line projection method. (b) Generated 3D height map for an examples surface [65]

The surface height,

$$\Delta Z = \Delta X \cdot \cot(\alpha) \tag{6.20}$$

is computed by imaging the movement of the line in the lateral direction, ΔX, and the beam's incident angle, α, is known. Manufacturers may use the surface heights to compute the surface slope and the RMS roughness of the exposed area through Eqs. (4.1), (4.2) and (4.3); to be used as inputs for the neural network model proposed in this thesis. Additional network training and testing must be performed using the surface topography and optical imagery from the Amepa microscope. If image thresholding cannot be applied easily for images captured using the Amepa online microscope, a convolutional neural network (CNN) may be developed to infer the cavity ratio.

6.4.2. Improving Accuracy and Uncertainty Quantification for ANN Model

Uncertainty quantification in neural networks is also a significant challenge. Neural networks have epistemic and aleatoric uncertainties [82, 83]. Epistemic uncertainty is the error associated with the model used to explain a physical process; for instance, if a model does not account for an essential factor, errors may arise in the final prediction. As such, epistemic uncertainties are also known as “knowledge uncertainties.” [82] One may reduce these errors by ensuring the model considers all pertinent phenomena and physical features. Epistemic uncertainties may be quantified through Bayesian neural networks (BNN).

On the contrary, aleatoric uncertainties arise due to inherent errors in the training data and are independent of the model. For example, the errors associated with the spectral emissivity measurements and surface roughness parameters used to train the ANN model in this study will contribute to aleatoric uncertainties. As such, more accurate training data may minimise these errors.

To model epistemic uncertainties through BNNs, which are also known as “uncertainty-aware neural networks,” [82, 83] the model parameters (weights, activation functions and biases) are set to be stochastic. Therefore, the epistemic uncertainty for a network with a model parameter set, θ, given a set of inputs, x, and outputs, y, is a probability distribution and can be expressed through Bayes' theorem,

$$p(\theta \mid x, y) = \frac{p(y \mid x, \theta) \cdot p(\theta)}{\int_{\theta} p(y \mid x, \theta') \cdot p(\theta) \mathrm{d}\theta'} \tag{6.21}$$

where $p(\theta \mid x,y)$ is the epistemic error (the inherent uncertainty which arises even without error in the training data) or the posterior, $p(y \mid x,\theta)$ is the aleatoric uncertainty or the likelihood and $p(\theta)$ is the prior distribution over the possible model parameters. The denominator represents the evidence: the aleatoric uncertainty marginalised over all possible model parameter combinations.

Statistically speaking, optimising BNNs lead to maximum *a posteriori* (MAP) estimates of the model parameters. Bayesian neural networks are usually trained through probabilistic tools such as Monte-Carlo Markov's Chain (MCMC) runs [83]. This framework shall allow for capturing neural network model uncertainties and generating uncertainty bounds for the spectral emissivity predictions made using the neural-network model.

Chapter 7 : Conclusions and Future Work

7.1: Key Findings

Steelmakers continue to grapple with the issue of non-uniform mechanical properties across single AHSS coils processed on CGLs, which lead to scrap rates in the industry as high as 30% [22]. Studies have traced these non-uniformities back to temperature excursions across single AHSS coils during the annealing process, leading to erratic changes in the steel's microstructure, as discussed in Sec. 1.2.2 affecting its mechanical properties.

Temperature excursions have often been attributed to non-uniform irradiation of the steel strip (especially across the width of the coil) as the coil passes through the continuous annealing furnace. However, further studies have shown that the radiative properties of the steel strip can also induce temperature excursions by affecting its pyrometrically-inferred temperature and altering its thermal absorption rate.

Various studies have elucidated how the radiative properties of AHSS vary during the annealing process due to changes in its temperature and surface state (primarily oxidation) through physics-based and data-driven models. However, this is the first study to analyse how the radiative properties may vary across a single AHSS coil even before it enters the annealing furnace. In addition, the pre-annealed surface state may also influence how the radiative properties subsequently evolve during annealing.

This thesis expands our understanding of these radiative property variations across a single coil and links them to differences in the surface state through a GOA ray-tracing algorithm and a data-driven artificial neural network model. Surface cavities strongly influence the pre-annealed radiative properties produced through processes upstream of annealing, such as hot-rolling, acid-pickling and cold-rolling. However, the topography outside the cavities has a minor influence on the radiative properties, at least for the samples analysed in this thesis.

Surface cavity formation occurs due to the dissolution of selective grain boundary oxides (formed during hot-rolling) during acid-pickling. Cold-rolling then flattens the cavities, where the flattening is linearly proportional to the cold-rolling reduction percentage. However, random variations in cold-rolling parameters (such as pressure) across a single coil may lead to the non-uniform flattening of cavities, leading to non-uniformities in the radiative properties across a single

AHSS coil. Therefore, future work will focus on performing a more robust analysis to fully understand the subtle effects of cold rolling on cavity flattening.

Furthermore, studies have shown that grain boundary oxidation can vary considerably across a single coil, affecting the surface cavity coverage after the hot-rolling and acid-pickling processes. These effects make it challenging to predict the radiative properties of the strip surface based on the process parameters alone. As such, the proposed data-driven machine learning model is a feasible tool to predict strip radiative properties using surface optical imagery and topographical parameters obtained using emerging on-line strip imaging technologies.

Overall, this thesis expands our knowledge base on the possible causes for non-uniformities in mechanical properties across single AHSS coils. These findings will serve as a valuable reference for steel producers and operators alike in efforts to minimise these variations and reduce the industry's high scrap rates.

7.2: Future Work

The findings of this research open many avenues for future work, some of which are discussed below:

7.2.1 Predicting Radiative Property Evolution

This work uses an FTIR and two integrating spheres, as discussed in Sec. 3.2 to analyse the radiative properties through an *ex-situ* procedure. However, on an annealing line, the radiative properties will vary with both steel strip temperature and changes in its surface state (primarily oxidation).

The changing temperature of the steel strip will influence the substrate material's refractive index, *n*, and extinction coefficient, *k*, in turn influencing the inherent radiative properties of the steel. Analytically modelling these variations is a significant challenge; for longer wavelengths (> 5 μm), the Hagen-Rubens relationship applies, where the spectral emissivity is directly proportional to the square root of surface temperature ($\varepsilon_\lambda \propto T^{1/2}$), caused by a change in the resistivity of the metal [16]. However, the relationship is reversed at the shorter wavelengths below a crossover point (~1.0 μm for Iron) [84], where spectral emissivity decreases with increasing temperature. As such, implementing a data-driven machine-learning approach may be more feasible to correlate spectral emissivity and surface temperature and requires further research.

The evolving surface states during annealing may also significantly impact strip radiative properties; for instance, the reducing atmosphere commonly used for intercritical annealing leads to forming of external and internal selective oxides, significantly affecting strip radiative properties. Oxide formation strongly depends on the steel's alloy composition (Si/Mn ratio), the annealing atmosphere's dew point temperature, and the pre-annealed surface state.

As discussed, various studies have attempted to model the impact of these parameters through physics-based and data-driven models by performing *ex-situ* characterisation of rapidly quenched AHSS alloys with varying surface states annealed at different atmospheric dew points [32, 42]. For example, Suleiman et al. [32] modelled pyrometric emissivity variations during annealing through a factorial design-of-experiments procedure. Lin et al. [85] then implemented a hybrid thin-film/GOA model to infer the radiative properties of oxidised AHSS samples; the model performed poorly on samples with as-received initial surface states due to the formation of discontinuous oxides while the model assumes a uniform oxide layer.

As such, the as-received variations in surface topography across the coil in its pre-annealed state will significantly affect how the surface state and radiative properties evolve during annealing. In addition, the influence of surface cavities on oxide formation must be explored. The highly rough surface inside the cavities should lead to the formation of oxide nodules; however, the blackbody nature of these cavities may obscure the oxides' effect. In contrast, the smooth region outside the cavities should see more continuous oxide layers forming. The layers will affect the radiative properties through thin-film interference effects.

Future work may employ an experimental approach by analysing samples from different coil locations quenched at different cycle stages in an annealing simulator to capture surface topography evolution. In addition to the *ex-situ* characterisation of the surfaces, performing *in-situ* radiative property measurements to capture the influence of varying temperatures on strip radiative properties will also benefit galvanisers.

A data-driven model may be explored for predicting radiative property evolution given the alloy composition of the steel, the applied annealing schedule, the dew point temperature of the annealing atmosphere and the pre-annealed surface state for samples from different coil locations. Galvanisers may infer the pre-annealed surface state of the steel and the initial radiative properties using the on-line microscope and the ANN model proposed in this thesis, respectively.

7.2.2 Updated Heat Transfer Model

The heat transfer model developed in Chapter 2 does not account for the metallurgical phase change of the steel, particularly the latent heat due to austenite formation during heating. The addition of this phenomenon to the model will allow galvanisers to understand better the impact of the non-uniform radiative properties across the coil (shown in Chapter 3) on the formation of austenite and martensite (during heating and subsequent quenching as discussed in Sec. 1.2.2). Which will, in turn, influence the strip mechanical properties as shown by the stress-strain curves in Sec. 3.2.2.

One feasible approach to model the phase change and formation of austenite during heating is the cellular automata (CA) technique [86], which represents the microstructure as a grid of 2D cells which are assigned different phases (Ferrite, Pearlite, or Austenite). Then, through a specific temperature evolution, the phase of each cell changes according to the states of neighbouring cells and other pre-defined phenomenological rules.

Future work may couple the heat-transfer and CA models through a finite difference approach stepping through time, where the two models are solved alternatively. Furthermore, as shown with the heat transfer model in Chapter 2, radiative properties strongly impact strip temperature evolution. As such, additional research should also incorporate the empirical radiative property evolution model from the previous section into the improved heat transfer/CA model for a robust method of predicting austenite and martensite formation. In turn, non-uniformities in mechanical properties across the coil.

7.2.3 Improving ANN Spectral Emissivity Model

Future work should also improve the neural network model for more accurate spectral emissivity predictions. This study has trained the ANN on data from the Keyence microscope; the model must be trained on data from the online microscope so galvanisers may use it in an industrial setting. Additional work should also focus on uncertainty quantification, a significant challenge in machine learning models. Using Bayesian neural networks is a possible solution for model uncertainty quantification and generating uncertainty bounds for the ANN spectral emissivity predictions.

7.2.4 Combining All Improvements

This thesis is the first to identify and characterise radiative property variations across a cold-rolled AHSS coil. It attributes these variations to differences in surface topography imparted to the coil before annealing through hot-rolling, acid-pickling and cold-rolling. These radiative property variations strongly influence pyrometric temperature measurements and strip thermal absorption, affecting the post-annealed mechanical properties through temperature excursions. The findings of this research serve as a foundation for the proposed future work described in the previous sections.

The pre-annealed surface state of the steel will significantly impact how the radiative properties may evolve during annealing. Therefore, the data-driven radiative property evolution model in Sec. 7.2.1, the improved heat transfer model in Sec. 7.2.2 and the improved ANN spectral emissivity model in Sec. 7.2.3 may be combined with the on-line strip imaging technologies to develop a robust method to predict expected mechanical property variations across a single coil caused by non-uniform austenite and martensite formation.

This predictive capability will allow manufacturers to improve real-time furnace temperature control and pyrometry algorithms. Furthermore, the findings of this research concerning the connection between the upstream processes such as hot-rolling, acid-pickling and cold-rolling, and the strip radiative properties may also allow steelmakers to reduce non-homogeneities in surface topography and radiative properties across the coil even before it enters the annealing furnace. Overall, this work provides critical insights into the AHSS manufacturing chain and identifies areas of future improvements to reduce the high-scrap rates in the industry.

References

[1] N. Fonstein, Advanced High Strength Sheet Steels: Physical Metallurgy, Design, Processing, and Properties, Cham: Springer, 2015.

[2] T. Senuma, "Physical Metallurgy of Modern High Strength Steel Sheets," *ISIJ International,* vol. 41, no. 6, pp. 520-532, 2001.

[3] "A New Global Formability Diagram," World Auto Steel, 2017. [Online]. Available: https://ahssinsights.org/blog/a-new-global-formability-diagram/. [Accessed 2023].

[4] S. Keeler, M. Kimchi and P. Mooney, "Advanced High-Strength Steels Application Guidelines Version 6," 2017. [Online]. Available: http://www.worldausosteel.org.

[5] R. I. L. Guthrie and M. M. Isac, "Continuous Casting Practices for Steel: Past, Present and Future," *Metals,* vol. 12, no. 5, p. 862, 2022.

[6] S. Ray, "Introduction to Rolling Process," in *Principles and Applications of Metal Rolling*, Cambridge University Press, 2016, pp. 1-29.

[7] D. Raabe, B. Sun, A. K. D. Silva, B. Gault, H. W. Yen, K. Sedighiani, P. T. Sukumar, I. R. S. Filho, S. Katnagallu, E. Jägle, P. Kürnsteiner, N. Kusampudi, L. Stephenson, M. Herbig, C. H. Liebscher, H. Springer, S. Zaefferer, V. Shah, S. L. Wong and C. Ba, "Current Challenges and Opportunities in Microstructure-Related Properties of Advanced High-Strength Steels," *Metallurgical and Materials Transactions A,* vol. 51, pp. 5517-5586, 2020.

[8] S. Naipinij, S. Sukieum, R. Namprai and T. Nilsonthi, "Formation of Thermal Oxide Scale and its Adhesion to Hot-Rolled Low Carbon Steels with Different Final Strip Thickness," *EDP Sciences,* vol. 355, 2022.

[9] J. Robson, "Steel Pickling: A profile.," EPA Contract 68, 1993.

[10] M. Demeri, Advanced High-Strength Steels, Science, Technology, and Application, ASM International, 2013.

[11] R. G. Davies, "Influence of Martensite Composition and Content on the Properties of Dual Phase Steels," *Metallurgical Transactions A,* vol. 9, no. 5, pp. 671-679, 1978.

[12] V. L. d. l. Concepcion, H. N. Lorusso and H. G. Svoboda, "Effect of Carbon Content on Microstructure and Mechanical Properties of Dual Phase Steels," *Procedia Materials Science,* vol. 8, pp. 1047-1056, 2015.

[13] K. Lin, *[PhD Thesis] Effect of Surface State on Radiative Properties of Advanced High Strength Steel Strips,* Waterloo: University of Waterloo, 2022.

[14] M. Blumeneau and A. Baumer, "Recent Developments in Continuous Annealing Process of Advanced High Strength Steels," in *Materials Science and Technology 2014*, Pittsburgh, 2014.

[15] S. Taylor and S. Wang, "Modelling Steel Strip Heating Within an Annealing Furnace," *Pacific Journal of Mathematics for Industry*, vol. 9, no. 1, pp. 1-15, 2017.

[16] J. R. Howell and M. P. S. R. Menguc, Thermal Radiation Heat Transfer, 6th Ed., Boca Raton: CRC Press, 2016.

[17] N. Narayanan, K. Lin, F. Suleiman and K. Daun, "The Causes and Effects of Pre-Annealed Radiative Property Variations Across Full-Hard Advanced High Strength Coils," *Steel Research International,* vol. 94, no. 3, p. 2200705, 2023.

[18] D. Bergstrom, J. Powell and A. Kaplan, "The Absorption of Light by Rough Metal Surfaces - A Three-Dimensional Ray-Tracing Analysis," *Journal of Applied Physics,* vol. 103, no. 10, 2008.

[19] D. DeWitt and G. Nutter, Theory and Practice of Radiation Thermometry, Wiley, 1988.

[20] F. Tanaka and D. DeWitt, "Theory of a New Radiation Thermometry Method and an Experimental Study Using Galvannealed Steel Specimens," *Transactions of the Society of Instrument and Control Engineers,* vol. 25, no. 10, pp. 1031-1037, 1989.

[21] R. Usamentiaga, D. Garcia, J. Molleda, F. Bulnes and J. Perez, "Temperature Measurement Using the Wedge Method: Comparison and Application to Emissivity Estimation and Compensation," *IEEE Transactions on Instrumentation and Measurement,* vol. 60, no. 5, pp. 1768-1778, 2011.

[22] Q. Somveille, *[MASc Thesis] Effect of Selective Oxidation on Temperature Measurements of AHSS with Pyrometry,* Montreal: Ecole Polytechnique de Montreal, 2018.

[23] R. Usamentiaga, J. Molleda, D. Garcia, L. Perez and G. Vecino, "Real-Time Line Scan Extraction from Infrared Images Using the Wedge Method in Industrial Environments," *Journal of Electronic Imaging,* vol. 19, no. 4, p. 043017, 2010.

[24] B. Tsai, R. Shoemaker, D. DeWitt, B. Cowans, Z. Dardas, W. Delgass and G. J. Dail, "Dual-Wavelength Radiation Thermometry: Emissivity Compensation Algorithms," *International Journal of Thermophysics,* vol. 11, no. 1, pp. 269-281, 1990.

[25] Williamson, "The Difference Between Two-Color and Dual-Wavelength Pyrometers," 2016. [Online]. Available: https://www.williamsonir.com/blog/the-difference-between-two-color-and-dual-wavelength-pyrometers/.

[26] R. Thiessen, E. Bocharova, D. Mattissen and R. Sebald, "Temperature Measurement Deviation During Annealing of Multiphase Steels," *Meterials and Metallurgical Transactions B,* vol. 41, no. 4, pp. 857-863, 2010.

[27] Q. Somveille, P. Mosser, M. Brochu and K. Daun, "Effect of Oxidation on Emissivity for DP780 and DP980 Steels," in *Galvatech 2017,* Tokyo, 2017.

[28] A. Araújo, "Multi-Spectral Pyrometry - A Review," *Measurement Science and Technology,* vol. 28, no. 8, p. 082002, 2017.

[29] C. Wen, "Investigation of Steel Emissivity Behaviors: Examination of Multispectral Radiation Thermometry Emissivity Models," *Internatioal Journal of Heat and Mass Transfer* , vol. 53, pp. 9-10, 2010.

[30] P. Coates, "Multi-Wavelength Pyrometry," *Metrologia,* vol. 17, pp. 103-109, 1981.

[31] Williamson, "Are All Single-Wavelength Infrared Pyrometers Alike?," [Online]. Available: https://www.williamsonir.com/pyrometer-wavelength-selection-guide/.

[32] F. Suleiman, K. Lin and K. Daun, "Development of a Multivariate Spectral Emissivity Model for Advanced High Strength Steel Alloy Through Factorial Design-Of-Experiments," *Journal of Quantitative Spectroscopy and Radiative Transfer,* vol. 271, p. 107693, 2021.

[33] M. Niederer, S. Strommer, A. Steinboeck and A. Kugi, "Nonlinear Predictive Control of the Strip Temperature in an Annealing Furnace," *Jounal of Process Control,* vol. 48, pp. 1-13, 2016.

[34] C. Rogalski, *[MASc Thesis] Application of a Network Model for Complex Fenestration Systems,* Wateroo: University of Waterloo, 2011.

[35] T. A. Blake, T. J. Johnson, R. G. Tonkyn, B. M. Forland, T. L. Myers, C. S. Brauer, Y.-F. Su, B. E. Bernacki, L. H. Gonzalez and G. Gonzales, "Methods for quantitative infrared directional-hemispherical and diffuse reflectance measurements using an FTIR and a commercial integrating sphere," *Applied Optics,* vol. 57, no. 3, pp. 432-446, 2018.

[36] Labsphere, "Reflectance Coatings and Materials," Labsphere, [Online]. Available: https://www.labsphere.com/wp-content/uploads/2022/01/Coatings-and-Materials-Solutions.pdf. [Accessed 2023].

[37] K. Lin, F. Suleiman and K. Daun, "interpreting the Radiative Properties of Advanced High Strength Steel Using the Geometric Optics Approximation," *International Journal of Heat and Mass Transfer,* vol. 176, p. 121429, 2021.

[38] M. Ordal, R. Bell, R. Alexander, L. Newquist and M. Querry, "Optical Properties of Aluminum, Iron, Titanium, Tantalu,. Tungsten, and Molybdenum at Submillimeter Wavelengths," *Applied Optics,* vol. 27, no. 6, pp. 1203-1209, 1988.

[39] R. C. P. Johnson, "Optical Constants of Transition Metals: Ti, V, Cr, Mn, Fe, Co, Ni, Pd," *Physical Review B, Solid State,* vol. 9, no. 12, pp. 5056-5070, 1974.

[40] P. Mosser, Q. Someveille, K. Daun and M. Brochu, "Effect of Temperature Deviation During Intercritical Annealing of HSLA and DP980 Steels," in *Galvatech 2017*, Tokyo, 2017.

[41] Y. Ma, W. Song, S. Zhou, A. Schwedt and W. Bleck, "Influence of Intercritical Annealing Temperature on Microstructure and Mechancial Properties of a Cold-Rolled Medium Mn Steel," *Metals (Basel),* vol. 8, no. 5, 2018.

[42] K. Lin, M. Pourmajidian, F. Suleiman, J. McDermid and K. Daun, "Effect of Annealing Atmosphere and Steel Alloy Composition on Oxide Formation and Radiative Properties of Advanced High Strenght Steel Strip," *Metallurgical and Materials Transactions B,* vol. 53, pp. 380-393, 2022.

[43] S. Ham, C. Carteret, J. Angulo and G. Fricout, "Relation Between Emissivity Evolution During Annealing and Selective Oxidation of TRIP Steel," *Corrosion Science,* vol. 132, pp. 185-193, 2018.

[44] J. Elchert, "Cryogenic Multilayer Insulation Theory and An Analysis of Seams Under a Variety of Assumptions," Thermal and Fluids Analysis Workshop 2018, Houston, 2018.

[45] H. Lee, D. Yang, J. W. Yoon and Y. W, "Numerical Modelling and Analaysis for Forming Process of Dual Phase 980 Steel Exposed to Infrared Local Heating," *International Journal of Solids and Structures,* vol. 75, pp. 211-224, 2015.

[46] K. Lin and K. Daun, "interpreting the Spectral reflectance of Advanced High Strength Steels Using the Davies' Model," *Journal of Quantitative Spectroscopy and Radaitive Transfer,* vol. 242, p. 106796, 2020.

[47] C. Wen and I. Mudawar, "Modelling the Effect of Surface Roughness on the Emissivity of Aluminum Alloys," *International Journal of Heat and Mass Transfer,* vol. 49, no. 23, pp. 4279-4289, 2006.

[48] D. Bergstrom, J. Powell and A. Kaplan, "A Ray-Tracing Analysis of the Absorption of Light by Smooth and Rough Metal Surfaces," *Jounral of Applied Physics,* vol. 101, p. 113504, 2007.

[49] K. Tang, R. Dimenna and R. Buckius, "Regions of Validity of the Geometric Optics Approximation for Angular Scattering from Very Rough Surfaces," *international Journal of Heat and Mass Transfer,* vol. 40, no. 1, pp. 49-59, 1997.

[50] K. K. Tang and R. O. Buckius, "The Geometric Optics Approximation for Reflection form Two-Dimensional Random Rough Surfaces," *International Journal of Heat and Mass Transfer,* vol. 41, no. 13, pp. 2037-2047, 1998.

[51] N. Kopper, F. Luther and T. Koll, "On Grain Boundary Topography and Surface Reactivity During Hot-Dip Galvanising," in *Galvatech 2021*, Vienna, 2021.

[52] U. Etzold, K. Mohr and P. Hulser, "The Use of Corrosion Inhibitors in Steel Strip Production and Coating," in *38DG Seminario de Laminacao Processos e Produtos Laminados e Revestidos*, 2001.

[53] D. Montgomery, Deisgn and Analysis of Experiments 8th Ed., New York: John Wiley & Sons, 2013.

[54] C. Daniel, "Use of Half-Normal Plots in Interpreing Factorial Two Level Experiments," *Technometrics,* vol. 1, pp. 311-342, 1959.

[55] M. Öner and I. Kocakoç, "A Compilation of Some Popular Goodness of Fit Tests for Normal Distribution: Their Algorithms and MATLAB Codes," *Journal of Modern Applied Statistical Methods,* vol. 16, 2017.

[56] O. Wiklund and F. Sandberg, "Chapter 15 - Modelling and Control of Temper Rolling and Skin Pass Rolling," in *Metal Forming Science and Practice*, Elsevier, 2002, pp. 313-343.

[57] Y. Park and S. Lek, "Chapter 7 - Artificial Neural Networks: Multilayer Perceptron for Ecological Modeling," vol. 28, pp. 123-140, 2016.

[58] E. Grossi and M. Buscema, "Introduction to Artificial Neural Networks," *European Journal of Gastroenterology & Hepatology,* vol. 19, no. 12, pp. 1046-1054, 2007.

[59] O. Abiodun, A. Jantan, A. Omolara, K. Dada, K. Mohamed and H.Arshad, "State-Of-The-Art in Artificial Neural Network Applications: A survey," *Heliyon,* vol. 4, no. 11, p. e00938, 2018.

[60] P. d. Harrington, "Sigmoid Transfer Function in Backpropogation Neural Networks," *Analytica,* vol. 65, no. 1993, pp. 2167-2168, 65.

[61] H. Kang, M. Kaya and S. Hajimirza, "A Data-Driven Artificial Neural Network Model for Predicting Radaitive Properties of Metallic Packed Beads," *Jounral of Quantitative Spectroscopy and Radiative Transfer*, vol. 226, pp. 66-72, 2019.

[62] J. Sullivan, A. Mirhashemi and J. Lee, "Deep Learning-Based Analysis of Microstructured Materials for Thermal Radiation Control," *Scientific Reports,* vol. 12, p. 9785, 2022.

[63] G. Acosta, M. A. Reicks, Moreno, A. Borjali, C. Zuhlke and M. Ghashami, "Emissivity Prediction of Functionalized Surfaces Using Artificial Neural Networks," *Journal of Quantitative Spectroscopy and Radiative Transfer,* vol. 291, p. 108325, 2022.

[64] H. Lee, "Simple Regression Model for Estimating Reflectance Reduction Due to Radnom Surface Roughness," *Internation Journal of Thermophysics,* vol. 40, no. 6, p. 55, 2019.

[65] M. Geneviève, "Advanced Sensor for On-Line Topography in Coninuous Annealing Lines," *La Revue de Metallurgie,* vol. 103, no. 5, pp. 233-237, 2006.

[66] H. Yu and B. Wilamowski, "Levenberg-Marquardt Training," in *Intelligent Systems,* CRC Press, 2011.

[67] H. Bennett and J. Porteus, "Relation Between Surface Roughness and Specular Reflectance at Normal Incidence," *Journal of the Optical Society of America*, vol. 51, no. 2, pp. 123-129, 1961.

[68] L. Ciao and K. Sendur, "Surface Roughness Effects on the Broadband Reflection for Refractory Metals and Polar Dielectrics," *Mateirals,* vol. 12, no. 19, p. 3090, 2019.

[69] N. Guliyev and V. Ismailov, "On the Approximation by Single Hiddne Layer Feedforward Neural Networks with Fixed Weights," *Neural Networks,* vol. 98, pp. 296-304, 2018.

[70] A. Thomas, M. Petridis, S. Walters, S. Gheytassi and R. Morgan, "Two Hidden Layers are Usually Better than One," *Communications in Computer and Information Science,* vol. 744, pp. 279-290, 2017.

[71] A. Eghtesad, F. Tabassum and S. Hajimirza, "A generalized characterization of radiative properties of porous media using engineered features and artificial neural networks," *International Journal of Heat and Mass Transfer,* vol. 205, p. 123890, 2023.

[72] M. Kott, M. Kraft, E. A and P. Groche, "Variance Based Sensitivity Analysis of Deep Drawing Process Based on Neural Networks Using Sobol Indices," *Material Science Engineering*, vol. 1157, p. 02309, 2021.

[73] Y. C. Liu, J. Nagawkar, L. Leifsson, S. Koziel and A. P. Dabrowska, "Iterative Global Sensitivity Analysis Algorithm With Neural Networks Surrogate Modeling," *Computational Science - ICCS 2021,* pp. 298-311, 2021.

[74] C. Xu and G. Gertner, "Extending a Global Sensitivity Analysis Technique to Model with Correlated Parameters," *Computational Statistics and Data Analysis,* vol. 51, pp. 5579-5990, 2007.

[75] G. McRae, J. Tilden and J. Seinfeld, "Glibal Sensitivity Analysis - A Computational Implementation of the Fourier Amplitude Sensitivity Test (FAST)," *Computers & Chemical Engineering,* vol. 6, no. 1, pp. 15-25, 1982.

[76] M. Haaker and P. Verheijen, "Local and Global Sensitivity Analysis for a Reactor Design with Parameter Uncertainty," *Chemical Enigneering Research and Design,* vol. 38, no. 5, pp. 591-598, 2004.

[77] I. Kioutsioukis, S. Tarantola, A. Saltelli and D. Gatelli, "Uncertainty and Global Sensitivity Analysis of Road Transport Emission Estimates," *Atmospheric Environment,* vol. 38, no. 38, pp. 6609-6620, 2004.

[78] A. Saltelli, S. Tarantola and K. Chan, "A Quantitative Model-Independent Method for Global Sensitivity Analysis of Model Output," *Technometrics,* vol. 41, pp. 39-56, 1999.

[79] R. Cukier, C. Fortuin and K. Schuler, "Study of the Sensitivity of Coupled Reaction Systems to Uncertainties in Rate Coefficients. III. Analysis of the Approximations," *Jounal of Chemical Physics,* vol. 63, pp. 1140-1149, 1975.

[80] R. L. Iman and W. Conover, "A Distribution Free Approach to Introducing Rank Correlation Among Input Variables," *Communications in Statistics - Simulation and Computation,* vol. 11, no. 3, pp. 311-334, 1982.

[81] K. Fu and P. Hsu, "New Regime Map of the Geometric Optics Approximation for Scattering from Random Rough Surfaces," *Journal of Quantitative Spectroscopy and Radiative Transfer,* vol. 109, pp. 180-188, 2008.

[82] M. Abdar, F. Pourpanah, S. Hussain, D. Rezazadegan, L. Liu and M. Ghavamzadeh, "A Review of Uncertainty Quantification in Deep Learning, Applications and Challenges," *information Fusion,* vol. 76, pp. 243-297, 2021.

[83] L. Jospin, H. Laga, F. Boussaid, W. Buntine and M. Bennamoun, "Hands-On Bayesian Neural Networks - A Turorial for Deep Learning Users," *IEEE Computational Intelligence Magazine,* vol. 17, no. 2, pp. 29-48, 2022.

[84] D. Price, "The Temperature Variation of the Emissivity of Metals in the Near Infra-Red," *Proceedings of the Physical Society,* vol. 59, no. 131, 1947.

[85] K. Lin, M. Pourmajidian, F. Suleiman, J. McDermid and K. Daun, "Interpreting the Radiative Properties of Advanced High Strength Steel Strip Using a Hybrid Thin

Film/Geometric Optics Model," *Journal of Quantitative Spectroscopy and Radiative Transfer*, vol. 277, p. 107963, 2022.

[86] C. Halder and M. Madej, "Discrete Micros-Scale Cellular Model for Modelling Phase Change Transformations During Heating of Dual Phase Steels," *Archives of Civil and Mechanical Engineering*, vol. 14, pp. 96-103, 2020.

Appendix A: Replicate Measurements

From a select number of coil locations (450m Mid, 880m Mid & 1684m Edge), eight samples, in addition to the five samples, are extracted and analysed to yield results from 13 samples. The standard errors across these 13 samples are analysed, and the error bars in Figure 2 at these coil locations reflect this standard error. Figure C.1 shows the spectral direction emissivities of the 13 samples at these coil locations. The low variance in emissivities amongst these samples shows that the result from one sample is representative of others from the same coil location.

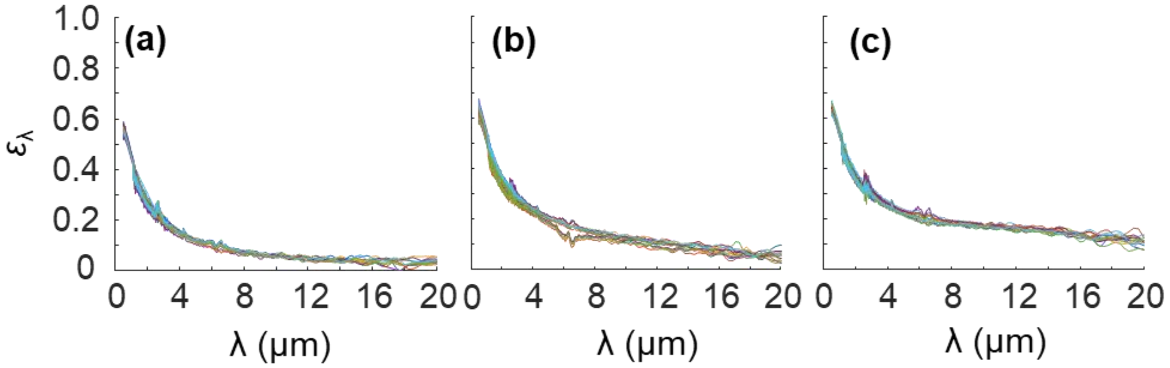

Figure A.1.: Spectral emissivities of 13 replicate samples at three select locations across the coil. The low variance in these curves shows that one sample's results are representative and broadly applicable. (a) 450m Edge, (b) 1684m Mid, (c) 880m Mid.

Additionally, Table C.1 shows the summary statistics for all 13 samples; the similarities of the surface slopes amongst the 13 samples further show that one sample represents all samples from the same location.

	Replicates												
Sample	**1**	**2**	**3**	**4**	**5**	**6**	**7**	**8**	**9**	**10**	**11**	**12**	**13**
450m Edge	0.231	0.243	0.231	0.242	0.231	0.193	0.221	0.211	0.212	0.214	0.222	0.220	0.210
1684m Mid	0.220	0.217	0.217	0.226	0.227	0.223	0.221	0.215	0.216	0.220	0.213	0.211	0.216
880m Mid	0.226	0.224	0.240	0.225	0.239	0.227	0.219	0.218	0.222	0.240	0.238	0.216	0.223

Table A.1.: Surface slope values of the 13 replicates from the three select locations. The similarities of the values across these 13 samples show that one sample is representative and broadly applicable.

Appendix B: Normality of Surface Heights

Surfaces produced through cold rolling usually have a Gaussian surface height distribution. Figure B.1 shows the normal probability plots of the surface heights for select samples. Again, the surface heights appear mostly normal, with a skewness at the tails for most samples.

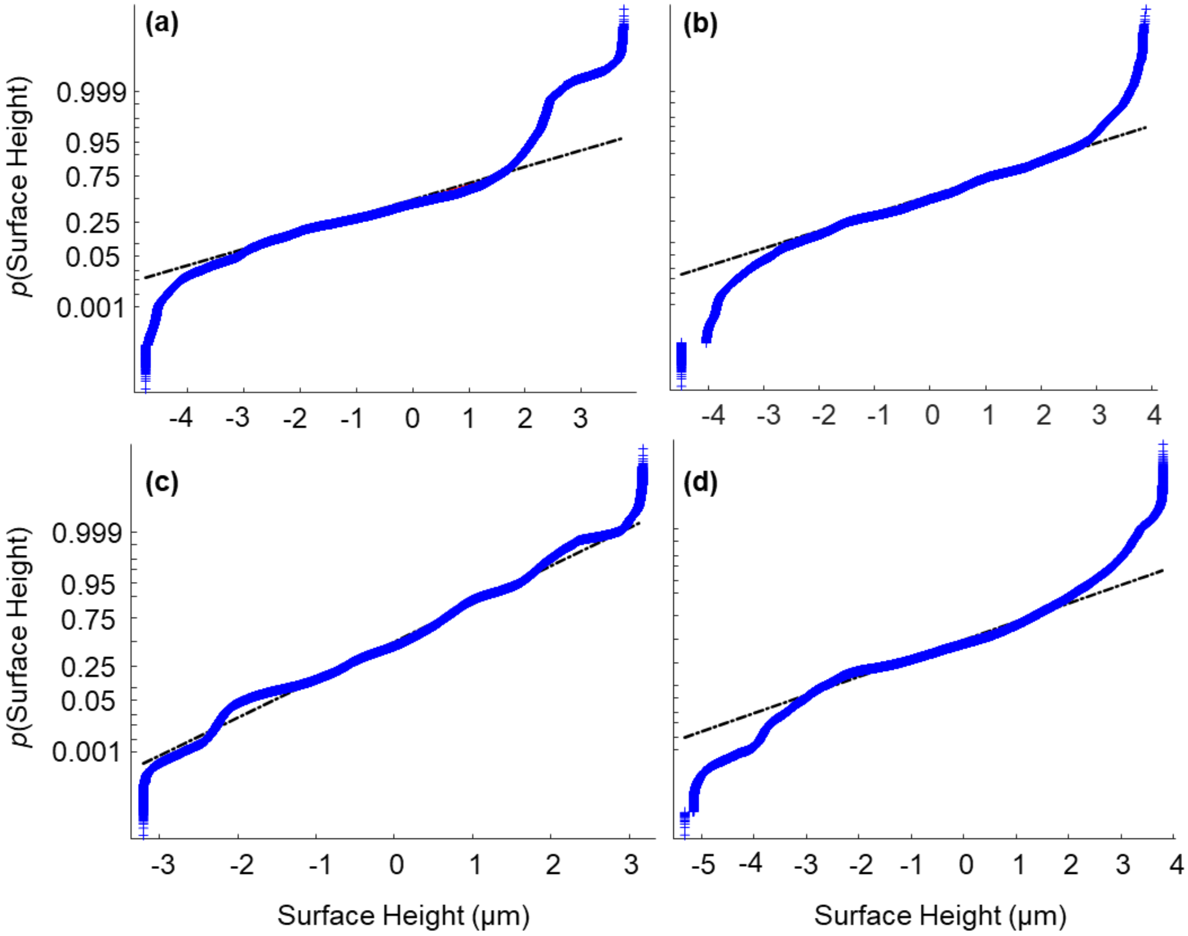

Figure B.1.: Normal probability plots of surface heights for a subset of samples. The distributions are mostly normal except for skewness at the tails. (a) 20m Edge, (b) 75m Edge, (c) 75 Mid, (d) 1509m Mid

Appendix C: Scanning Area Selection & Summary Statistics

The scanning area for the summary statistics presented in Table 4-1 was selected according to previous studies that have analysed the surface parameters of AHSS, such as Ham et al. [40] and Lin et al. [35,44]. These studies used regions of approximately (500µm × 500µm) sufficient to ensure they represented the sample while minimising undue analysis time associated with a larger sample area.

This study analyses five locations (500µm × 500µm) on a single sample for a few samples; additionally, larger scan areas are also tested at their centres for specific samples. Figure C1 shows these scanning locations.

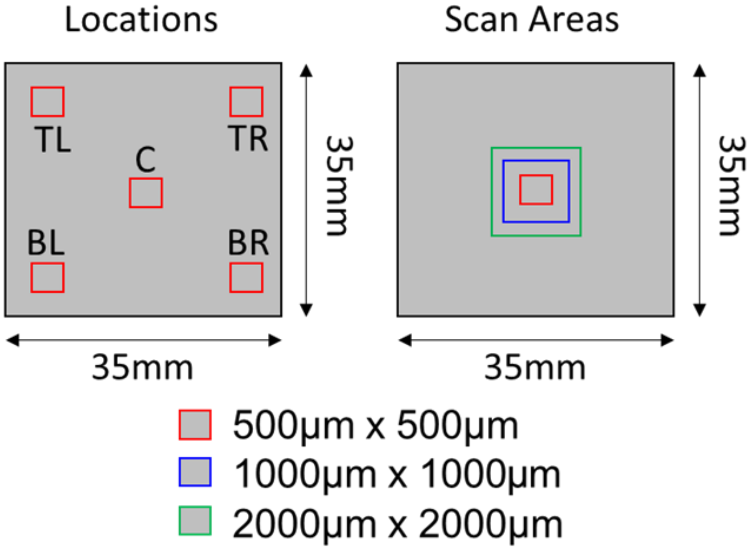

Figure C.1.: Locations of (500µm x 500µm) areas analysed from five different locations on a single sample (not to scale)

The similarity of the roughness statistics at the five locations shows that a single scanning area (500µm x 500µm) anywhere on a sample is representative of the whole sample (Table C.1). Additionally, the similarities between the surface slopes among the different scanning area sizes also shows that an area of (500µm x 500µm) is representative (Table C.2).

	$(R_q/\tau)_g$				
	Locations				
Sample	Centre	Bottom Left	Top Left	Top Right	Bottom Right
450m Edge	0.232	0.252	0.227	0.219	0.218
880m Mid	0.227	0.231	0.231	0.229	0.229

Table C.1.: Summary statistics for the five locations imaged on two select samples. The similarity of the summary statistics shows that the scanning area is representative of the whole sample.

	Scan Area (μm x μm)		
	500 x 500	**1000x1000**	**2000 x 2000**
880m Mid	0.223	0.221	0.229
1684m Mid	0.217	0.221	0.222

Table C.2.: Summary statistics for different scan areas performed on several samples. The similarities in the surface slopes amongst the different scan areas show that the (500 x 500) sample size is large enough to correct for local effects.

Appendix D: Levenberg-Marquardt Algorithm

The Levenberg-Marquardt algorithm combines gradient descent and the Gauss-Newtown minimisation methods. At the early stages of training, gradient descent is preferred when the weights and biases are furthest from their optimum values and the cost function's gradient is high. Closer to the optimum values, however, as the cost function gradient reduces, the Gauss-Newton method performs better as it utilises the second derivative of the cost function for finer adjustments.

The algorithm updates the weights and biases through,

$$\mathbf{w}_{\mathrm{k+1}} = \mathbf{w}_{\mathrm{k}} - \left(\mathbf{J}^{\mathrm{T}}_{\mathrm{k,w}} \cdot \mathbf{J}_{\mathrm{k,w}} + \mu \mathbf{I}\right)^{-1} \cdot \mathbf{J}_{\mathrm{k,w}} \cdot \mathbf{e}_{\mathrm{k}} \tag{D-1}$$

$$\mathbf{b}_{\mathrm{k+1}} = \mathbf{b}_{\mathrm{k}} - \left(\mathbf{J}^{\mathrm{T}}_{\mathrm{k,b}} \cdot \mathbf{J}_{\mathrm{k,b}} + \mu \mathbf{I}\right)^{-1} \cdot \mathbf{J}_{\mathrm{k,b}} \cdot \mathbf{e}_{\mathrm{k}} \tag{D-2}$$

where k represents the epoch of training, $\boldsymbol{w}$ is a matrix containing the weights of all connections in the network, $\mathbf{B}$ is a matrix containing the biases of all neurons in the network, $\mathbf{J}_{\mathrm{k,w}}$ and $\mathbf{J}_{\mathrm{k,b}}$ are the Jacobian matrices containing the gradients of the residuals (the residuals between the actual values and the predictions) with respect to each of the weights and biases in the network, and $\boldsymbol{e}_{\mathrm{k}}$ is the residual vector across the samples in the training dataset. Matrix $\mathbf{I}$ is the identity matrix, which has a size equivalent to the number of rows in the Jacobian. The Jacobian is,

$$\mathbf{J}_{\mathrm{k,w}} = \begin{bmatrix} \frac{\partial e_{1,1}}{\partial w_1} & \frac{\partial e_{1,1}}{\partial w_2} & \cdots & \frac{\partial e_{1,1}}{\partial w_N} \\ \frac{\partial e_{1,2}}{\partial w_1} & \frac{\partial e_{1,2}}{\partial w_2} & \cdots & \frac{\partial e_{1,2}}{\partial w_N} \\ \cdots & \cdots & \cdots & \cdots \\ \frac{\partial e_{1,M}}{\partial w_2} & \frac{\partial e_{1,M}}{\partial w_2} & \cdots & \frac{\partial e_{1,M}}{\partial w_N} \\ \cdots & \cdots & \cdots & \cdots \\ \frac{\partial e_{p,1}}{\partial w_2} & \frac{\partial e_{p,1}}{\partial w_2} & \cdots & \frac{\partial e_{p,2}}{\partial w_N} \\ \frac{\partial e_{p,2}}{\partial w_2} & \frac{\partial e_{p,2}}{\partial w_2} & \cdots & \frac{\partial e_{p,2}}{\partial w_N} \\ \cdots & \cdots & \cdots & \cdots \\ \frac{\partial e_{p,M}}{\partial w_2} & \frac{\partial e_{p,2}}{\partial w_2} & \cdots & \frac{\partial e_{p,M}}{\partial w_N} \end{bmatrix} \tag{D-3}$$

where p is the number of training samples, M is the number of outputs, and N is the number of weights in the network. The method uses a similar Jacobian for the biases. The algorithm then computes the gradients in the Jacobian matrices through a chain rule of partial derivates through backpropagation. The parameter μ is an adaptation parameter set to a very large value at the beginning of training. It is progressively reduced as the model's performance improves on the validation dataset (i.e., as the parameters approach their optimum values).

For large μ values, the update equation approaches the gradient descent method and simplifies to

$$\mathbf{w}_{\mathrm{k+1}} = \mathbf{w}_{\mathrm{k}} - a \cdot \mathbf{g}_{\mathrm{k,w}} \tag{D-4}$$

$$a = \frac{1}{\left(\mathbf{J}^{\mathrm{T}}_{\mathrm{k,w}} \cdot \mathbf{J}_{\mathrm{k,w}} + \mu \mathbf{I}\right)}, \mathbf{g}_{\mathrm{k,w}} = \mathbf{J}_{\mathrm{k,w}} \cdot \mathbf{E}_{\mathrm{k}} \tag{D-5}$$

where $\boldsymbol{a}$ represents the step size in gradient descent and $g_{\mathrm{k,w}}$ is the cost function gradient. A similar process can then be followed for the biases. If the value of μ is small, the algorithm approaches the Gauss-Newton method, and the weights are updated as,

$$\mathbf{w}_{\mathrm{k+1}} = \mathbf{w}_{\mathrm{k}} - \left(\mathbf{J}_{\mathrm{k,w}}^{\mathrm{T}} \cdot \mathbf{J}_{\mathrm{k,w}}\right)^{-1} \cdot \mathbf{J}_{\mathrm{k,w}} \cdot \mathbf{e}_{\mathrm{k}} \tag{D-6}$$

$$\mathbf{H} = \mathbf{J}_{\mathrm{k,w}}^{\mathrm{T}} \cdot \mathbf{J}_{\mathrm{k,w}} \tag{D-7}$$

H is the Hessian matrix approximated using the Jacobian and its transpose. The Hessian contains the second derivates of the cost function with respect to each weight in the network; again, a similar process can then be followed for the biases.

Appendix E: Variance Computation

The following shows the derivation of the variance equation for function *f*(*s*) from its Fourier expansion:

$$V = \mathrm{E}\left[f\left(\mathrm{s}\right)^2 \right] - \left[\mathrm{E}\left\{ f\left(\mathrm{s}\right) \right\} \right]^2 \tag{E-1}$$

$$f\left(s\right) = A_0 + \sum_{\mathrm{p}=1}^{\infty} \left\{ A_{\mathrm{p}} \cdot \cos\left(p \cdot s\right) + B_{\mathrm{p}} \cdot \sin\left(p \cdot s\right) \right\} \tag{E-2}$$

$$\mathrm{E}\left[f\left(\mathrm{s}\right)^2 \right] = \frac{1}{2\pi} \cdot \int_{-\pi}^{\pi} \left[A_0 + \sum_{\mathrm{p}=1}^{\infty} \left\{ A_{\mathrm{p}} \cos\left(s \cdot p\right) + B_{\mathrm{p}} \sin\left(s \cdot p\right) \right\} \right]^2 \mathrm{ds} \tag{E-3}$$

$$\left[\mathrm{E}\left\{ f\left(\mathrm{s}\right) \right\} \right]^2 = \frac{1}{4\pi^2} \cdot \left[\int_{-\pi}^{\pi} \left[A_0 + \sum_{\mathrm{p}=1}^{\infty} \left\{ A_{\mathrm{p}} \cos\left(s \cdot p\right) + B_{\mathrm{p}} \sin\left(s \cdot p\right) \right\} \right] \mathrm{ds} \right]^2 \tag{E-4}$$

$$\mathrm{E}\left[f\left(\mathrm{s}\right)^2 \right] = \frac{1}{2\pi} \int_{-\pi}^{\pi} \left[A_0^2 + 2A_0 \cdot \left\{ \sum_{\mathrm{p}=1}^{\infty} \left(A_{\mathrm{p}} \cos\left(s \cdot p\right) + B_{\mathrm{p}} \sin\left(s \cdot p\right) \right) \right\} + \left\{ \sum_{\mathrm{k}=1}^{\infty} \left(A_{\mathrm{p}} \cos\left(s \cdot p\right) + B_{\mathrm{p}} \sin\left(s \cdot p\right) \right) \right\}^2 \right] \mathrm{ds}$$

(E-5)

$$\mathrm{E}\left[f\left(\mathrm{s}\right)^2 \right] = A_0^2 + \frac{A_0}{\pi} \int_{-\pi}^{\pi} \sum_{p=1}^{\infty} \left[A_{\mathrm{p}} \cos\left(s \cdot p\right) + B_{\mathrm{p}} \cdot \sin\left(s \cdot p\right) \right] \mathrm{ds} + \frac{1}{2\pi} \int_{-\pi}^{\pi} \sum_{p=1}^{\infty} \left[\left\{ A_{\mathrm{p}} \cos\left(s \cdot p\right) + B_{\mathrm{p}} \cdot \sin\left(s \cdot p\right) \right\} \right]^2 \mathrm{ds}$$

(E-6)

$$\left[\mathrm{E}\left\{ f\left(\mathrm{s}\right) \right\} \right]^2 = \frac{1}{4\pi^2} \left[\begin{array}{l} \left(\int_{-\pi}^{\pi} A_0 \mathrm{ds} \right)^2 + 2 \times \int_{-\pi}^{\pi} A_0 \mathrm{ds} \times \int_{-\pi}^{\pi} \left\{ \sum_{\mathrm{p}=1}^{\infty} A_{\mathrm{p}} \cdot \cos\left(s \cdot p\right) + B_{\mathrm{k}} \cdot \sin\left(s \cdot p\right) \right\} \mathrm{ds} + \\ \left\{ \int_{-\pi}^{\pi} \sum_{\mathrm{k}=1}^{\infty} A_{\mathrm{p}} \cdot \cos\left(s \cdot p\right) + B_{\mathrm{p}} \cdot \sin\left(s \cdot p\right) \right\}^2 \end{array} \right] \tag{E-7}$$

$$\left[\mathrm{E}\left\{f(\mathrm{s})\right\}\right]^2 = A_0^2 + \frac{A_0}{\pi}\cdot\int_{-\pi}^{\pi}\sum_{\mathrm{p}=1}^{\infty} A_{\mathrm{p}}\cos(s\cdot p)+B_{\mathrm{p}}\sin(s\cdot p)\mathrm{ds} + \frac{1}{4\pi^2}\left[\int_{-\pi}^{\pi}\left(\sum_{\mathrm{p}=1}^{\infty}A_{\mathrm{p}}\cos(s\cdot p)+B_{\mathrm{p}}\sin(s\cdot p)\right)\mathrm{ds}\right]^2$$

(E-8)

$$\therefore V = \frac{1}{2\pi}\int_{-\pi}^{\pi}\left(\sum_{\mathrm{p}=1}^{\infty}A_{\mathrm{p}}\cos(s\cdot p)+B_{\mathrm{p}}\sin(s\cdot p)\right)^2\mathrm{ds} - \frac{1}{4\pi^2}\left[\int_{-\pi}^{\pi}\left(\sum_{\mathrm{k}=1}^{\infty}A_{\mathrm{p}}\cos(s\cdot p)+B_{\mathrm{p}}\sin(s\cdot p)\right)\mathrm{ds}\right]^2$$

(E-9)

For a single Fourier term, *p*, let,

$$P_{\mathrm{p}} = \frac{1}{2\pi}\int_{-\pi}^{\pi}\left(A_{\mathrm{p}}\cos(s\cdot p)+B_{\mathrm{p}}\sin(s\cdot p)\right)^2\mathrm{ds} \tag{E-10}$$

$$Q_{\mathrm{p}} = \frac{1}{4\pi^2}\cdot\left[\int_{-\pi}^{\pi}\left(A_{\mathrm{p}}\cos(s\cdot p)+B_{\mathrm{p}}\sin(s\cdot p)\right)\mathrm{ds}\right]^2 \tag{E-11}$$

$$P_{\mathrm{p}} = \frac{1}{2\pi}\left[\int_{-\pi}^{\pi}A_{\mathrm{p}}^2\cdot\cos^2(s\cdot p)\mathrm{ds} + \int_{-\pi}^{\pi}2\cdot A_{\mathrm{p}}\cdot B_{\mathrm{p}}\cdot\cos(s\cdot p)\sin(s\cdot p)\mathrm{ds} + \int_{-\pi}^{\pi}B_{\mathrm{p}}^2\cdot\sin^2(s\cdot p)\mathrm{ds}\right]$$

(E-12)

$$Q_{\mathrm{p}} = \frac{1}{4\pi^2}\left[\left(\int_{-\pi}^{\pi}A_{\mathrm{p}}\cos(s\cdot p)\mathrm{ds}\right)^2 + 2\int_{-\pi}^{\pi}A_{\mathrm{p}}\cos(s\cdot p)\mathrm{ds}\times\int_{-\pi}^{\pi}B_{\mathrm{p}}\sin(s\cdot p)\mathrm{ds} + \left(\int_{-\pi}^{\pi}B_{\mathrm{p}}\sin(s\cdot p)\mathrm{ds}\right)^2\right]$$

(E-13)

For any positive integer, *p*, the values of the integrals of the sines and cosines from -π to π are the same, as their arguments will always be an integer multiple of π. As such,

$$P_{\mathrm{p}} - Q_{\mathrm{p}} = \frac{A_{\mathrm{p}}^2}{2\pi}\int_{-\pi}^{\pi}\cos^2(s\cdot p)\mathrm{ds} + \frac{B_{\mathrm{p}}^2}{2\pi}\int_{-\pi}^{\pi}\sin^2(s\cdot p)\mathrm{ds} = \frac{1}{2}\left(A_{\mathrm{p}}^2 + B_{\mathrm{p}}^2\right) \tag{E-14}$$

In turn, the variance,

$$V = \frac{1}{2}\sum_{\mathrm{p}=1}^{\infty}\left(A_{\mathrm{p}}^2 + B_{\mathrm{p}}^2\right) \tag{E-15}$$

can subsequently be expressed as the super-position of the Fourier terms.

Appendix F: Probability Distributions of ANN Input Data

This work uses surface topography data from samples in datasets 1, 2, and 3 to approximate PDFs to sample values for the FAST-C algorithm. It is challenging to estimate standard parametric distributions to model the inputs. As such, and to avoid making assumptions about the data distribution, non-parametric kernel distributions are implemented using MATLAB®'s *distfit* and *ksdensity* functions. The PDF of the kernel distribution is,

$$pdf\left(x\right)=\frac{1}{nh}\cdot\sum_{\mathrm{i}=1}^{n}K\left(\frac{x-x_{\mathrm{i}}}{h}\right) \tag{F-1}$$

where *K* is a Gaussian kernel, *n* is the number of samples, and *h* is the bandwidth. Figure F.1 and Figure F.2 show the normalised histograms of the inputs and their respective overlayed PDFs for the surface topography parameters and the optical constants of the substrate.

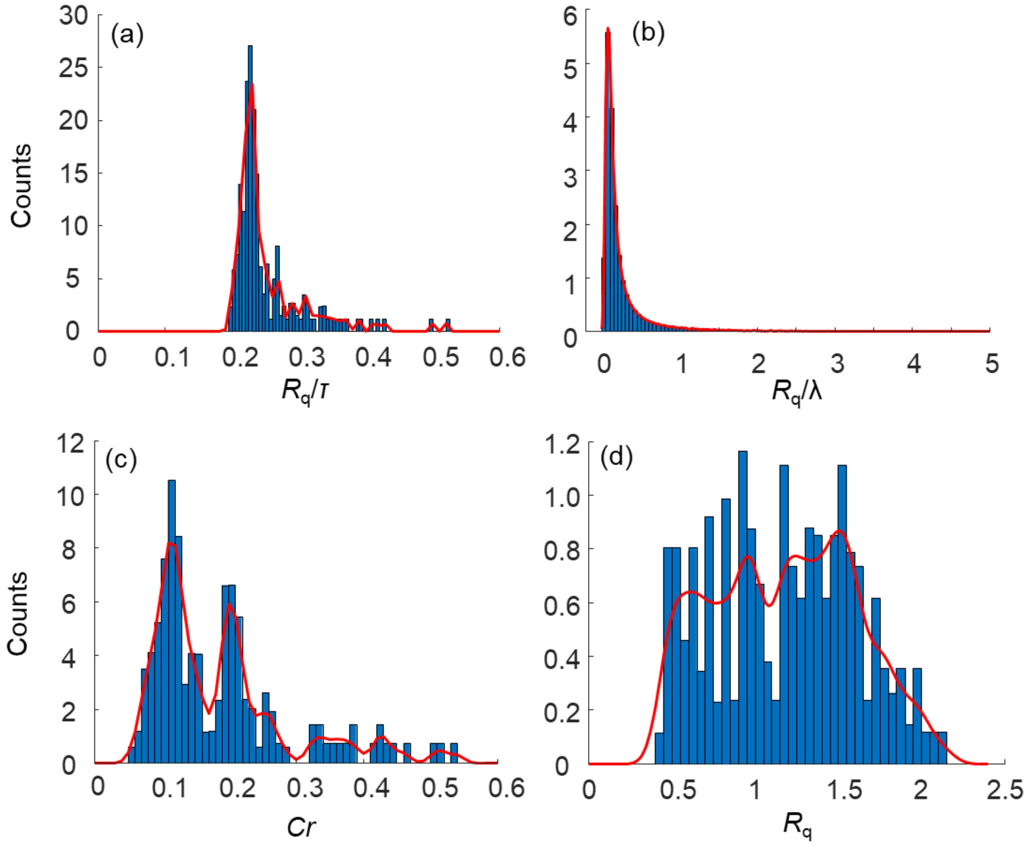

Figure F.1: Normalised histograms and the Kernal PDFs generated for surface topography parameters (a) Slope, (b) Wavelength-Normalised RMS Roughness, (c) The Cavity Ratio, and (d) RMS roughness.

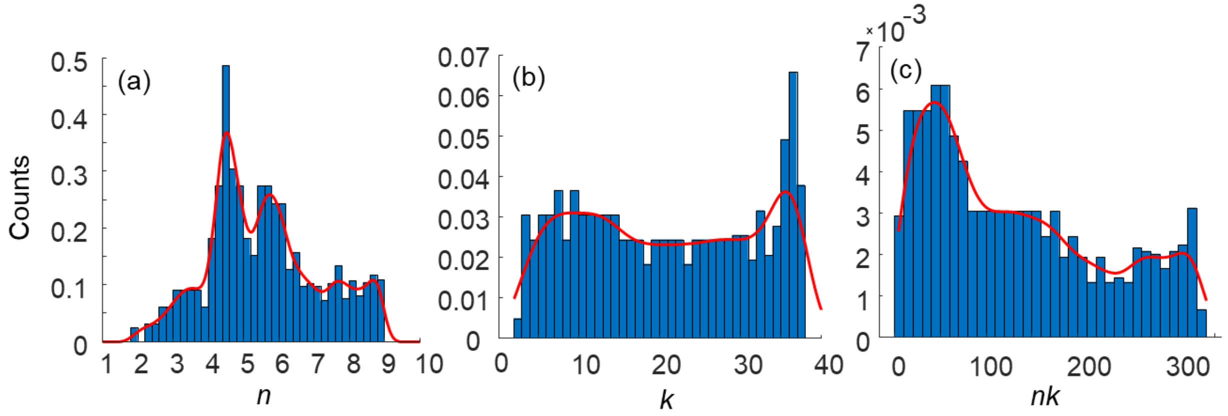

Figure F.2: Normalised histograms and the generated kernel PDFs for the optical properties of the substrate (a) optical constant *n*, (b) extinction coefficient *k*, (c) the product *nk*.

Appendix G: Iman and Conover Procedure

The Iman and Conover [36] procedure introduces correlations among the input parameters. A rank correlation structure **C** is introduced to matrix **X**, where each column represents an input, $x_{i,}$ to the neural network, and the rows represent the number of samples, N. Given matrix **X** and a required (r x r) rank correlation structure **C**, the following procedure can be adopted:

<u>Step 1:</u>

The values are ranked for each column in matrix X using MATLAB®'s *tiedrank* function. These ranks are saved in an (N x r) matrix called **RANKS**.

<u>Step 2:</u>

For each column in the **RANKS** matrix, Van der Waerden scores are computed and saved in a (N x r) matrix, **B.**

$$\mathbf{B}(\mathrm{j},\mathrm{i}) = \Phi^{-1}\left(\frac{\mathbf{RANKS}(\mathrm{j},\mathrm{i})}{N+1}\right) \tag{G-1}$$

where j is the row of the matrix, i is the column, and Φ^{-1} is the inverse CDF of the standard normal distribution.

<u>Step 3:</u>

B's Pearson rank correlation matrix is then computed and saved as an (N x r) matrix, **CS**.

<u>Step 4:</u>

A matrix **Q** and a matrix **P** are then computed such that,

$$\mathbf{CS} = \mathbf{QQ}^{\mathrm{T}} \tag{G-2}$$

$$\mathbf{C} = \mathbf{PP}^{\mathrm{T}} \tag{G-3}$$

Q and **P** can be found through a lower triangular, Cholesky decomposition of **CS** and **C**.

Step 5:

Matrices **T** (a transformation matrix) and **Y** are found such that,

$$\mathbf{T} = \mathrm{inv}\left(\mathbf{Q}\right) \cdot \mathbf{P} \tag{G-4}$$

$$\mathbf{Y} = \mathbf{B}\mathbf{T}^{\mathrm{T}} \tag{G-5}$$

Y contains Van der Warden scores with the required correlation structure, **C**. The ranks of entries in each column of **Y** are computed using MATALB®'s *tiedrank* function and saved in a matrix **R**.

Step 6:

Lastly, the entries in each column of **X** are permuted according to the ranks in **R** to yield a matrix **W**. Now, the entries in **W** follow the required rank correlation structure **C** while maintaining the original marginal distributions of each input parameter x_i.